



Characteristics of the CE 1226 Medieval tephra layer from the Reykjanes volcanic system

Agnes Ösp Magnúsdóttir



**Faculty of Earth Sciences
University of Iceland
2015**

Characteristics of the CE 1226 Medieval tephra layer from the Reykjanes volcanic system

Agnes Ösp Magnúsdóttir

60 ECTS thesis submitted in partial fulfillment of a
Magister Scientiarum degree in geology

Advisor
Ármann Höskuldsson

MS-Committee
Guðrún Larsen
Magnús Tumi Guðmundsson

Examiner
Börge Johannes Wigum

Faculty of Earth Sciences
School of Engineering and Natural Sciences
University of Iceland
Reykjavik, January 2015

Characteristics of the CE 1226 Medieval tephra layer from the Reykjanes volcanic system

Characteristics of the Medieval tephra layer

60 ECTS thesis submitted in partial fulfillment of a *Magister Scientiarum* degree in
Geology

Copyright © 2015 Agnes Ösp Magnúsdóttir
All rights reserved

Faculty of Earth Sciences
School of Engineering and Natural Sciences
University of Iceland
Askja, Sturlugata 7
101 Reykjavík
Iceland

Telephone: 525 4600

Bibliographic information:

Agnes Ösp Magnúsdóttir, 2015, Characteristics of the CE 1226 Medieval tephra layer from the Reykjanes volcanic system, Master's thesis, Faculty of Earth Sciences, University of Iceland, pp. 72.

Printing: Háskólaprent
Reykjavík, Iceland, January 2015

Abstract

The Medieval tephra layer was formed in an eruption within the Reykjanes volcanic system in the year 1226 CE. It is the largest tephra layer formed in the system and on the Reykjanes peninsula since the settlement of Iceland. The layer has been studied using grain size analysis, particle shape analysis, SEM studies and volume estimates using three different models of tephra layer volumes. Grain size distributions measurements were made for twelve ash samples at various distances from the volcanic source. The grains were analyzed down to 1 μm . Some of the samples were collected from a part of the ash layer but most of them were bulk samples. SEM analysis of representative grains in the phi 3-4 range showed them to have typical characteristics of particles formed in phreatomagmatic eruptions. The amount of fine material preserved in the soil from this phreatomagmatic eruption was small, suggesting that a part of the fine material has been removed by the combined effect of wind and water erosion. Various aspects of the tephra were examined in order to determine whether systematic changes occur with growing distance from source. The total grain size distribution was found using the Voronio method, applied to a series of bulk samples. The median grain size for this tephra layer was found to be 2.4 phi or 189 μm .

Shape analysis of the tephra layer was performed by using a particle shape analyzer. Two types of triangular plots were made using different parameters; some of the plots show a slight difference in particle shape between three selected sample places at various distances from the source. Statistical analysis shows that a significant but small changes occur with distance from source in almost all parameters used in the triangular plots.

Volume calculations were made using three different methods: The power law, exponential thinning and the Weibull method. The results show that the values obtained for the exponential (0.089 km^3) and Weibull (0.096 km^3) methods are almost identical and compare well with previous estimates. However, the power law method yields an unrealistic value of 0.49 km^3 , due to difficulties in defining the boundary conditions needed for the method. It is likely that the obtained volumes underestimate the volume of tephra erupted, as deposition that may have occurred towards west and south and northwest fell into the sea and is not included in the values obtained.

Útdráttur

Miðaldarlagið er öskulag ættað úr Reykjanes eldstöðvakerfinu og er það frá árinu 1226. Þetta er stærsta öskulag úr eldstöðvakerfinu eftir landnám Íslands. Öskulagið var rannskað með því að nota kornastærðargreiningar, kornalögunargreiningar, SEM myndir auk þess voru notuð 3 líkön við rúmmálsútreikinga. Kornastærðargreiningar voru gerðar á tólf sýnum úr mismunandi fjarlægðum frá upptökum gosins. Kornin voru greind niður í 1 μm . Sum sýnin voru einungis sýni úr hluta lagsins en flest öll sýnin voru úr öllum þykktarás lagsins. SEM greiningar voru gerðar á kornum af stærðnum 3-4 ϕ og sýndu þau einkenni sprengigosa. Magn fínefnis sem hefur varðveist í jarðvegi úr þessu sprengigosi er lítið, líklega hefur hluti fínefnis horfið úr öskulagi með vind- og vatnsrofi. Skoðaðir voru mismunandi hlutir til að ákvarða hvort að breytingar myndu kæmu fram með vaxandi fjarlægð frá upptökum. Heildarkornastærðardreifing var fundin með því að nota Voronio aðferðina og var aðferðinni beitt á sýni sem höfðu verið tekin af öllum þykktarás lagsins. Meðalkornastærð öskulagsins var funin með þessari aðferð og var hún 2,4 ϕ eða 189 μm .

Kornalögunargreiningar voru gerðar á öskulaginu með því að nota Particle shape analyzer. Tvær tegundir þríhyringsgrafa voru gerðar með því að nota ólíkar mælieiningar, sumir þessara þríhyrninga sýna eitthverja breytingu í kornalögun á milli þriggja sýnatökustaða í mismunandi fjarlægð frá upptökum. Tölfræðilegar greiningar sýna að það er marktækar breytingar þó litlar séu á milli staðanna í nánast öllum mælistærðum sem notaðar voru í þríhyringsgröfunum.

Rúmmálsreikingar voru gerðir með þremur mismunandi aðferðum. Þær voru power law, exponential thinning og Weibull aðferðin. Niðurstöður þeirra sýna að exponential (0,089 km^3) og Weibull (0,096 km^3) gefa mjög svipaða niðurstöðu og falla vel við áður útgefið rúmmál öskulagsins. Hinsvegar gefur power law frekar óraunverulega niðurstöðu uppá 0,49 km^3 , vegna erfileika við að skilgreina þau mörk sem aðferðin notar. Það er þó líklegt að rúmmál öskunnar sem fell sé vanmetið þar sem að askan hefur mögulega dreifst til vesturs, suðurs og norðvestur hefur hún fallið í sjóinn og því ekki tekin með í rúmmálsreikingana.

Table of Content

Abstract	iii
Útdráttur	v
Acknowledgements	xiii
1 Introduction.....	1
1.1 Volcanism in Iceland.....	1
1.2 The Reykjanes Ridge and Peninsula	3
1.2.1 Reykjanes volcanic system	4
1.2.2 Eruptive history and previous research.....	5
1.2.3 The CE 1226 eruption	6
2 Phreatomagmatism.....	9
2.1 Magmatic fragmentation	9
2.2 Magma – water interaction.....	10
2.3 Tephra.....	12
2.4 Eruption styles.....	12
2.4.1 Phreatomagmatic eruptions styles.....	13
2.5 Structures.....	14
2.5.1 Tuff rings	15
2.5.2 Tuff cones	15
2.5.3 Maars.....	15
3 Materials and methods	17
3.1 Material	17
3.2 Methods.....	18
3.2.1 Sieving	18
3.2.2 Density measurements	19
3.2.3 Sedigraph	20
3.2.4 Particle shape analyzer.....	21
3.2.5 SEM (Scanning electron microscope)	26
3.2.6 Total grain size.....	27
3.2.7 Volume calculations.....	27
4 Results.....	31
4.1 Grain size measurements.....	31
4.2 Total grain size	39
4.3 Shape analysis	40
4.3.1 Triangular plots.....	40
4.3.2 Frequency graphs	47
4.3.3 Shape plots.....	51
4.4 Scanning electron microscope.....	53
4.5 Volume calculations	57

4.5.1	Exponential thinning.....	57
4.5.2	Power law	59
4.5.3	Weibull method	60
5	Discussion	61
5.1	Grain size analysis	61
5.2	Particle shape analysis	64
5.3	SEM	65
5.4	Volume calculations.....	65
6	Conclusion	67
	References	69
	Appendix I.....	75
	Sample information	75
	Appendix II.....	77
	Histograms, cumulative curves and grain size data.....	77
	Appendix III.....	97
	SEM-Images	97
	Appendix IV.....	105
	Density measurements.....	105
	Appendix V	107
	Statistical analysis	107

Figures

<i>Figure 1-1: Volcanism in Iceland.....</i>	<i>2</i>
<i>Figure 1-2: Volcanic systems on the Reykjanes Peninsula</i>	<i>3</i>
<i>Figure 1-3: Craters in the Reykjanes area</i>	<i>4</i>
<i>Figure 1-4: Backscatter image of the most southwestern-most part of the Reykjanes volcanic system</i>	<i>6</i>
<i>Figure 1-5: Isopach map of the CE 1226 eruption and sample points</i>	<i>7</i>
<i>Figure 2-1: Magmatic fragmentation.....</i>	<i>10</i>
<i>Figure 2-2: Classification of volcanic eruptions after dispersal and fragmentation. F</i>	<i>13</i>
<i>Figure 3-1: Tephra in the soil 11 km from the source</i>	<i>17</i>
<i>Figure 3-2: The particle shape analyzer, grains that are being analyzed</i>	<i>21</i>
<i>Figure 4-1: Map showing the sample points where the tephra samples were collected.....</i>	<i>31</i>
<i>Figure 4-2: Sorting against the mean grain size</i>	<i>32</i>
<i>Figure 4-3: The grain size distribution of the Medieval tephra layer.....</i>	<i>33</i>
<i>Figure 4-4: All the samples of the Medieval tephra layer. The grain distribution has been split into categories on the basis of the size of the grains.....</i>	<i>34</i>
<i>Figure 4-5: Material finer than 63μm (4ϕ) plotted against the distance.....</i>	<i>35</i>
<i>Figure 4-6: Changes in material of 31μm (5 ϕ) and finer against distance</i>	<i>35</i>
<i>Figure 4-7: The material of the size finer than 11μm (6.5ϕ) against the distance</i>	<i>36</i>
<i>Figure 4-8: The largest grains presented on the phi scale for each sample plotted against the distance from the source</i>	<i>37</i>
<i>Figure 4-9: The largest grains presented in millimeters in each sample plotted against the distance from the source</i>	<i>37</i>
<i>Figure 4-10: The mean grain size plotted against the distance from the source. The mean grain sizes are here shown on the phi scale.....</i>	<i>38</i>
<i>Figure 4-11: Shows how the Voronoi cells are distributed for the area that the ash layer covered</i>	<i>39</i>

<i>Figure 4-12: The total grain size distribution for the Medieval tephra layer with the Voronoi method</i>	<i>39</i>
<i>Figure 4-13: Triangular plots for 3.0 phi at various distances, the form factor scale has been scaled by 2.5 to get a better range in the data</i>	<i>41</i>
<i>Figure 4-14: Triangular plots for 3.5 phi at various distances, the form factor scale has been scaled by 2.5 to get a better range in the data</i>	<i>42</i>
<i>Figure 4-15: Triangular plots for 4 phi and finer at various distances, the form factor scale has been scaled by 2.5 to get a better range in the data</i>	<i>43</i>
<i>Figure 4-16: Triangular plots for 3.0 phi at various distances, having form factor, compactness and circularity in the corners</i>	<i>44</i>
<i>Figure 4-17: Triangular plots for 3.5 phi at various distances, having form factor, compactness and circularity in the corners</i>	<i>45</i>
<i>Figure 4-18: Triangular plots for 4 phi and everything below that size at various distances having form factor, compactness and circularity in the corners.....</i>	<i>46</i>
<i>Figure 4-19: Frequency of the measured circularity at two different distances from the source</i>	<i>47</i>
<i>Figure 4-20: Frequency of the measured ellipse aspect ratio at two different distances from the source</i>	<i>48</i>
<i>Figure 4-21: Frequency of the measured circularity at three different distances from the source</i>	<i>48</i>
<i>Figure 4-22: Frequency of the measured ellipse aspect ratio at three different distances from the source</i>	<i>49</i>
<i>Figure 4-23: Frequency of the measured circularity at three different distances from the source</i>	<i>50</i>
<i>Figure 4-24: Frequency of the measured ellipse aspect ratio at three different distances from the source</i>	<i>50</i>
<i>Figure 4-25: Rectangularity, circularity and form factor plotted against feret aspect ratio</i>	<i>52</i>
<i>Figure 4-26: Rectangularity, circularity and form factor against feret aspect ratio</i>	<i>52</i>
<i>Figure 4-27: SEM images for the Medieval tephra layer. The grain size shown is 3.5 phi and the sample is taken 35 km from the source.....</i>	<i>53</i>
<i>Figure 4-28: Tephra from the Medieval tephra layer. The grain size shown is 3.5 phi and the sample is taken 46 km from the source.....</i>	<i>53</i>

<i>Figure 4-29: Tephra from the Medieval tephra layer. The grain size is 3.5 phi and the sample was taken 64 km from the source</i>	<i>54</i>
<i>Figure 4-30: Tephra from the Medieval tephra layer. The grain size is 4 phi and everything below that and the sample is taken 35 km away from the source.....</i>	<i>54</i>
<i>Figure 4-31: Tephra from the Medieval tephra layer the grain size is 4 phi and everything below and the sample is taken 46 km from the source.....</i>	<i>55</i>
<i>Figure 4-32: Showing tephra from the Medieval tephra layer. The grain size is 4 phi and everything below that, the sample is taken 64 km from the source</i>	<i>56</i>
<i>Figure 4-33: The plot for the exponential thinning method where \ln of the thickness of the layer is plotted against square root of the area.....</i>	<i>58</i>
<i>Figure 4-34: The power law fit for the CE 1226 eruption</i>	<i>59</i>
<i>Figure 4-35: The Weibull fit for the Medieval tephra layer.....</i>	<i>60</i>
<i>Figure 5-1: Changes in certain grain size classes with distance from the volcanic source.....</i>	<i>62</i>
<i>Figure 5-2: Changes in material below $63\ \mu\text{m}$ with distance from the source</i>	<i>62</i>
<i>Figure 5-4: The AD 1226 eruption against the Eyjafjallajökull 2010 eruption.....</i>	<i>66</i>

Tables

<i>Table 1: Classification table for tephra both shown in the phi scale and millimeters with the given names for each group.....</i>	<i>18</i>
<i>Table 2: Result from the Voronoi method for the total grain size of the Medieval tephra layer.</i>	<i>40</i>
<i>Table 3: The data for the Medieval tephra layer, t is the thickness in centimeters, A^* is the area that the layer covered in square meters and A is the area that it covered in square kilometers and then T is the thickness of the layer in kilometers.</i>	<i>57</i>
<i>Table 4: Shows results for the exponential thinning method were T is the intercept, k is the slope of the line and BS is the break in slope.</i>	<i>57</i>
<i>Table 5: Showing how the mean in each parameter changes between 11 km and 64 km from the source of the eruption. Between these two places was always significant statistical difference.....</i>	<i>64</i>

Acknowledgements

Firstly I would like to thank my supervisor Ármann Höskuldsson for guidance along the way and useful discussions. I would also like to thank the MS-committee, Magnús Tumi Guðmundsson and Guðrún Larsen, for the help during this work, discussions and useful comments on the thesis. Magnús Á. Sigurgeirsson gets a special thanks for letting me use his sample for further research.

Special thanks to Johanne Schmith for all her help, for taking the time to teach me how to use the instruments and many useful discussions about the particle shape analyzer.

I would like to think Toby Düring for his help with the statistical analysis.

I would like to think Rob Askew for reading the thesis over and correcting my English.

I would also like to thank my co-students, especially Tinna, Margrét, Edda and Halldóra for their friendship and good company over the years.

I would like to thank staff members of Askja for many good talks and comments over the time of my studies.

Then last but not least I would like thank my family especially Gunnar Snorri Guðmundsson and my daughter Kristín Emma for all their patience and support during his time and my parents for all their support.

This project was supported by the ICAO as a part of a catalogue of Icelandic volcanoes, a project of the Icelandic Meteorological Office and the Institute of Earth Sciences at the University of Iceland.

1 Introduction

Phreatomagmatism is a type of explosive eruptions that is the result of hot magma coming in contact with a water body. This interaction causes the magma to cool rapidly, fragment as the water boils and rapidly expands, resulting in an explosive eruption (Morrissey et al., 2000).

The main purpose of this project is to analyze data on the CE 1226 eruption within the Reykjanes volcanic system, especially with respect to the grain size distribution down to $1\mu\text{m}$ using a Sedigraph and the shape of the tephra grains using a particle shape analyzer.

The Reykjanes Volcanic Belt (RVB) is an active volcanic system fairly close to Reykjavík, the capital of Iceland, and Keflavík where Iceland's international airport is located. Therefore it is important to know the characteristics of this eruption in order to get an idea of the hazards eruption of this type could present in the future. The main research questions highlighted in this thesis are: (1) Does the grain size distribution of the tephra from CE 1226 eruption change with distance from the source vent, and (2) does the shape of the tephra finer than $125\mu\text{m}$ change with distance from the source vent?

Even though this eruption was of modest size compared to some of the major phreatomagmatic eruptions in Iceland, an eruption on this scale in this area could have a great effect on the lives of a large part of the population in Iceland, since about 70% of the inhabitants live within the area inside the 0.5 cm isopach of the CE 1226 eruption (Sigurgeirsson, 1992; Hagstofa Íslands, 2014).

This thesis is split into six main chapters. This chapter looks into the volcanism of Iceland, the volcanic systems of the Reykjanes ridge and Peninsula, the Reykjanes volcanic system, the eruptive history of the volcanic system and the CE 1226 eruption. In the second chapter the theoretical background of the eruption style and fragmentation is looked at. The material used and methods used are described in detail in the third chapter. The main results are presented in the fourth chapter, which is followed by chapters with discussion and conclusions.

1.1 Volcanism in Iceland

Volcanism in Iceland mostly occurs within the volcanic zones, which cover about 30.000 km^2 of the country. The volcanic zones are 15-50 km wide belts of volcanism and active faulting. The volcanic zones are characterized by volcanic systems that consist of either, fissure (dyke) swarms and/or a central volcano and in many cases both are present. These systems have a typical lifetime of about 0.5-1.5 million years (Thordarson & Höskuldsson, 2008). The exact number of volcanic systems in Iceland is a matter of definition and slight

variations are seen between different authors, Thordarson and Höskuldsson (2008) define thirty active volcanic systems 3 of those are in the Reykjanes Volcanic belt (RVB), 6 in the Western Volcanic zone (WVZ), 2 in the Mid-Iceland belt (MIB), 5 in the North Volcanic zone (NVZ), 8 in the East Volcanic zone (EVZ) 3 in the intraplate volcanic belt and 3 in the Snæfellsnes Volcanic belt (SVB), see Figure 1-1.

Out of the 30 volcanic systems, 19 have central volcanoes. Four of these systems have two central volcanoes bringing the number of identified central volcanoes to 23 (Thordarson & Höskuldsson, 2008).

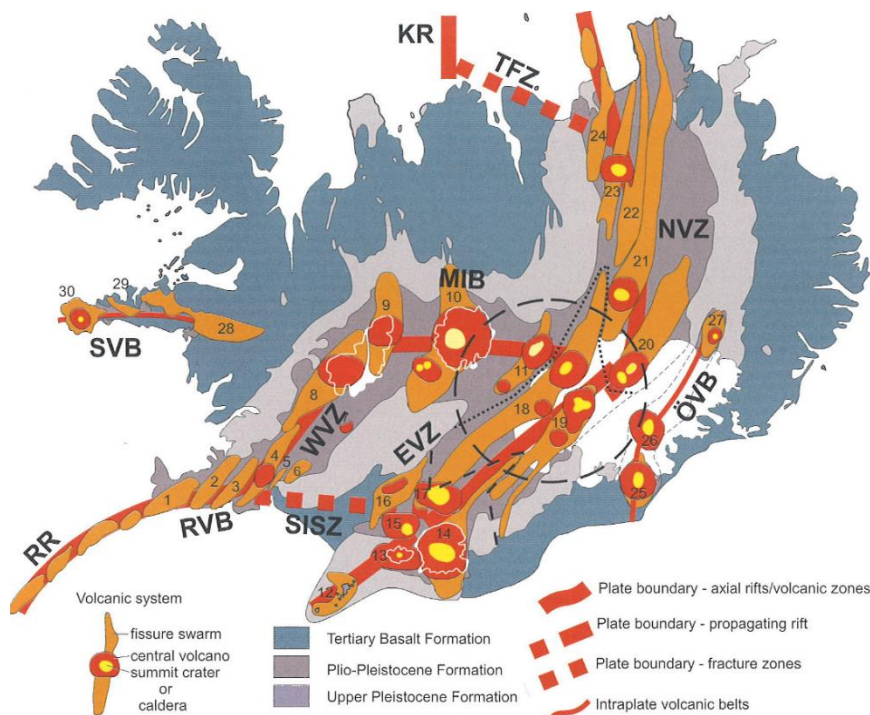


Figure 1-1: The plate boundary through Iceland and the associated volcanic systems. Volcanic systems contain either a central volcano or a fissure swarm or both. RR refers to the Reykjanes Ridge and RVB to the Reykjanes Volcanic Belt, other abbreviation are SVB for the Snæfellsnes Volcanic Belt, WVZ for the Western Volcanic Zone, SISZ for the Southern Icelandic Seismic Zone EVZ for the Eastern Volcanic Zone, MIB for the Mid Icelandic Belt, NVZ for the Northern Volcanic Zone, ÖVB for the Örfajökull Volcanic Belt, TFZ for the Tjörnes fracture zone and KR for the Kolbeinsey Rigde (from Thordarson & Höskuldsson, 2008).

Volcanism in Iceland is mostly around the central rift zones which are RVB, WVZ, EVZ and NVZ, but central volcanoes can be divided into off rift zone central volcanoes and rift zone central volcanoes. Rift zone central volcanoes are often broad, low angle shields. Higher relief has developed where the central volcano has been largely built in eruptions under glaciers and many have calderas. Off rift central volcanoes usually form prominent stratovolcanoes (Harðarsson et al., 2008; Sæmundsson, 1986).

1.2 The Reykjanes Ridge and Peninsula

Postglacial volcanic activity on the Reykjanes Peninsula is characterized by fissure swarms trending NE-SW. The peninsula is defined slightly differently from the Reykjanes Volcanic Belt above, since it is customary to include the Hengill volcanic system as part of the Reykjanes Peninsula. Some workers define Reykjanes and Eldvörp-Svartsengi with Fagradalsfjall as one system while others split this part of the Peninsula into Reykjanes, Eldvörp-Svartsengi with Fagradalsfjall, Krísuvík, Brennisteinsfjöll and Hengill (Clifton & Kattenhorn, 2006; Guðmundsson, 1986; Jakobsson et al., 1978), see Figure 1-2.

All the volcanic systems are 5-8 km. width and 30-50 km. long. Each volcanic system has two or more fissure swarms and all systems have an active geothermal area (Sæmundsson & Sigurgeirsson, 2013). The Reykjanes Peninsula lies obliquely to the rift zone and it has had periods of earthquakes which have activity on N-S fissures (Einarsson, 2008) and periods of volcanic eruptions and rifting on the NE-SW trending fissure swarms. These volcanic periods are called fires and have lasted for a centuries (Sæmundsson & Sigurgeirsson, 2013). All the volcanic systems on the Reykjanes peninsula have erupted in historical time (in the last 1100 years). Suggestions have been made that the volcanic activity on the peninsula is periodic, that is, there are periods of high volcanic activity, which lasts for hundreds of years, followed by a longer period of no volcanic activity that can last for several hundred years (Hreinsdóttir et al., 2001).

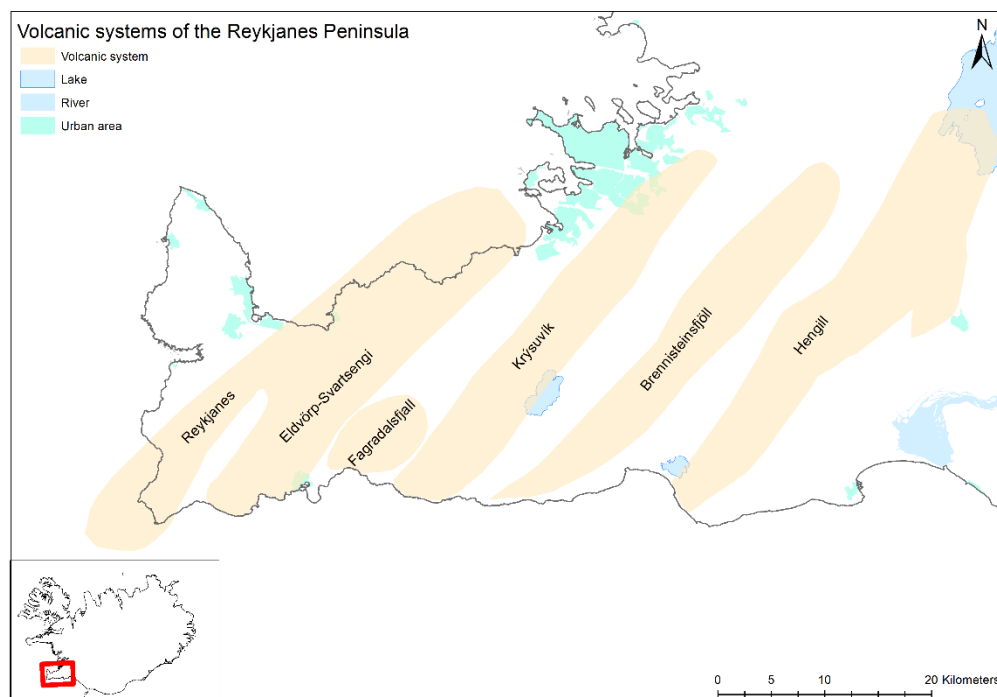


Figure 1-2: All five volcanic systems on the Reykjanes Peninsula based on Sæmundsson and Sigurgeirsson (2013).

The last historical eruptions were between 940 and 1340 CE, these were all fissure eruptions (Jakobsson et al., 1978). In the last eruption period the activity moved from one volcanic system to another in a 30-150 year interval. The activity was characterized by eruption periods on fissure swarm that lasted several decades, these kind of eruptions are called fires. On the Reykjanes Peninsula there have only been basaltic eruptions since the end of the last glaciation (Sæmundsson & Sigurgeirsson, 2013).

1.2.1 Reykjanes volcanic system

The Reykjanes volcanic system is 35 km long and 5 km wide in the south but about 15 km wide in the north. The south-easternmost 9 km of the volcanic system are under sea. There have been many submarine eruptions, which have left tephra layers in the soil in the Reykjanes area. The volcanic system has two crater rows which are 1.5 km apart and have a southwest-northeast direction. The last eruptive period in this system was between 1210-1240 (Sæmundsson & Sigurgeirsson, 2013). The Reykjanes area is barren, for the most parts covered by tephra, sand and lava flows (see Figure 1-3). From the lava plains rise palagonite- and pillow lava ridges that continue intermittently towards the NE of the area (Sigurgeirsson, 1995b).



Figure 1-3: One of the craters in the Reykjanes area (Agnes Ösp Magnúsdóttir, 2014).

1.2.2 Eruptive history and previous research

Off shore eruptions on the Reykjanes Ridge are mentioned in old written records. The oldest Icelandic records of eruptions in this area are from 1211 and describe this kind of an eruption. These records describe both a large earthquake that caused casualties and a fire that came up from the sea near Reykjanes. Written records also tell of a volcanic eruption in 1226 off the shore of Reykjanes. Þórarinnsson (1965) points out that these old records mention “darkness in the middle of the day” and describe its consequences as a “sandy winter”. In a record from 1238 a “red sunset” is also described. Later eruptions are also mentioned in the records during the years 1340, 1422, 1583, 1783, 1830, 1879 and 1926. For the last four eruptions there are rather good descriptions about ash fall and at what time of the year they happened (Þórarinnsson, 1965).

The ash layer from CE 1226 is often called the Medieval layer (isl. Miðaldalagið). It was first studied by Ólafsson (1983), who measured many soil sections on the Reykjanes Peninsula and traced the dispersal of it in much more detail than had been done earlier. The sampled data seem to indicate that the main wind direction during the eruption was from the southwest. The volcanic source was suggested to be a crater near Reykjnestá and the rock (isl. drangurinn) Karl is thought to be a part of this crater.

In the summers of 1989 and 1990 Sigurgeirsson (1992) did more work in the area and made an isopach map of the dispersal from the CE 1226 eruption and some other offshore eruptions in the area. He concludes that the volcanic source of the Medieval layer is 2-3 km out in the sea and not the crater near Reykjanestá as previously thought. Sigurgeirsson (1992) suggests that, the crater originally considered the source, is in fact a part of another submarine eruption within the Reykjanes volcanic system, Sigurgeirsson (1992) calls these craters at the coastline RG-2 and RG-3 since it was shown using geochemical analysis that the volcanic glass in these craters doesn't have the same geochemical composition as the volcanic glass in the Medieval tephra layer. The volcanic glass from the Medieval tephra layer has a higher value in FeO and TiO₂ and has a lower value in CaO than the volcanic glass from the craters.

In this thesis the source vents of the Medieval layer is put at about 2.5 km from the coastline. In fact the eruption in CE 1226 could have happened anywhere on AVR 1 (Axial volcanic ridge 1) which is shown on Figure 1-4. Höskuldsson et al. (2007) suggest that there were several eruptions in that area during the years 1226-1238. Backscatter images show that the axial ridges formed in several eruptions, on the AVR 1 and two eruption sites can be identified there. An eruption in the area where the AVR1 is at 50-100 meters depth under sea level could result in an explosive eruption.

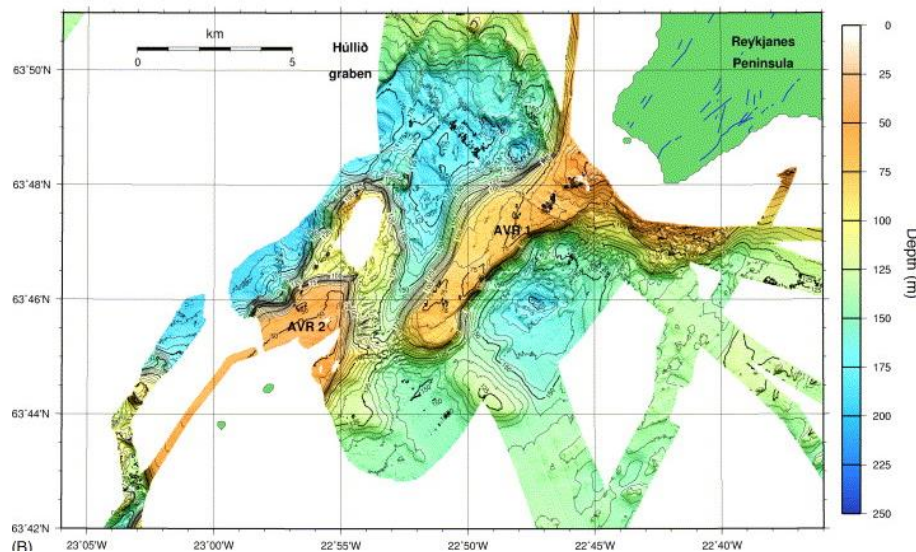


Figure 1-4: Backscatter image of the most southwestern-most part of the Reykjanes volcanic system (Höskuldsson et al., 2007).

1.2.3 The CE 1226 eruption

The phreatomagmatic eruption of CE 1226 was a submarine eruption according to the thickness distribution of the tephra layer. Which suggests that the origin is not far from the shore or about 2-3 km (Sigurgeirsson, 1995a). According to (Sigurgeirsson, 1992, 1995a) this eruption deposited about 0.1 km^3 of tephra on land which is preserved in the soil, the area within the 0.5 cm isopach was about 3500 km^2 . The volume inside the 0.5 cm isopach was calculated but the area outside of it was estimated, see Figure 1-5 (Sigurgeirsson, 1992, 1995a). Geochemical analysis on the tephra from the CE 1226 eruption has a SiO_2 of 49.08% (Haflidason et al., 2000). Geochemical analysis on the tephra characterizes it as tholeiitic, the main lava type that has erupted from fissures on the Reykjanes Peninsula. Although this eruption didn't leave a large ash layer on the Reykjanes Peninsula but most likely it did have a great impact on vegetation and habitats in the area (Sigurgeirsson, 1995a). However there are no written records about effects or consequences of the eruption on the surrounding area. Sigurgeirsson (1995a) summarized to try to get some idea of the impact of this eruption one can look into soil sections and search for some clues about the effects:

1. From the soil sections it can be seen that the ash has probably been blowing about for some time, possibly for some years after the eruption.
2. On the Peninsula it can be seen that under the CE 1226 ash layer is fine humus soil but above the layer is shifting sand or a very sandy soil, which indicates that there wasn't much soil formation after the eruption.
3. Some years before the CE 1226 eruption there had been another eruption on the peninsula, an effusive eruption on land and then an explosive eruption where the fissure reached the sea. It is thought that this event is the source of the shifting sand

and therefore vegetation on the Peninsula and surrounding areas was weaker than usual when the ash layer of the CE 1226 eruption fell.

From these statements it's safe to conclude that the effect of the CE 1226 eruption on vegetation was severe and in some places the vegetation had difficulties growing for a long time afterwards.

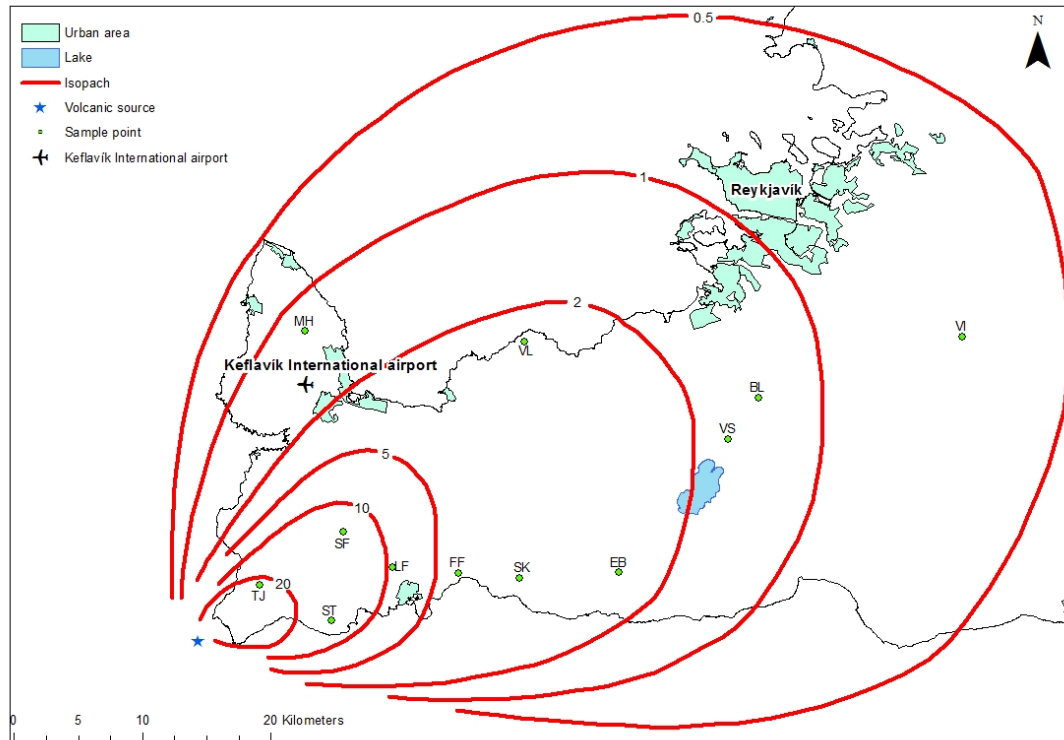


Figure 1-5: Isopach map of the CE 1226 eruption and sample points, the isopachlines are shown in centimeters based on Sigurgeirsson (1992); Sæmundsson and Sigurgeirsson (2013).

2 Phreatomagmatism

The processes in a phreatomagmatic eruption are difficult to study, mostly because phreatomagmatic eruptions take place under lakes, at sea or even under glaciers. Subglacial eruptions melt the overlying glacier creating large volumes of water, this water interacts with the magma as it would in submarine or sub-lacustrine environments. The ash layer from the CE 1226 eruption was formed by this kind of an eruption, i.e. a phreatomagmatic eruption.

Below the processes of fragmentation are discussed and for completeness both magmatic and phreatomagmatic fragmentation is described.

2.1 Magmatic fragmentation

Paper's by Zhang (1999) and Marti et al. (1999) provided new insight into the behavior of magma during fragmentation. Volcanic eruptions are driven by gas bubble formation as can be seen in Figure 2-1. This process is not well understood, especially how the bubbles form (Toramaru, 1995). In theory these bubbles should not be able to form at all. The surface tension inside a small bubble in magma should be much greater than the tension in the surrounding magma and for that reason the gas should dissolve in the magma and the bubble then disappear, but that is not the case. Bubbles start to form in the magma and at first they are very small, but as they rise closer to the surface they grow and that growth is controlled by inward diffusion of gases (Proussevitch & Sahagian, 1998; Sahagian, 1999; Sahagian & Proussevitch, 1996) as well as decompressive expansion as the magma rises up a magma chamber or conduit system. When the pressure dependent solubility is reduced the gas moves down a concentration gradient from a high point in the middle of the distance between two bubbles and from there it moves into the bubbles. The rate of the diffusion of the magma depends on the same properties as the viscosity (Sahagian, 1999). The bubble development is dependent on how fast the magma rises to the surface, if the rise is fast enough the diffusion of dissolved gas between the bubbles in the magma may not occur fast enough to maintain chemical equilibrium with the falling pressure. Therefore the magma becomes supersaturated in gases at low pressure in the volcano and at that point bubbles grow swiftly. As they grow their surface becomes bigger and as they become bigger the greater the rate of gas influx becomes. Fuelled by high enough level of magma supersaturation this runaway feedback effect can lead to bubble growth that is explosive. When the bubble growth has reached a critical growth rate (Sahagian & Proussevitch, 1996) the magma stops behaving like a liquid and starts to behave as an elastic solid (Marti et al., 1999; Zhang, 1999). When the stresses induced by growing bubbles increases the magmatic foam becomes unable to withstand the forces and brittle failure of the bubbles walls can lead to fragmentation into a gassy spray (Sahagian, 1999).

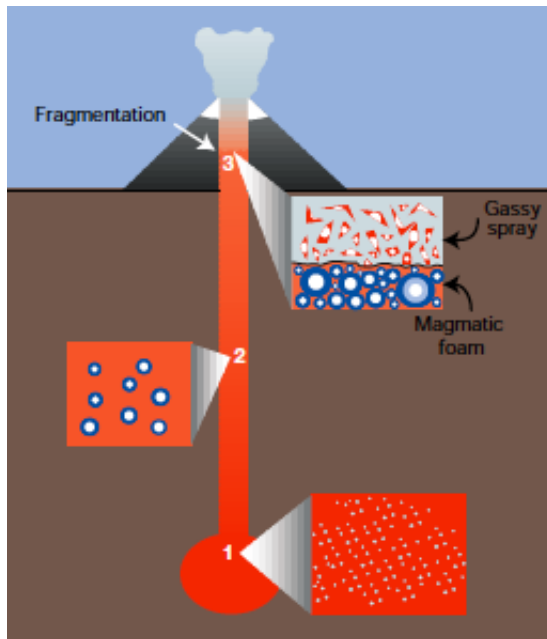


Figure 2-1: Bubble growth within magma: They start as small bubbles at depth but as they rise in the magma chamber or conduit system they grow. When they have reached a critical growth rate the magma starts to act like elastic solid and finally brittle failure of the bubbles leads to fragmentation of the bubble walls into glassy spray (Sahagian, 1999).

2.2 Magma – water interaction

Phreatomagmatic eruptions occur when magma comes in contact with a great amount of ground water, melt water from ice or sea. This causes a violently explosive eruption which can have quarrying effects leading to ejection of both juvenile magma and surface rocks (Francis & Oppenheimer, 2004).

Volcanic eruptions are driven by thermal energy. Phreatomagmatic eruptions, including Surtseyjan activity, use some of the thermal energy conserved in the magma to heat up the surrounding water and turn it into steam. The thermal shock on the magma leads to its fragmentation. The heating and boiling of the water leads to explosive expansion (Morrissey et al., 2000; Wohletz, 1983; Zimanowski et al., 1997).

The process of the interaction between magma and water has been studied for many years using experiments and therefore the physical dynamics of phreatomagmatic fragmentations are well studied. This process is called FCI (fuel coolant interaction), whereby heat transfer can occur in any environment. This FCI process converts heat into kinetic energy in a very short time (Morrissey et al., 2000).

As mentioned previously before many experiments have been done in the last 30 years or so. These experiments were carried out to find out what happens in the process when magma and water meet (Wohletz et al., 1995). In the case of mixing of hot melt and water then the descriptive term is Molten Fuel Coolant Interactions (MFCI) and, volcanic MFCI is often used for phreatomagmatic expansion (Zimanowski & Wohletz, 2000). MFCI

occurs when two liquids are mixed together in this case magma and water. It is important that the temperature of the magma is above the critical temperature of the water (Büttner & Zimanowski, 1998). When these two liquids have mixed, and a high heat transfer rate has been activated, this results in brittle reaction of the melt which is driven by the thermally induced expansion of water (Büttner et al., 2002).

FCI is usually split up into four phases, they are described in detail in e.g. (Morrissey et al., 2000; Wohletz, 1983; Wohletz, 1986; Zimanowski et al., 1997):

1. The initial contact and coarse blending between fuel and coolant under a stable vapor film causes boiling conditions.
2. A layer is formed between the liquid and the hot magma or a solid body when this film has been completed, it collapses which is caused either by the passage of a pressure pulse that could be for example, from seismicity or by a local implosion due to rapid condensation of coolant vapor. The fuel and coolant vapor are thermally and mechanically coupled when the coolant vapor is completely condensed.
3. The increase of heat transmission from fuel to coolant and fine fragmentation of the fuel, leading to superheated and pressurized water. When the coolant heats it expands which leads to rapid increase in load stress on the melt. Explosive seismic energy is released by the relaxation of load stress in the brittle mode. The release of kinetic explosive energy released in this phase is about 90% of the total kinetic energy.
4. As the superheated water transforms to superheated steam a volumetric expansion of the fuel-coolant mixture takes place. The fuel and coolant are thermally and mechanically decoupled at this stage.

To further describe the processes in steps 2 and 3, detailed experiments have revealed the following: If low-energy shock waves (smaller than 10 J) are passed through a premix of magma and water, a quasi-coherent collapse of the vapor film can occur (i.e., the induction of vapor films may collapse if the premix takes place in few nanoseconds, and the following reactions have a duration of several hundred microseconds), and the so called “direct contact” between both liquids of the premix occurs that is the complete hydraulic coupling of both liquids consequently, the transfer of heat from magma to water increase proportionally to the area of the direct contact interface. Both processes are coupled in a positive feedback mechanism. Heat flux from the magma to the water increases strongly, and the water becomes superheated. In the end the superheated water vaporizes. The expanding steam now drives a volcanic eruption along with further fragmentation processes by disrupting some parts of the system that are not yet part of the process (Zimanowski et al., 1997).

2.3 Tephra

Tephra is a collective term for all airborne pyroclasts, regardless of their size or shape. Tephra is a greek word proposed by Sigurður Þórarinnsson as a collective term for airborne pyroclasts in his doctoral thesis in 1944. Aristotle used the word tephra, which in greek means ash, in his decription of an eruption on Lipari Islands in the 4th century BCE (Thorarinsson, 1944).

During a volcanic eruption fragmented magma is transported from inside of the Earth to the atmosphere. This material is in the form of liquid magma, phenocrysts, dissolved volatiles and country rock material from the conduit walls or the ground surface (Wilson & Houghton, 2000). The material is ejected from the volcanic vent at very high speed into the atmosphere and is deposited as pyroclastic fall or pyroclastic flow deposits. Fall deposits are both produced in “dry” magmatic eruptions and “wet” phreatomagmatic eruptions; grain size distribution and morphology of the pyroclasts, of the whole deposit, reflect the eruption type.

Fall deposits get thinner with distance from the volcanic vent, where the point of maximum thickness usually is. Isopach maps are made to show the distribution of the tephra and its thickness. Isopachs maps usually form regular ellipses and are elongated in the downwind direction, the main dispersal direction is usually called a dispersal axis (Houghton, Wilson, & Pyle, 2000).

The tephra that is formed in a phreatomagmatic eruption is a mixture of glass, crystals and material that has fragmented from the conduit walls, usually called lithics. The lithic fragments can range from blocks and bombs (>64 mm) in size down to fine ash (<0.064 mm). The shape of the tephra can indicate the fragmentation by fracturing if the grains have angular edges. The grains in a phreatomagmatic eruption are finer grained than tephra formed in a magmatic eruption. When the tephra grains are observed using an electron microscope the phreatomagmatic tephra have distinctive shapes, the grains are blocky, fusiform, mosslike, platy and spherical or droplike. Other textural features that can be used to distinguish the tephra are particles adhering to glass surface, grooves or scratched, chipped edges and rounded edges (Morrissey et al., 2000).

2.4 Eruption styles

Classifications of the fragmentation (F) and the dispersal (D) of the volcanic products was introduced by Walker (1973), later redefined by Self and Sparks (1978) and Walker (1980). Phreatomagmatic eruptions are split into two main eruption types Surtseyan and Phreatoplinian. Surtseyan eruptions were defined after an eruption in Surtsey in 1963. Surtseyan activity occurs when a basaltic explosive eruption takes place in the sea or a lake. These kind of eruptions are more explosive than Strombolian activity. The eruption column may reach several kilometers in to the air and the dispersal is generally greater than in activity of the Hawaiian or the Strombolian kind. Eruptions of the Surtseyan kind

most often happen in a submarine environment and therefore their dispersal characteristics are not as well studied as for large Plinian eruptions (Walker, 1973). Phreatoplinian is used for eruptions that have a large dispersal or over 50 km^2 within the $0.01T_{\max}$ isopach see Figure 2-2. Eruptions that are classified as phreatoplinian are more silicic than deposits made by a Surtseyan eruption (Self & Sparks, 1978).

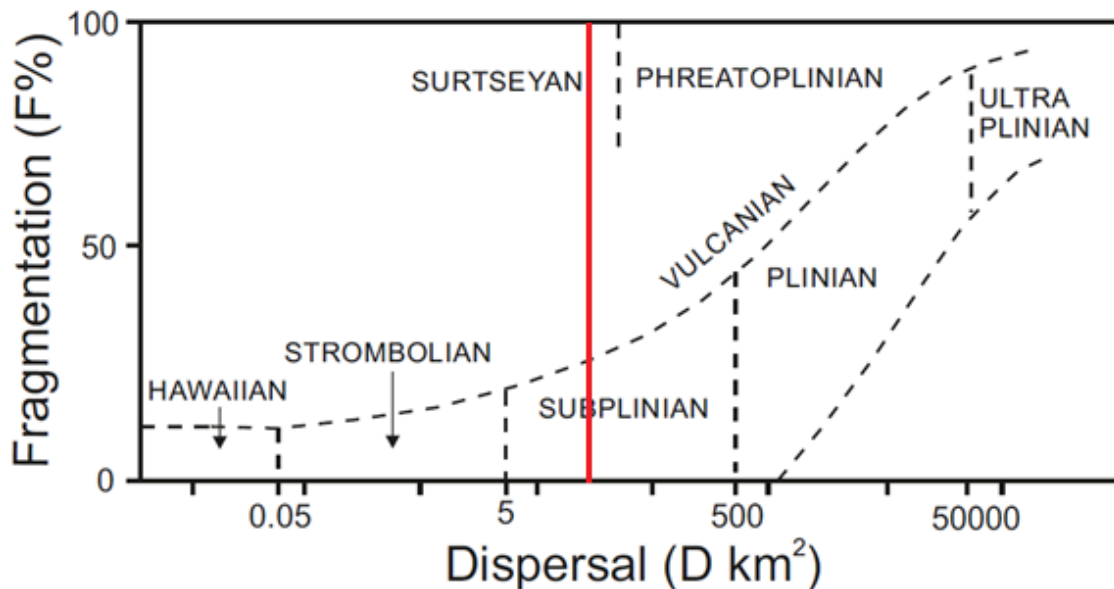


Figure 2-2: Classification of volcanic eruptions after dispersal and fragmentation. F is the percentage of material finer than 1 mm on the axis that crosses the $0.1T_{\max}$ isopach against the dispersal D which is the area enclosed by $0.01T_{\max}$. T_{\max} is the measured maximum thickness of the tephra layer. The red line represents possible dispersal of the area enclosed by the $0.01T_{\max}$ (Agnes Ösp Magnúsdóttir, 2014); based on (Self & Sparks, 1978; Walker, 1973; Walker, 1980)

For the CE 1226 eruption T_{\max} can't be measured because the source is off shore and the crater is not preserved. The red line represents that the maximum thickness of the layer was 20 meters but the maximum thickness could have been much greater. The fragmentation can't be exactly measured since a sample so close to the source is unobtainable, but the dispersal of tephra from this eruption tells us that the fragmentation was rather high.

2.4.1 Phreatomagmatic eruptions styles

Phreatomagmatic eruptions are usually classified into two main groups; Surtseyan eruptions and Phreatoplinian eruptions.

2.4.1.1 Surtseyan eruptions

Surtseyan eruptions are the result of a basaltic eruption taking place in a sea or lake and therefore they are more explosive than Strombolian eruptions and have a dispersal of tephra in a downwind direction from the eruption. The eruption column from these kinds of eruptions can be expected to reach few a kilometers into the air (Thorarinsson et al.,

1964; Walker, 1973). When eruptions of this kind starts at a lake or ocean bottom there may not be much to see on the surface. The main changes to the surrounding area are dirty, discolored water and perhaps dead fish floating around (e.g. Francis and Oppenheimer, 2004). At shallow water the eruption becomes explosive as water accesses the top of the magmatic vent. Powerful blasts occur every few minutes or seconds causing pyroclastic material to propel up in dark masses, the fragments arcing upwards along parabolic paths, tailing smaller fragments behind. The term cock's tail is usually used to describe this. Activity of this kind can continue for many weeks or until enough material has piled up on the seafloor so that it has reached above sea-level, closing access of external water to the vent resulting in cessation of phreatomagmatic activity and the onset of strombolian activity. However it is possible for seawater to get into the crater causing phreatomagmatic explosions (Francis & Oppenheimer, 2004).

2.4.1.2 Phreatoplinian eruptions

Phreatoplinian eruptions have been defined as wet Plinian eruptions, meaning that they usually form from evolved magma that has fragmented through interaction with external water (Houghton, Wilson, Smith, et al., 2000; Self & Sparks, 1978). They are quite similar to Plinian eruptions apart from forming much finer tephra. The deposits from Plinian and Phreatoplinian eruptions are much dryer than deposits from Surtseyan eruptions, the reason considered to be water vapor formation is more prominent in the phreatoplinian eruptions (Morrissey et al., 2000). Phreatoplinian eruptions have a large dispersal area of fine grained tephra deposits. Phreatoplinian eruptions are defined as having dispersal over 50 km² (Figure 2-2) and high fragmentation similar to Surtseyan eruptions. Phreatoplinian eruptions can last from only a few hours up to a few weeks. (Houghton, Wilson, Smith, et al., 2000).

2.5 Structures

Maars and tuff rings are formed in shallow water or subaerially. They are the result of a phreatomagmatic eruption when water and magma come together. These water magma interactions can occur in shallow groundwater, the sea, under a glacier or when a lava flow reaches the sea. Hydroclastic volcanoes are divided into three different types after their morphology and structure, they are:

1. tuff rings
2. tuff cones
3. maars

These phenomena are normally formed in one single eruptive episode with nearly constant eruptive conditions during the growth of the volcanic landform and can last from a few days up to years at the most. Studies of scoria cones have shown that complex structures due to alternating magmatic and phreatomagmatic eruptive conditions over a longer period of time. Some volcanoes have evolved from a maar, tuff ring or a tuff cone phase to a

scoria cone phase followed by lava flows which results in a composite volcanic structure (Vespermann & Schmincke, 2000).

2.5.1 Tuff rings

Tuff rings are usually not more than 50 meters high and they consist of craters which have small depth to width ratios at or above ground level. They also have low ejecta rims of hydroclastic debris and beds dipping $<25^\circ$. Tuff rings deposits consist from a mixture of juvenile and accidental clasts. The main constituent of the well stratified deposits are juvenile pyroclasts (Vespermann & Schmincke, 2000).

2.5.2 Tuff cones

Tuff cones have higher profiles than tuff rings and maars and they also have a steeper slope, with bedding dips over 25° . The floor of the crater is usually above ground level. The deposit is composed mainly of juvenile clasts and subordinate amounts of accidental clasts. The rim beds of the tuff cones are massive and they are interpreted as having been emplaced laterally by turbulent surges, fall and remobilization processes (Vespermann & Schmincke, 2000).

2.5.3 Maars

The definition of Maars is that there are craters shaped like a bowl the depth of them can be from 10 m to more than 500 m to the pre eruptive surface. Maars have low well bedded ejecta rims surrounding them the beds dipping is more than 25° and their thickness decreases rapidly in thickness away from the rim. Maar deposits can be distinguished from tuff rings and tuff cones by the abundance of nonjuvenile components. Deposits are replaced by base surges and fallout (Vespermann & Schmincke, 2000).

3 Materials and methods

In this study several methods and technical procedures were used. This chapter describes the methods used in the treatment of the tephra samples and how the data was analyzed. The methods used were sieving, density measurements, and analyses with sedigraph, particle shape analyzer and a scanning electron microscope. The total grain size of the tephra layer was estimated and volume calculations performed.

3.1 Material

The tephra used in this research was a basaltic in composition, with SiO_2 content of 49.08% (Haflidason et al., 2000), from the CE 1226 phreatomagmatic eruption from the part of the Reykjanes volcanic system that is under sea.

Samples collected by Magnús Á. Sigurgeirsson, for his Masters project, in the summers of 1989 and 1990 were used in this work. Additional bulk samples were collected by Agnes Ösp Magnúsdóttir in the spring of 2014, see Figure 3-1.

Two of the earlier collected samples were contaminated by soil. To get rid of most of the soil they were boiled in a peroxide solution in a water bath at 40°C. After the peroxide treatment the samples were dried and then they went through the same process as other samples.

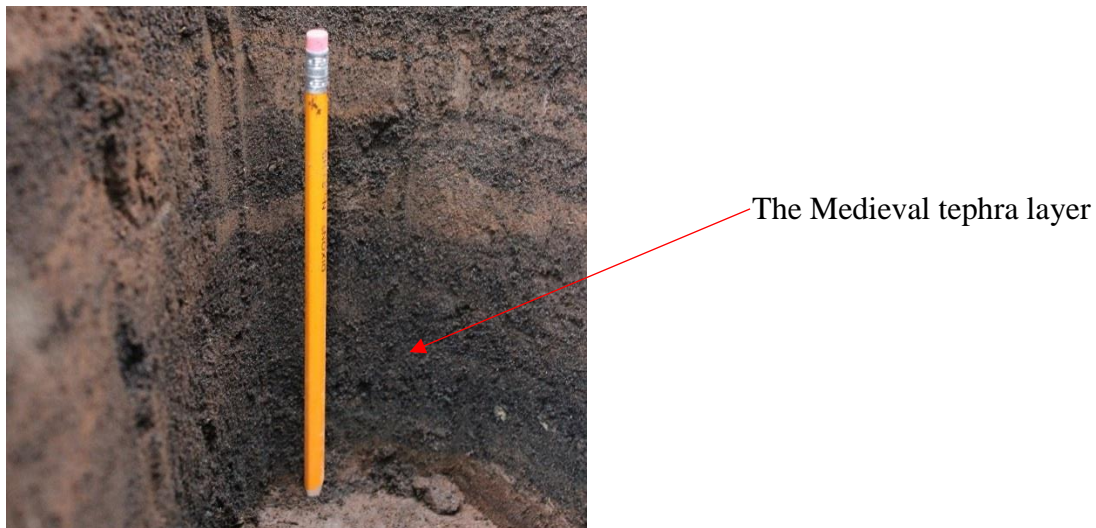


Figure 3-1: From the field work, showing tephra in the soil about 11 km from the source (Agnes Ösp Magnúsdóttir, 2014)

3.2 Methods

3.2.1 Sieving

The samples previously collected by Magnús Á. Sigurgeirsson in the summers of 1989 and 1990, had already been hand sieved for his earlier Master's project but the new samples had to be hand sieved for this project.

Grain size analysis is a widely used technique to describe and analyze sediments. The size of the particles in a particular deposit can reflect fragmentation processes, erosion processes or weathering which generates particles of many different sizes and the nature of subsequent transport processes. The particles have a huge size range; they can range from several meters to a few microns. Because of this large range a logarithmic scale is often used. This scale is often referred to as the phi scale. The phi scale is based on the following relationship

$$\phi = -\log_2 d \quad (1)$$

Where ϕ is the phi size of the particle and d is the grain diameter in millimeters (Boggs, 2006).

Table 1: Classification table for tephra both shown in the phi scale and millimeters with the given names for each group (Þórðarsson, 1990).

Phi (ϕ)	Millimeter (mm)	Size class
<-6	>64	Blocks and bombs
-5 to -6	32-64	Coarse lapilli
-4 to -5	16-32	Medium lapilli
-1 to -4	2-16	Fine lapilli
0 to -1	1-2	Coarse ash
4 to 0	0.064-1	Medium ash
>4	<0.064	Fine ash

Grain size measurements are done by sieving through a set of nested, wire-mesh screens where each mesh has its own size. The sieve sizes are in certain millimeters or phi sizes. The sieving technique measures the dimension of the particles, the intermediate size of the particle is determined if the particle goes through a particular mesh (Boggs, 2006).

To find the mean grain size and sorting the results from the sieving and the sedigraph were put into an excel program called GRADISTAT (Blott & Pye, 2001) which calculates statistical parameters that can be useful when interpreting grain size data.

3.2.2 Density measurements

Density calculations were done by using a pycnometer method. This method uses a pycnometer flask. It is very precise procedure and therefore widely used for determining density of e.g. powders and granules. The pycnometer method is more time-consuming and labor-intensive than other available methods but it is chosen for its precision.

The pycnometer method entails difficulty of precise volume determination of the powder sample V_s for determination of the solid ρ_s where m_s is the sample mass. Three measurements have to be done with a known density liquid to get a good accuracy.

$$\rho_s = \frac{m_s}{V_s} \quad (2)$$

Volume of the solid can be calculated according to equation 3 where V_{ges} is the volume of the pycnometer and V_{fl} is the volume of liquid in the pycnometer.

$$V_s = V_{ges} - V_{fl} \quad (3)$$

First it is necessary to calculate V_{ges} this is done by filling the pycnometer with a liquid and the mass of the liquid (m_{1fl}) in the flask is then determined also, the temperature of the liquid has to be known and the density of the water is determined accordingly (ρ_{fl}). Now the volume V_{ges} can be calculated according to equation 4.

$$V_{ges} = \frac{m_{1fl}}{\rho_{fl}} \quad (4)$$

The next step is to empty, clean and dry the pycnometer. Then the sample material, m_s , is put in the pycnometer and then it is weighed. Next, the pycnometer is filled with a liquid with known density (i.e. water) and it is weighed again, which gives $m_{(fl+s)}$. The mass of the liquid (m_{2fl}) can now be calculated from this information according to, equation 5.

$$m_{2fl} = m_{(fl+s)} - m_s \quad (5)$$

V_{fl} can then be calculated according to equation 6.

$$V_{fl} = \frac{m_{2fl}}{\rho_{fl}} = \frac{m_{(fl+s)} - m_s}{\rho_{fl}} \quad (6)$$

The volume of the sample can now be calculated using equation 3. When the volume of the sample has been found, equation 2 can be used to calculate the density of the sample. (Sartorius, 1999).

3.2.3 Sedigraph

The Sedigraph is a particle size analyzer which can analyze grains from 300 μm down to 0.1 μm (Micromeritics, 1996-2014). To get the best results, the optimal amount of material to put in the Sedigraph for analysis is about 3 grams, but it can work with much less. The Sedigraph consists of three units, a particle size analyzer, a multifunctional computer and a MasterTech. The MasterTech is a carousel which holds the samples and makes sure that the right sample goes in at any given time. The Sedigraph is used for many different things and in different fields e.g. in geology, ceramics and cosmetics (Micromeritics, 2010).

The Sedigraph uses two main principles, they are the Stokes law and the absorption of X-ray radiation (Beer-Lambert Law). According to the Stokes law the biggest and heaviest grains will settle first. Absorption of X-ray radiation is done by using a narrow collimated beam of X-rays to measure the particle concentration in the liquid medium. To measure the baseline the amount of X-ray absorption is measured with no particles in the liquid. When the measurements are performed the cell is filled with sedimentation liquid (i.e. a liquid, usually water, which the sample has been added to) and the X-ray absorption is measured. The combination of those two theories, which are the Stokes law and the X-ray absorption makes the Sedigraph a very useful instrument in many fields. Interpretation of the raw data is rather easy, but it gives a lot of data which you have to sort out (Micromeritics, 2010).

3.2.3.1 Technical details when using the Sedigraph

About 3 grams of the material that is going to be analyzed is weighted and put into a cup, in the present work material (volcanic ash from the CE 1226 eruption) finer than 90 μm was used. Then a mixture of glycerol and water is added to the ash. The density of the sample is put in to the computer program to find what liquid mixture to use. The Reynolds number must be between 0.1 and 0.3 for the flow to be right. For the CE 1226 ash the density was measured to be 2.70 g/cm^3 , the Reynolds number was 0.17 and the appropriate liquid compositions was 40 % glycerol and 60% water measured by weight.

3.2.3.2 Data processing from the Sedigraph

The Sedigraph and hand sieving rely on two very different methods. To merge these two datasets together a best practice guide from the Irish marine office was used. The Irish marine office merged sieve data and laser diffraction data to produce a complete particle size distribution at 0,5 ϕ intervals. To do this they hand sieve down to 1 mm and put material that is 1 mm and below in size laser diffraction to find out the grain sizes. When the data is then merged together all laser data of 1 mm and above is removed from the dataset and then the dataset is rescaled to 100%. When laser data is converted into weights the total weight of <1mm is used. Sieve weights are used for sediment > 1mm including 1mm fraction and everything below 1 mm is derived from laser weights (Mason, 2011).

For analyzing in the sedigraph grain sizes of 4 and <4 ϕ (63 μm and <63 μm) are used. When processing the data everything that is analyzed as 4 ϕ or above is taken out and the

rest is rescaled to 100%. Then finally it is converted into weights. After the two datasets were merged they were put into histograms and cumulative graphs which can be seen in appendix II.

3.2.4 Particle shape analyzer

The Particle Insight, particle shape analyzer can measure grains from 400 μm down to 2 μm in width and diameter and the length of the grains can range from 10 μm up to 1000 μm . The instrument takes images at a rate of up to 30 frames per second with real time analysis. Shape models that are included are circular, rectangular, elliptical, polygonal, fiber and irregular. To form analysis only a very small amount of sample is needed. After the sample is put into the device it flows through a thin cell (see Figure 3-2). This thin cell has an illumination source on one side and a camera on the other side. The camera records dark silhouettes of the particles which are then sent to a computer. A computer program then analyses each particle based on their size and shape found by their shadows by using a pre-selected model which is appropriate for the kind of particles that are being analyzed each time (Particle Insight).

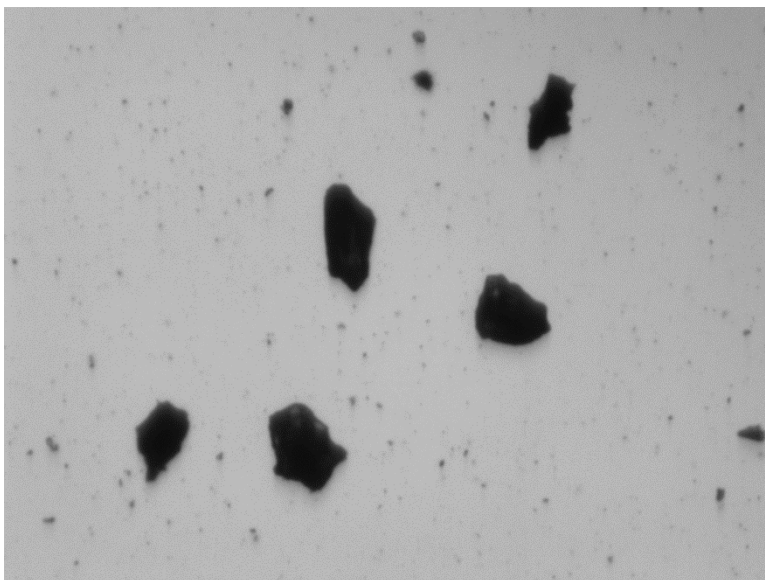


Figure 3-2: Image from the particle shape analyzer showing grains that are being analyzed, these grains are from the VL sample which is 35 km from the source and they are from 3.5 phi (Agnes Ösp Magnúsdóttir, 2014).

3.2.4.1 Technical details of the use of the particle shape analyzer

Three samples from various distances from the volcanic source were used for the analysis. The grain sizes that were analyzed were 3.0 phi, 3.5 phi and 4 phi and material finer than that. Very little sample material is needed to perform these analysis. Focus rejection is set at 90% therefore all grains that don't fulfill that requirement are automatically rejected. Bubble formation in the fluid is an inescapable part of the process but to try to prevent this, sodium polyphosphate is used in a little amount in the water. The classification criteria are

also used by rejecting every observed particle that has more than 0.9 in circularity because they are most likely bubbles.

3.2.4.2 Data processing from particle shape analyzer

In this experiment 12000 grains were counted and measured. Particle insight measures 27 different parameters. Some of those 27 parameters were used to make triangular plots. The purpose of these triangular plots was to see if the distance from the source had any effect on the shapes of the examined grains.

In Boggs (2006) particle shape is plotted on triangles which have form factor, compactness and sphericity on the axis.

In sedimentology the conventional form factor (F) classifies particles into platy, bladed or elongated using equation 7.

$$F = \frac{(a - b)}{(a - c)} \quad (7)$$

Where F is the conventional form factor, a is the longest axis, b is the intermediate axis and c is the shortest axis. However, in this work we use slightly different definition given below equation 12.

Compactness is defined as the ratio of platyness, bladedness and elongateness using the following equation 8.

$$S = \frac{c}{a} \quad (8)$$

Where S is the compactness, as above c is the shortest axis and a is the longest axis.

Sphericity can tell us how well a particle of a certain shape relates to transport properties of a sphere, the expression roundness refers to the degree to which the edges of a particle are rounded. Sphericity can also be used as indication of a fluvial transport distance and furthermore to measure the particle's suspensibility and transportability. Sphericity is found by using equation 9:

$$\Psi = \left(\frac{c^2}{c * b} \right)^{1/3} \quad (9)$$

Where Ψ is the sphericity, c and b defined as before.

Particle insight does not measure these exact parameters but a best approximation I made using measured parameters. The parameters used were circularity, compactness and form

factor for one type of triangular plots and for the other type form factor, feret aspect ratio and fiber aspect ratio (see below for definitions) were used. Particle insight only measures the tephra grains in two dimensions not in three as described above so this makes comparison very hard and almost impossible, the tephra grains are not defined into groups after their compactness, platyness, bladedness or elongation because of the difference in methodology.

When making the first type of triangular plots circularity is used instead of sphericity. Circularity is defined as the form area (A) and bounding circle diameter (D_{BC}). A perfect circle has the circularity of 1. Sphericity and circularity would not give the same value but the circularity is thought to be the best proxy provided by the software. The circularity is calculated from equation 10:

$$\text{Circularity} = \frac{4A}{\pi D_{BC}^2} \quad (10)$$

Where A is the form area and D_{BC} is the bounding circle diameter (Particle Insight).

Compactness is calculated as the square root of the circularity as equation 11 shows, the compactness value does not vary as greatly as the circularity:

$$\text{Compactness} = \frac{2\sqrt{A}}{\sqrt{\pi D_{BC}^2}} \quad (11)$$

The form factor used the Particle Insight software and therefore applied here (see results) is slightly different from the conventional one (equation 7) and is found using calculated from equation 12:

$$\text{Form factor} = \frac{4\pi A}{P^2} \quad (12)$$

Where A is calculated from area and P is the perimeter of the particle projection. Form factor is a number between 0 and 1 where the form factor of a perfect circle would be 1 (Particle Insight).

For the second type of the triangular plots the form factor is found in the same way as before (equation 12).

Fiber aspect ratio is the ratio between the fiber length and width. The fiber model is good for measuring long particles that may be curved or bent, but have similar thickness over the whole length. If a particle like that would be straightened out and made to fit in a rectangle that rectangle would have a fiber length given by equation 14 and a fiber width given by equation 15. The dimensions of the rectangle computed from the silhouette's area (A) and perimeter (P) are found using equation 13:

$$D = \frac{(P^2 - 16A)}{4} \quad (13)$$

If $D > 0$

$$\text{Fiber length: } L = \frac{(P + 2\sqrt{D})}{4} \quad (14)$$

$$\text{Fiber width: } W = \frac{A}{L} \quad (15)$$

By using fiber aspect ratio elongation of the grains is calculated.

Feret aspect ratio is the ratio between the feret length and feret width. The feret width and length measure the smallest and the largest spacing between two parallel lines that come in contact with the particle but do not intersect it in any way (Particle Insight).

By using the form factor, feret aspect ratio and the fiber aspect ratio in the corners of the triangular plots each factor represents a certain form. The form factor represents a rectangular particle, the feret aspect ratio represents a platy particle and the fiber aspect ratio represents an elongated particle (Particle Insight).

The shape plots are made by multiplying three factors which are rectangularity, circularity and form factor and then the outcome is plotted against the feret aspect ratio. The first two factors, rectangularity and circularity, are area-based parameters that are rather stable (Schmith, 2014).

All the factors except rectangularity have been previously introduced. The rectangularity is used for non-fiber shaped objects that have a low aspect ratio. Rectangularity is defined as the smallest area that is enclosed in but does not intersect the object. Bounding rectangle aspect ratio is found using equation 16:

$$\text{Aspect ratio} = \frac{L}{W} \quad (16)$$

(Particle Insight).

3.2.4.3 Frequency plots

Frequency plots were made, using circularity and ellipse aspect ratio, where the x-axis is split up to unit intervals. The frequency plots show if the number of particles in each interval change with distance from the volcanic source. Circularity has been previously described but ellipse aspect ratio is defined as the ratio between the equivalent elliptical area length and width (Particle Insight).

3.2.4.4 T-test

To check if there is any significant difference between the means of the parameters used on the triangular plots as the distance changes, the t-test for equality of means is used to determine if any significant change occurs. There are two versions of the t-test for equality of means where the assumption is made that the variance is unknown. One version assumes that the samples do have the same variance but the other version assumes that the samples don't have the same variance. To determine which version to use on each case the Levene's test for equality of variance is used. Levene's test tests the null hypothesis that the samples have equal variances:

$$H_0: \sigma_1^2 = \sigma_2^2 \quad (17)$$

Versus the alternative hypothesis that the variances of the samples are not equal:

$$H_1: \sigma_1^2 \neq \sigma_2^2 \quad (18)$$

Where σ_1^2 and σ_2^2 are the hypothetical variances of the samples (Levene, 1960).

When it has been determined whether the null hypothesis of the Levene's test is rejected or not it is possible to use the version of the t-test for equality of means that better fits the results of the Levene's test. Although the two versions of the t-test for equality of means differ in some ways, they both have the same null hypothesis and alternative hypothesis:

$$H_0: \mu_1 - \mu_2 = 0 \quad (19)$$

Versus the alternative hypothesis:

$$H_1: \mu_1 - \mu_2 \neq 0 \quad (20)$$

Where μ_1 and μ_2 are the hypothetical means of the samples.

The version of the test where the equality of the variances is assumed uses a test statistic given by:

$$t = \frac{(\bar{x} - \bar{y})}{s_p \sqrt{1/n + 1/m}} \quad (21)$$

Where \bar{x} and \bar{y} are the calculated means of the two samples, n and m are the sizes of the two samples and s_p is the root of the pooled estimator of the common variance, given by:

$$s_p = \sqrt{\frac{(n-1)s_1^2 + (m-1)s_2^2}{n+m-2}} \quad (22)$$

where s_1^2 and s_2^2 are the calculated variances of the samples.

When the nul hypothesis is true the t in equation 21 has a t -distribution with $n+m-2$ degrees of freedom and since there is an inequality sign in the alternative hypothesis it is a two tailed test. Therefore an absolute value of the t in equation 21 is used to determine the rejection region which becomes:

$$|t| > t_{\alpha/2, n+m-2} \quad (23)$$

Where α is the chosen significance level. If the absolute value of t in equation (23) is larger than the critical value the null hypothesis is rejected and it is assumed that the two samples don't have equal means (Walpole et al., 2012).

In the version where it is assumed that the variances of the samples are unequal the test statistic is given by:

$$t = \frac{(\bar{x} - \bar{y})}{\sqrt{s_1^2/n + s_2^2/m}} \quad (24)$$

When the null hypothesis is true the t in equation (24) has a t -distribution with approximate v degrees of freedom where:

$$v = \frac{(s_1^2/n + s_2^2/m)^2}{(s_1^2/n)^2/(n-1) + (s_2^2/m)^2/(m-1)} \quad (25)$$

As the previous version this version of the test is also a two tailed test so the absolute value of the t in equation 24 has to be used to determine the rejection region. The rejection region then becomes:

$$|t| > t_{\alpha/2, v} \quad (26)$$

Where α is the chosen significance level. Therefore if the absolute value of t in equation 26 is larger than the critical value the null hypothesis is rejected and it is assumed that the samples don't have equal means (Walpole et al., 2012).

3.2.5 SEM (Scanning electron microscope)

The SEM, TM3000 was used to take pictures of the grains of the CE 1226 eruption. Photos were taken of grains that were 3.5 ϕ and smaller. When taking the pictures various magnifications were used depending on what fitted best for each grain. Before the grains were analyzed on the SEM they were gold coated to yield a better contrast.

The TM3000 has a variable accelerating voltage 5 or 15 kV. The TM3000 has a magnification of 15x to 30.000x. Backscattered electrons are mainly used to take images of the specimen ("HITACHI TM3000 Tabletop Scanning Electron Microscope," 2014).

3.2.6 Total grain size

When calculating the total grain size of the eruption, the Voronoi tessellation statistical method was used. This method was first used by Bonadonna and Houghton (2005) on pyroclastic deposits. The method splits the area into polygons and each polygon represents a Voronoi cell that is built for each sample point. That point is assigned with the same mass per unit area values and grain size distribution as the corresponding sample point. A zero line is drawn surrounding the area that has tephra fallout. The total grain size distribution is obtained as the areas weighted average of all the Voronoi polygons over the whole deposit.

By finding the total grain size distribution it can be used to find eruption style and fragmentation by linking the particle size and the initial gas content and the water magma interaction process (Bonadonna & Houghton, 2005).

For the total grain size calculations Bonadonna and Houghton (2005) compiled a Matlab program, which was used to calculate the total grain size for the Reykjanes eruption 1226.

3.2.7 Volume calculations

Calculations of tephra volume can be done by many different approaches e.g. the power law fit, exponential thinning and the Weibull method. The volume of the Reykjanes eruption 1226 has been previously calculated and the total volume of the tephra was found to be 0.1 km³ (Sigurgeirsson, 1992, 1995a). The power law fit, exponential thinning and Weibull were used for recalculations volume of the tephra.

All volume calculations are made from a semi-log plot of thickness of the ash layer versus the square root of the area. There are two main approaches used they are from Pyle (1989, 1990) which uses the assumption of a circular and elliptical isopachs and the other is from Fierstein and Nathenson (1992) which uses a similar approach but showed that the method is also valid for isopachs of more irregular shape. Equation 27 is the main formula for calculating the volume of the tephra:

$$V = \int_0^{\infty} T dA \quad (27)$$

Where A (m²) is the total area that is enclosed by an isopach thickness line T. The way the T is calculated differs between the three methods mentioned before.

3.2.7.1 Exponential thinning

In the exponential thinning method it is assumed that thickness decline with increasing distance from vents can be described with equation 28

$$T = T_0 \exp(-k\sqrt{A}) \quad (28)$$

Where T_0 is the maximum thickness and k is the slope on plots of the natural logarithm (ln) of thickness vs. the square root of the area.

When looking at a semi-log plot with thickness versus the square root of an area the plot often shows more than one break in slope. When that is the case the thickness equation is integrated for each segment. Equation 29 is the most simple of such equations for deposit volume; where there is one break in slope. More terms are needed for a larger number of breaks (Bonadonna & Houghton, 2005):

$$V = \frac{2T_0}{k_1^2} + 2T_0 \left[\frac{k_2 BS_1 + 1}{k_2^2} - \frac{k_1 BS_1 + 1}{k_1^2} \right] \exp(-k_1 BS_1) \quad (29)$$

Here T_0 is the intercept, $-k_n$ is the slope and BS_n is the break in slope. The CE 1226 eruption has one break in the slope and therefore equation 29 was used calculate the volume.

3.2.7.2 Power law method

In the power law method the relationship between thickness of ash and the square root, T , of the area is described by equation 30:

$$T = T_{pl} \sqrt{A}^{-m} \quad (30)$$

Where T_{pl} is a constant and m is the power-law coefficient. Equations 27 and 30 give equation 31:

$$V = \left[2T_{pl} * \frac{\sqrt{A}^{(2-m)}}{2-m} \right]_0^\infty \quad (31)$$

To prevent the V in equation 31 to become infinite when $\sqrt{A} = 0$ and $\sqrt{A} = \infty$ two arbitrary integration limits are set they are B and C this gives equation 32:

$$V = \frac{2T_{pl}}{2-m} (C^{(2-m)} - B^{(2-m)}) \quad (32)$$

B is defined as the distance of the calculated maximum thickness i.e. the value of \sqrt{A} , as defined in equation 30, when $T=T_0$ in equation 28. C is the downwind limit of the significant of volcanic cloud spreading that would show on satellite images (Bonadonna &

Houghton, 2005). The power law method is thought to estimate natural thinning curvature of the tephra when data is missing (Bonadonna & Costa, 2012).

3.2.7.3 Weibull method

The Weibull method is more flexible than a fit using multiple exponential segments. Also it does not require the sometimes rather arbitrary choice of both position and number of straight segments. Bonadonna and Costa (2012) proposed that this method can produce natural thinning similar to the power law method when data is missing, and that it shows less gradual thinning and a better fit to real data than the power law method does. The Weibull is based on the assumption that thickness, T , scales with square root of the isopach area in accordance with equation 33.

$$T = \theta \left(\frac{x}{\lambda}\right)^{n-2} \exp\left[-\left(\frac{x}{\lambda}\right)^n\right] \quad (33)$$

λ represents the characteristic decay length scale of deposits thinning (this value is typically expressed in kilometers), for the thickness scale θ is used (this value is typically expressed in centimeters), the value of $\theta = e^*T(\lambda)$ where e is the Euler-Napier constant, n is a shape parameter and has no unit, when $n=1$ it describes the exponential relationship for $xT(x)$. Using equations 27 and 33 the volume of the tephra deposits can be calculated as shown in equation 34:

$$\begin{aligned} V &= \int_0^\infty T dA = 2 \int_0^\infty T(x) x dx \\ &= \frac{2\theta\lambda^2}{n} \int_0^\infty \frac{n}{\lambda} \left(\frac{x}{\lambda}\right)^{n-1} e^{-\left(\frac{x}{\lambda}\right)^n} dx \\ &= \frac{2\theta\lambda^2}{n} \left[1 - e^{-\left(\frac{x}{\lambda}\right)^n}\right]_0^\infty = \frac{2\theta\lambda^2}{n} \end{aligned} \quad (34)$$

(Bonadonna & Costa, 2012)

4 Results

In this chapter the results of data analysis applying the methods described in the previous chapter. This chapter is split into sections on grain size measurements, particle shape measurements, scanning electron microscope images, the total grain size and volume calculations.

4.1 Grain size measurements

Grain size measurements were done on twelve samples (see Figure 4-1) from the CE 1226 eruption in the Reykjanes volcanic system.

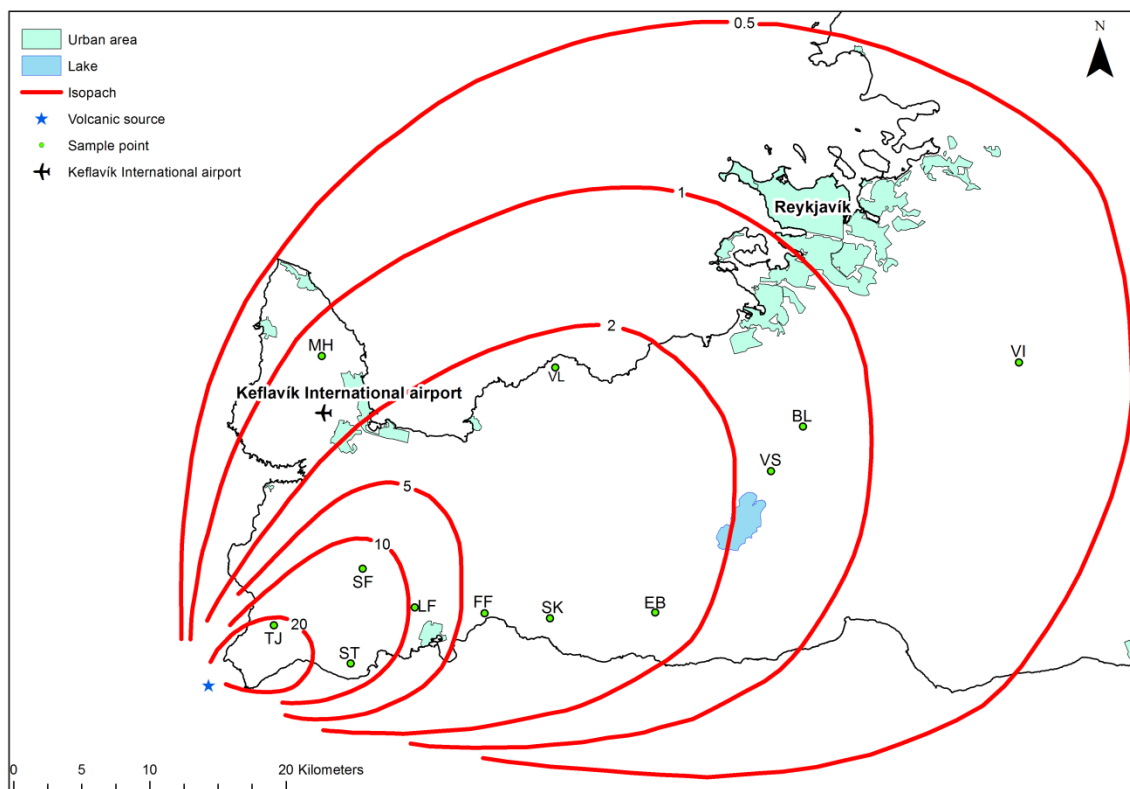


Figure 4-1: Map showing the sample points where the tephra samples were collected, isopach lines based on Sigurgeirsson, 1992; Sæmundsson & Sigurgeirsson, 2013.

Analyses were done down to 1 μm using the Sedigraph. A complete grain size distribution was performed for all sample locations which are at various distances from the source. Bulk samples were used to make the grain size distribution curves. To merge the hand sieving and the Sedigraph together the methods in chapter 3.2.4 are used.

Figure 4-3 shows an example of a distribution curves for the Medieval tephra layer. Sample locations are shown in Appendix I and all the distribution curves are shown in Appendix II. It is very hard to find good places to take samples because of a lack of vegetation in the area. This especially applies for the Reykjanes area, less so for the Reykjanes peninsula as a whole. Therefore high quality samples in the area are hard to come by and some of the samples from this area are reworked. There is lack of fine material in the samples compared to other phreatomagmatic eruptions e.g. the Eyjafjallajökull eruption in 2010.

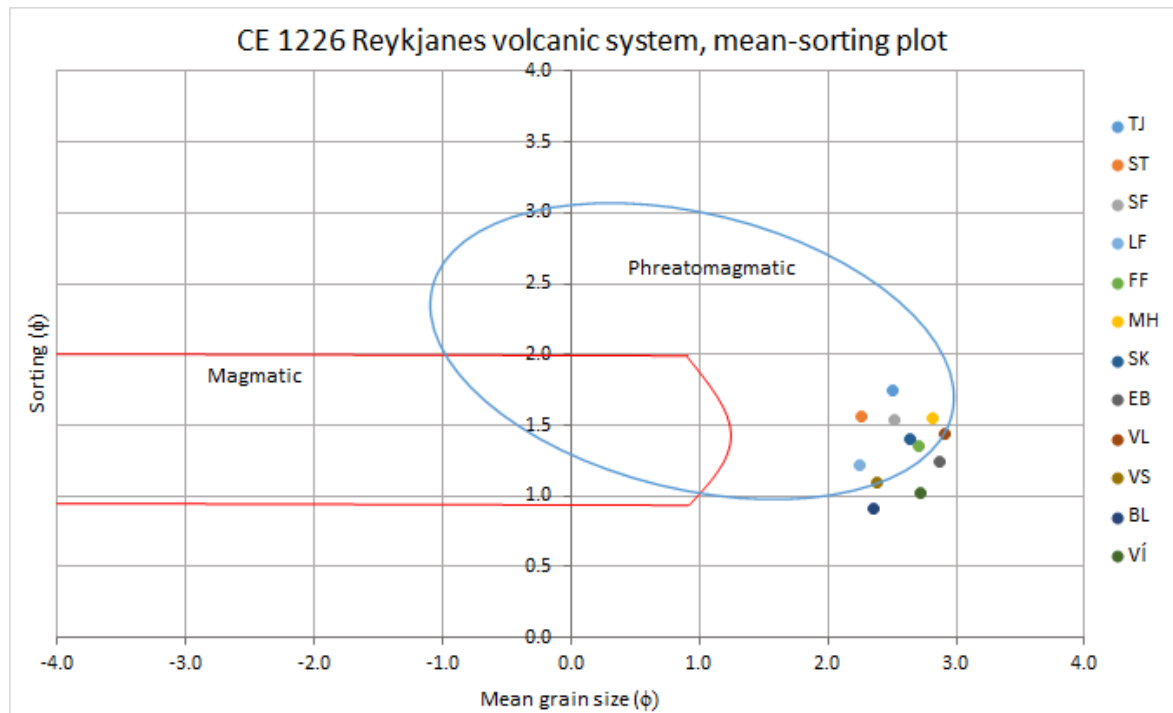


Figure 4-2: Sorting against the mean grain size and how the samples from each location is classified into magmatic or phreatomagmatic eruptions styles. This graph is based on Walker and Croasdale (1971) (Agnes Ösp Magnúsdóttir, 2014).

Walker and Croasdale (1971) presented a plot that showed the difference between magmatic and phreatomagmatic eruption styles by using the sorting against the mean grain size. By plotting up the samples like is done in Figure 4-2 it can be seen that the samples from the Medieval layer plot in the phreatomagmatic region.

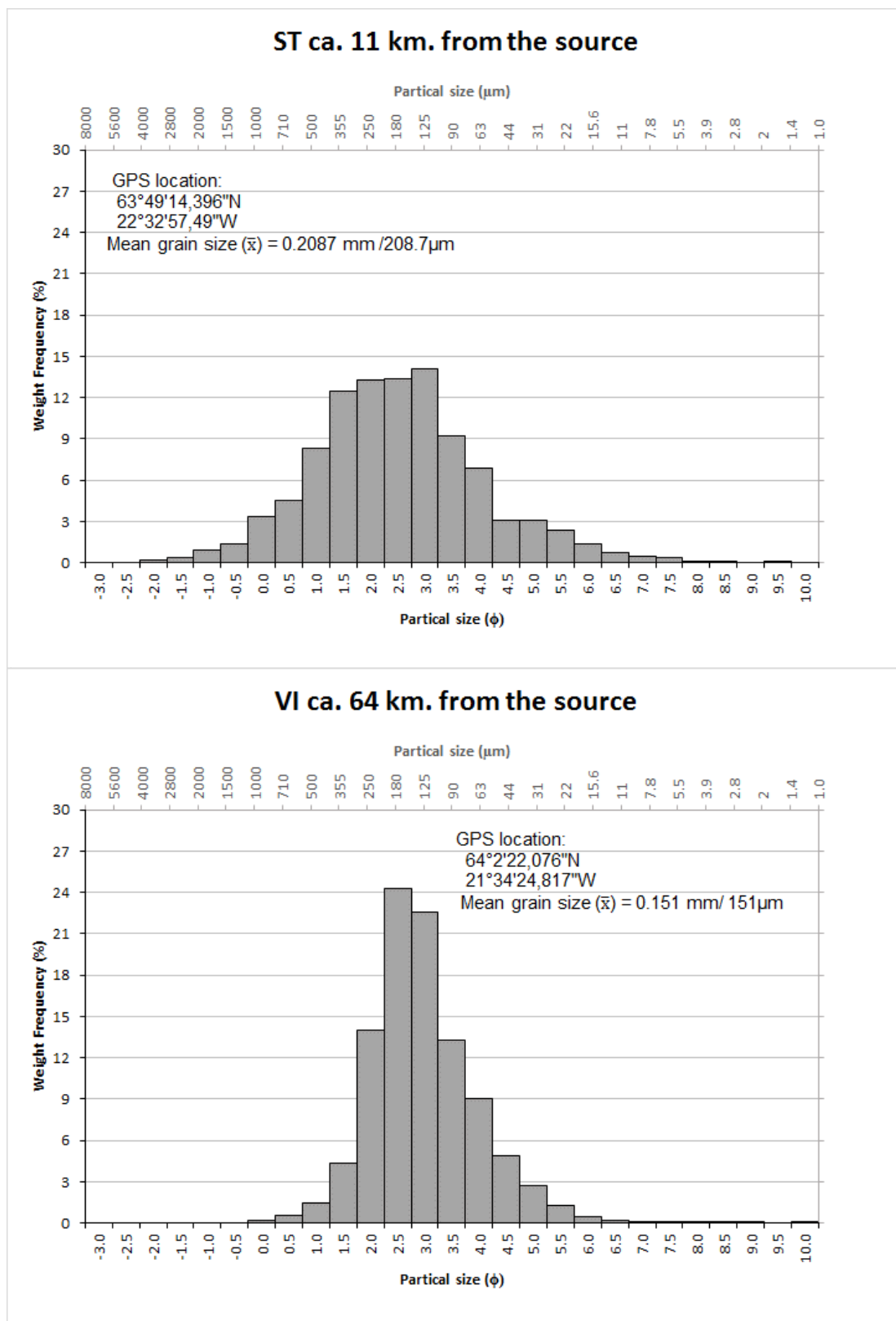


Figure 4-3: The grain size distribution of the Medieval tephra layer. The samples are analyzed down to 1 μ m. Sample locations are ST (upper figure) taken from about 11 km from the source; VÍ (lower figure) taken about 64 km from the source (Agnes Ösp Magnúsdóttir, 2014).

Two distribution curves are shown in Figure 4-3 one is close to the source from the ST sample location which is about 11 km from the source and the second one is further away or from the VÍ sample location which is 64 km away from the source. As can be seen there is a large difference between the two curves. The ST one doesn't have a sharp maximum but just over 50% of the sample is fairly evenly distributed over the grain size range 90-355 μm . VÍ has two grain size classes (125 and 180 μm) that are much larger than the rest of grain size bins. It can also be seen that the amount of coarser grains is much greater at shorter distances from the source.

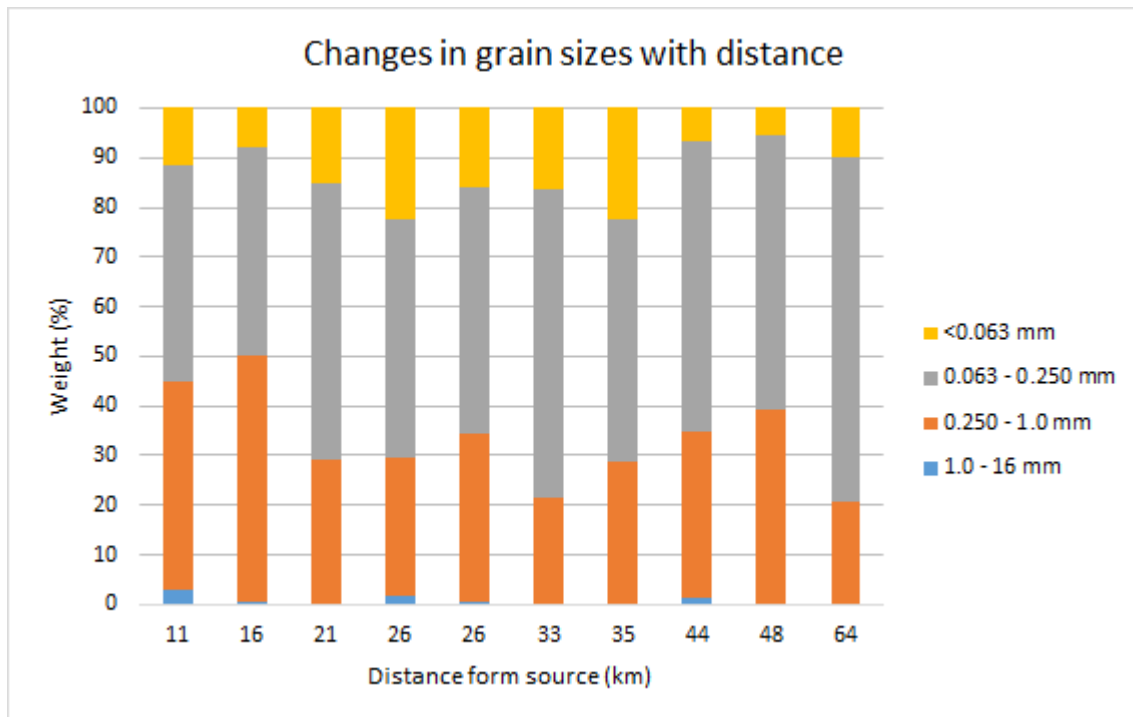


Figure 4-4: All the samples of the Medieval tephra layer. The grain distribution has been split into categories on the basis of the size of the grains. It shows how categories change with distance from the source (Agnes Ösp Magnúsdóttir, 2014).

When the grain size distributions are split into categories like shown in Figure 4-4 it can be seen that the distributions do change slightly with the distance from the source. The amount of coarse material is very small no matter the distance from the source but it can be seen that there is a difference in the fine material from one distance to another. It is clear that the biggest difference is on one hand in the grain sizes from 0.250-0.063 mm as the ratio of grains in that category increase as the distance from the source grows and on the other hand in the grain sizes of 1.0-0.250 mm, the ratio of grains in this category decreases as the distance from the source grows.

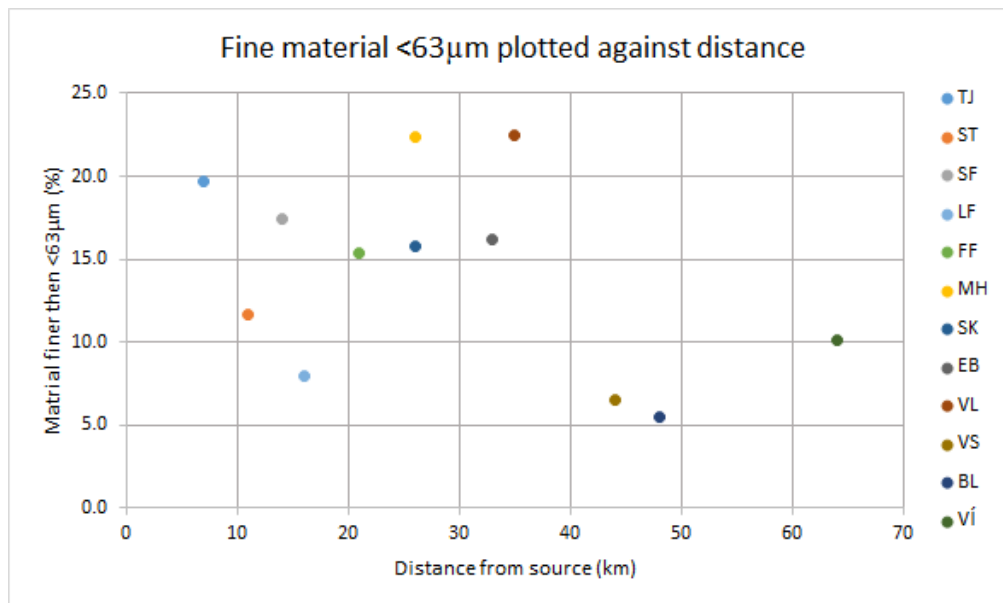


Figure 4-5: Material finer than 63μm (4φ) plotted against the distance from the source (Agnes Ösp Magnúsdóttir, 2014).

Materials finer than 63μm decrease with distance from the source. The trend seems to be that the amount of fine materials are decreasing although there are some outliers that don't seem to follow this trend.

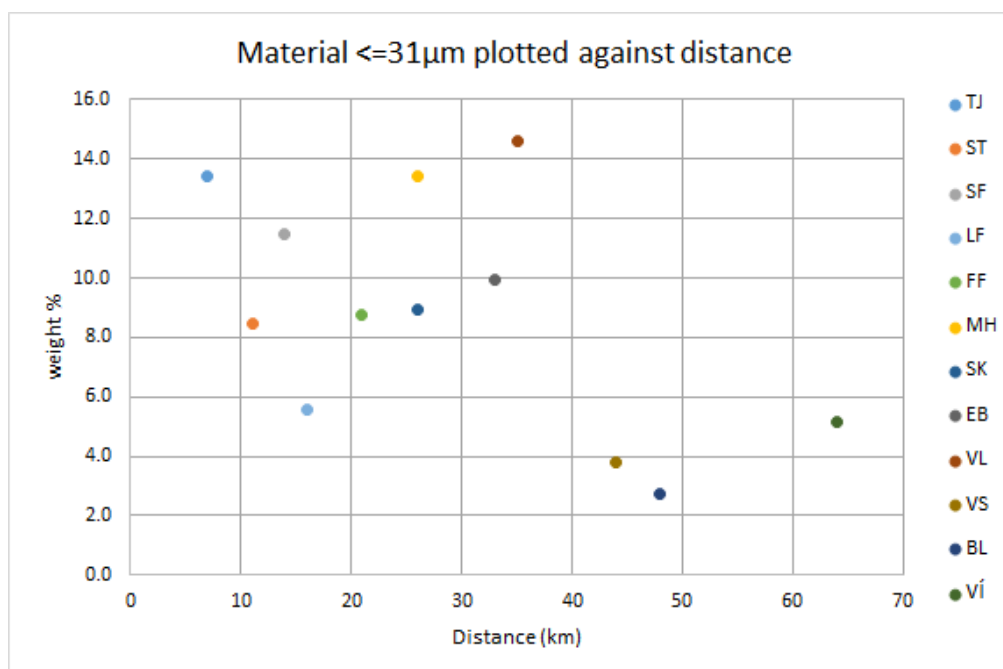


Figure 4-6: Changes in material of 31μm (5 φ) and finer against distance from the source Agnes Ösp Magnúsdóttir, 2014).

When the material of 31μm and finer is looked at in Figure 4-6 they show a similar behavior as the material below 63 μm. did. There can be seen a definite trend of decrease with distance although some samples seem to be outliers and don't stick to the trend.

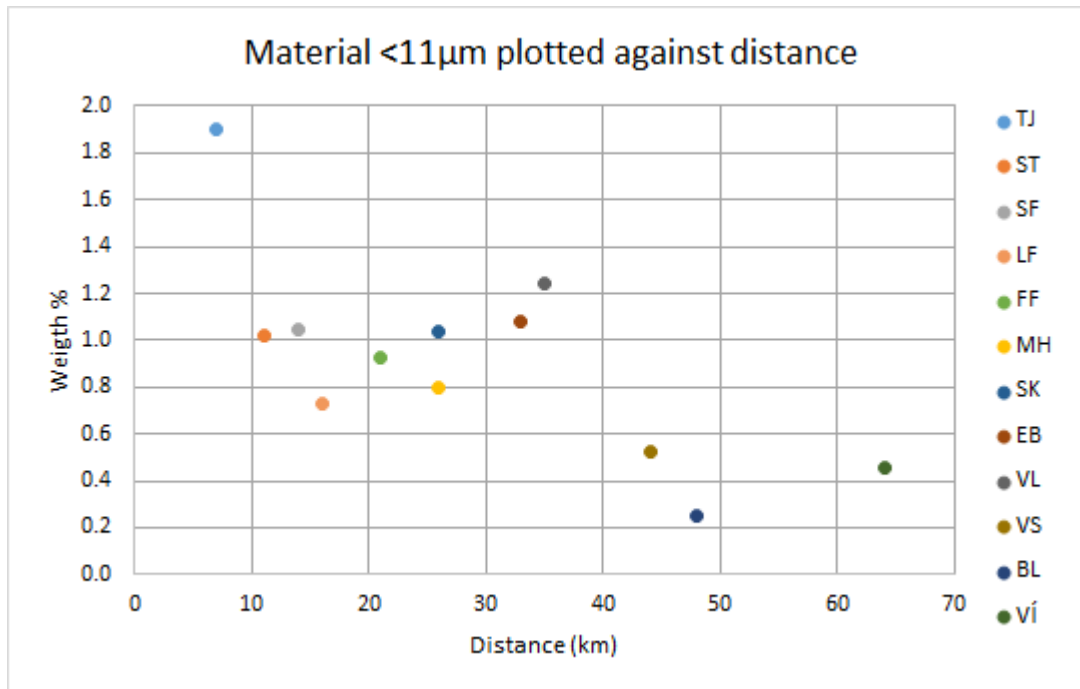


Figure 4-7: The material of the size finer than 11µm (6.5φ) against the distance from the volcanic source (Agnes Ösp Magnúsdóttir, 2014).

When looking at Figure 4-7 there is the same trend as in Figure 4-5 and Figure 4-6. Where the fine material decreases with the distance from the volcanic source. Although the material finer than 11µm differs a bit from one place to the next it is obvious that the material as a whole, seen in Figure 4-7, is decreasing with distance.

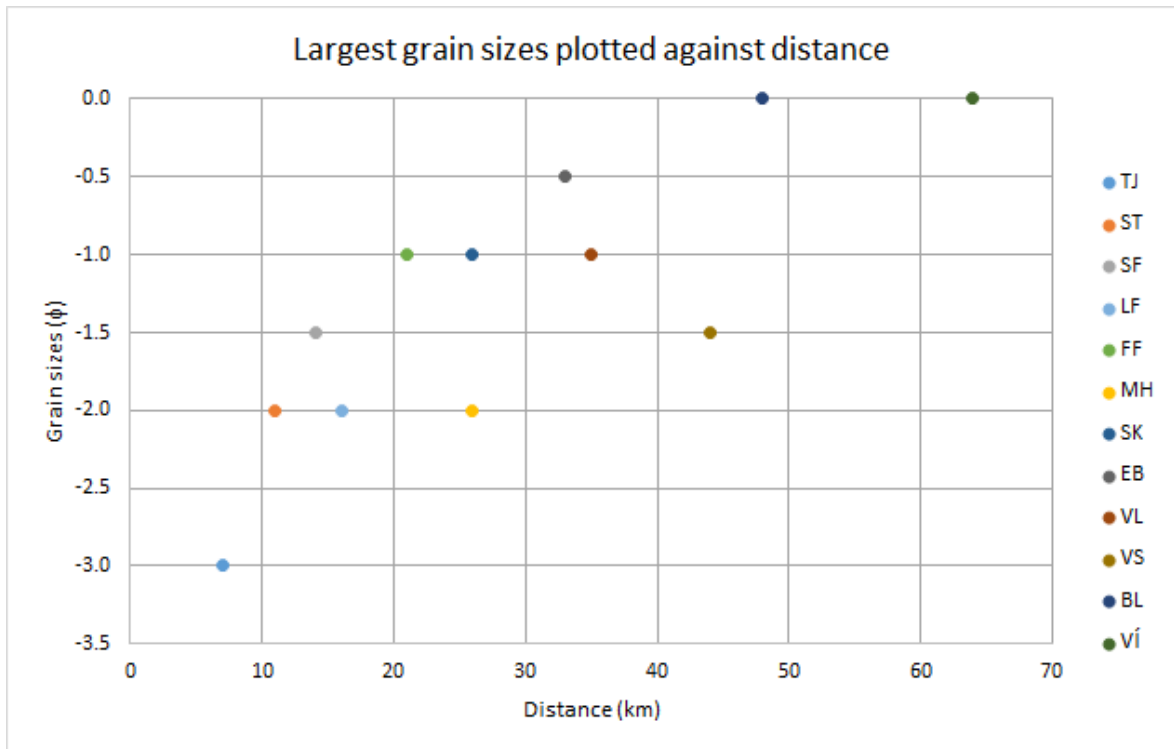


Figure 4-8: The largest grains presented on the phi scale for each sample plotted against the distance from the source (Agnes Ösp Magnúsdóttir, 2014).

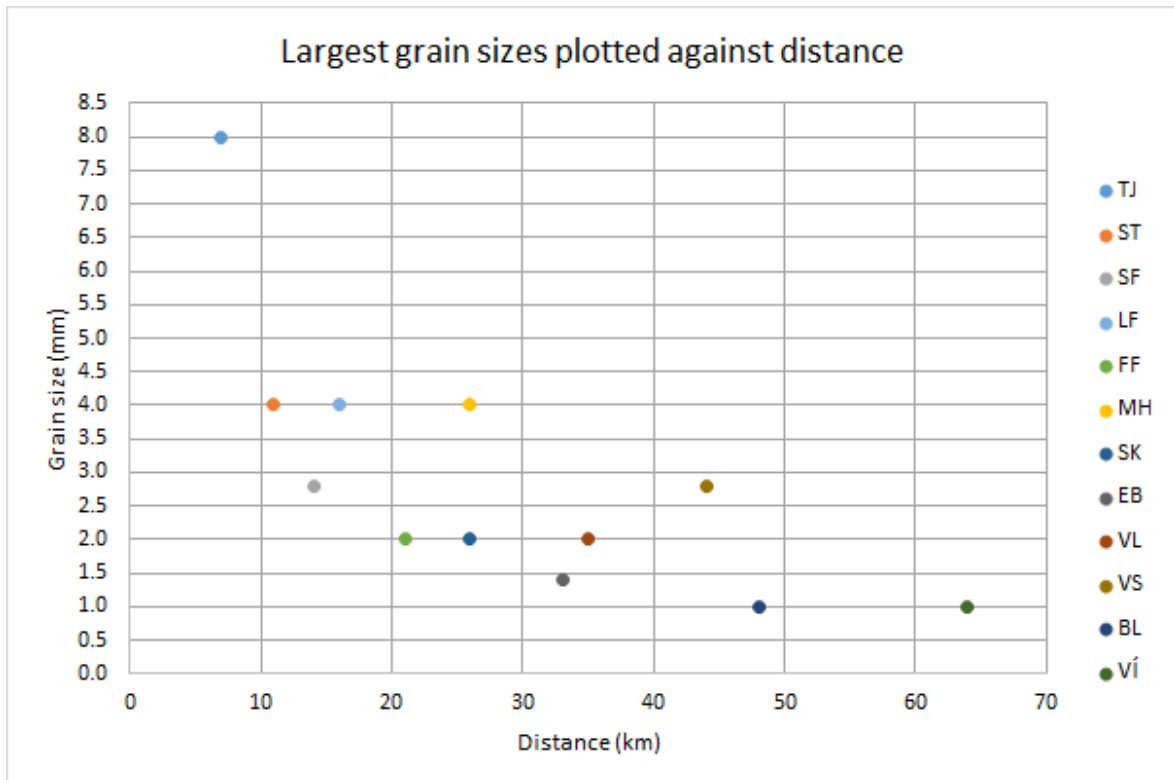


Figure 4-9: The largest grains presented in millimeters in each sample plotted against the distance from the source (Agnes Ösp Magnúsdóttir, 2014).

When looking into how far the largest grains travel, the largest grain class found is plotted against the distance from the source. The grain size is both shown on the phi scale in Figure 4-8 and in millimeters in Figure 4-9. Both these figures show how the largest grains in each sample become smaller the further away from the source they were sampled.

The largest grains probably are within 11 km from the source where the largest grains are -3.0 ϕ or 8 mm. At distances from 11 km to 42 km from the volcanic source the largest grains are -2.0 ϕ to -0.5 ϕ or 4 to 1.4 mm. At distances greater than 42 km from the volcanic source the biggest grains are 0.0 ϕ or 1 mm.

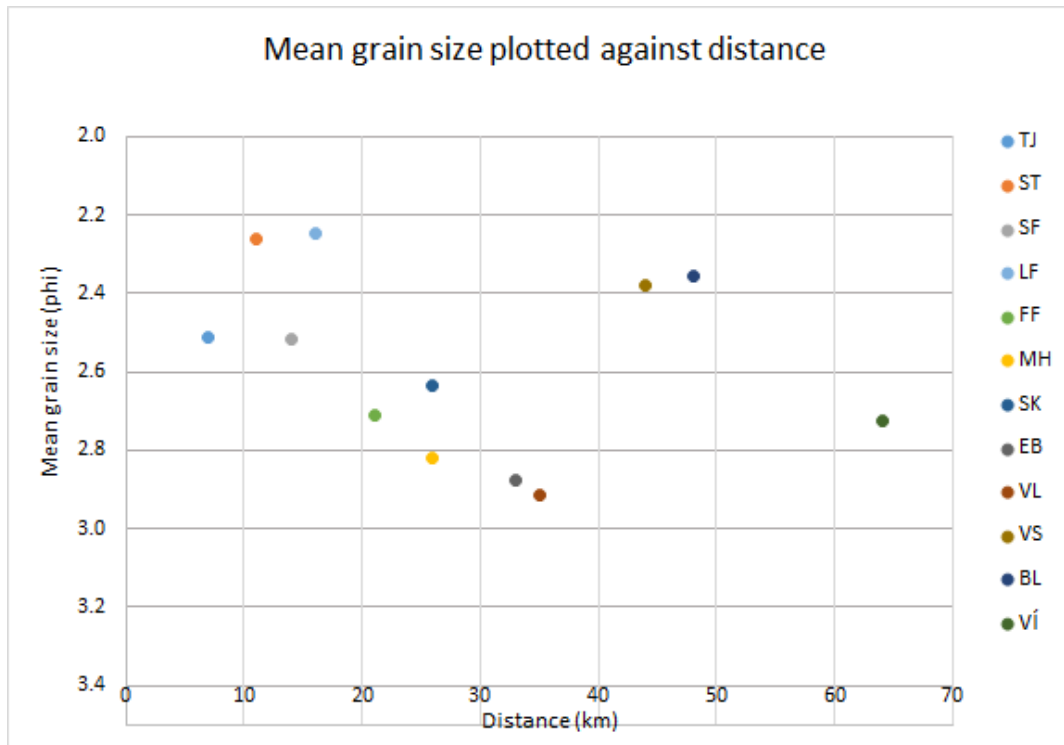


Figure 4-10: The mean grain size plotted against the distance from the source. The mean grain sizes are here shown on the phi scale (Agnes Ösp Magnúsdóttir, 2014).

The mean grain size of each sample is plotted against the distance from the source. Figure 4-10 shows that the mean grain size does not change much with increasing distance from the source. However, a slight difference can be seen. Sampling locations TJ and SF only represent a portion of the layer since the sample taken was not a bulk sample so the mean grain size at these two locations could be a little distorted. So ignoring those two locations and looking only at locations between ST at 11 km. distance and VÍ at 64 km. distance, it is clear that there is a little difference in the mean grain size but even so the VÍ sample has a little bit finer mean grain size than the ST sample.

The mean grain size and the sorting don't change much with distance as shown in Figure 4-2, the small changes tell us that the mean grains size decreases with distance from the volcanic source and the samples get better sorted the further away they are from the source.

4.2 Total grain size

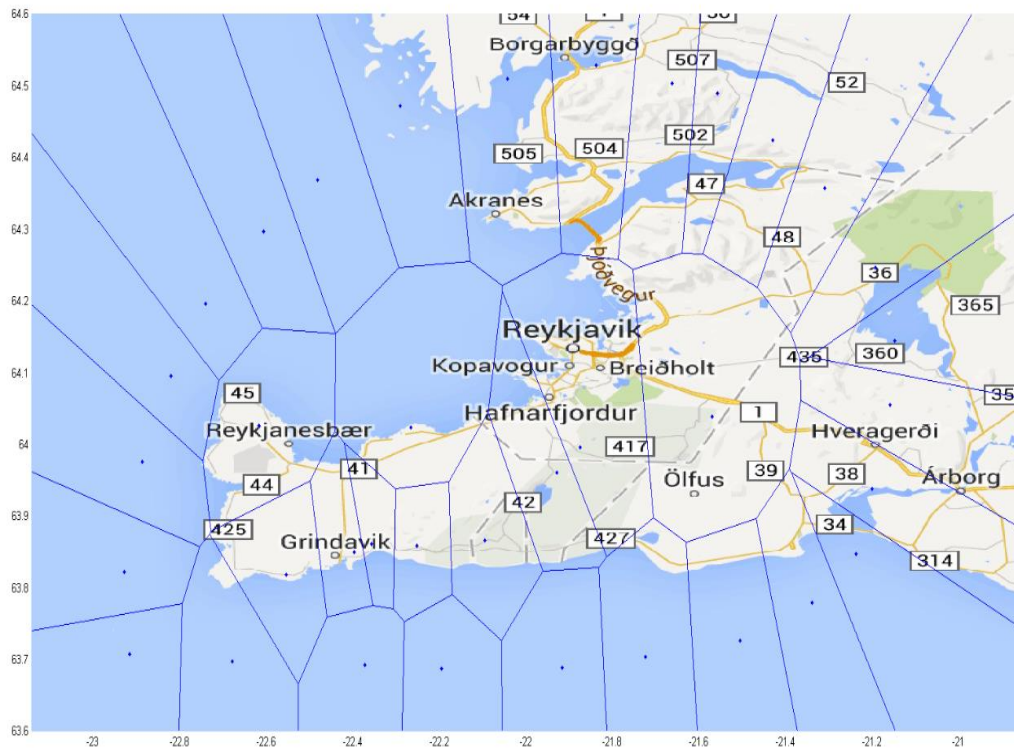


Figure 4-11: Shows how the Voronoi cells are distributed for the area that the ash layer covered (Agnes Ösp Magnúsdóttir, 2014).

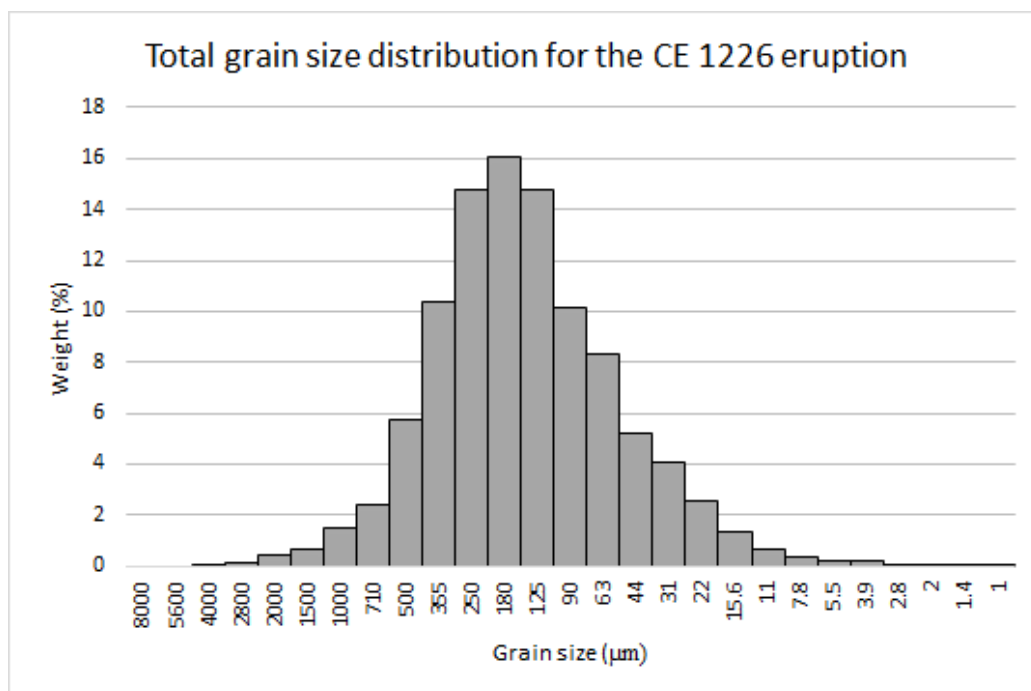


Figure 4-12: The total grain size distribution for the Medieval tephra layer with the Voronoi method (Agnes Ösp Magnúsdóttir, 2014).

The Voronoi method was applied to the CE 1226 eruption, using only bulk samples to avoid any possible bias. This method combines all obtained grain size distributions, giving each location a representative area. The total mean grain size distribution for the whole layer is shown in Figure 4-11. It is obtained as the weighted mean of the cells. The area representing each grain size distribution can be seen in Figure 4-11 and further results from this method are shown in Table 2.

Table 2: Result from the Voronoi method for the total grain size of the Medieval tephra layer.

	phi	mm
Median	2.4015	0.1893
Std. dev.	-1.2042	2.3041

When looking at Figure 4-10 it can be seen that the mean grain size of most of the samples is finer than the total grain size found using the Voronoi method according to Table 2. This is to be expected since the Voronoi segments are of similar size regardless of distance to the vent. This implies that the cells closest to the vents have the largest amount of tephra and therefore have more effect on the total grain size distribution than those further away.

4.3 Shape analysis

In total, sixteen samples were measured using the particle shape analyzer but only eight were used for the data processing. Data for all the analyses are on a CD that comes with the thesis as an appendix.

4.3.1 Triangular plots

Two kinds of triangular plots were used to interpret the shape analysis of the Medieval tephra layer. One where the form factor, the feret aspect ratio and the fiber aspect ratio are used and another one where, the form factor, the compactness and the circularity are used. These factors were used to try to detect some changes in the shapes of the particles.

3.0 phi changes with distance

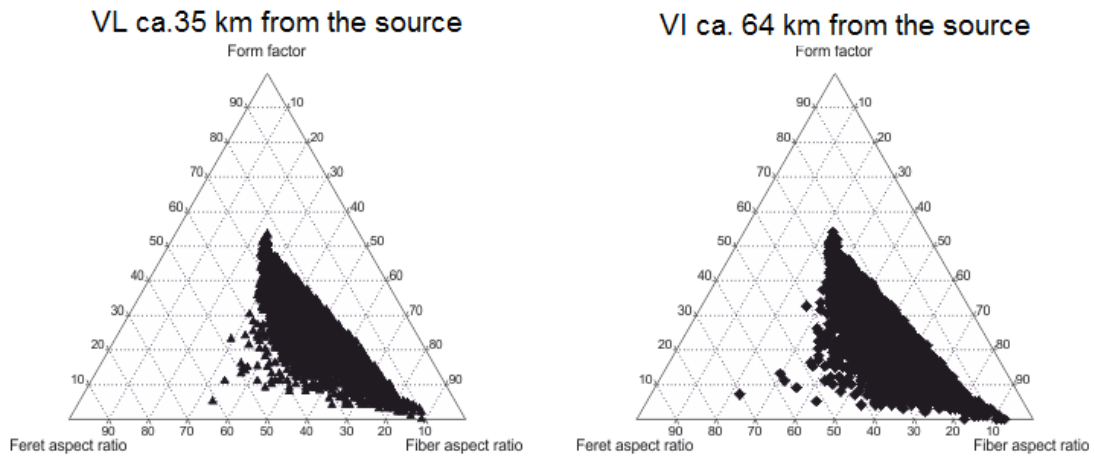


Figure 4-13: Triangular plots for 3.0 phi at various distances, the form factor scale has been scaled by 2.5 to get a better range in the data (Agnes Ösp Magnúsdóttir, 2014).

There is not much of a difference that can be detected between the two diagrams shown in Figure 4-13 where the shape parameters are the form factor, the ferret aspect ratio and the fiber aspect ratio. In these diagrams the form factor has been scaled by 2.5 to get a better range in the dataset hoping to detect some changes. Figure 4-13 shows that the grains have a form factor ranging between around 0% - 55%, a fiber aspect ratio that ranges from around 20% - ~90% and a feret aspect ratio that ranges from around 5% - 70%. Both diagrams seem to show this same trend so it is impossible to detect any real difference between them.

3.5 phi changes with distance

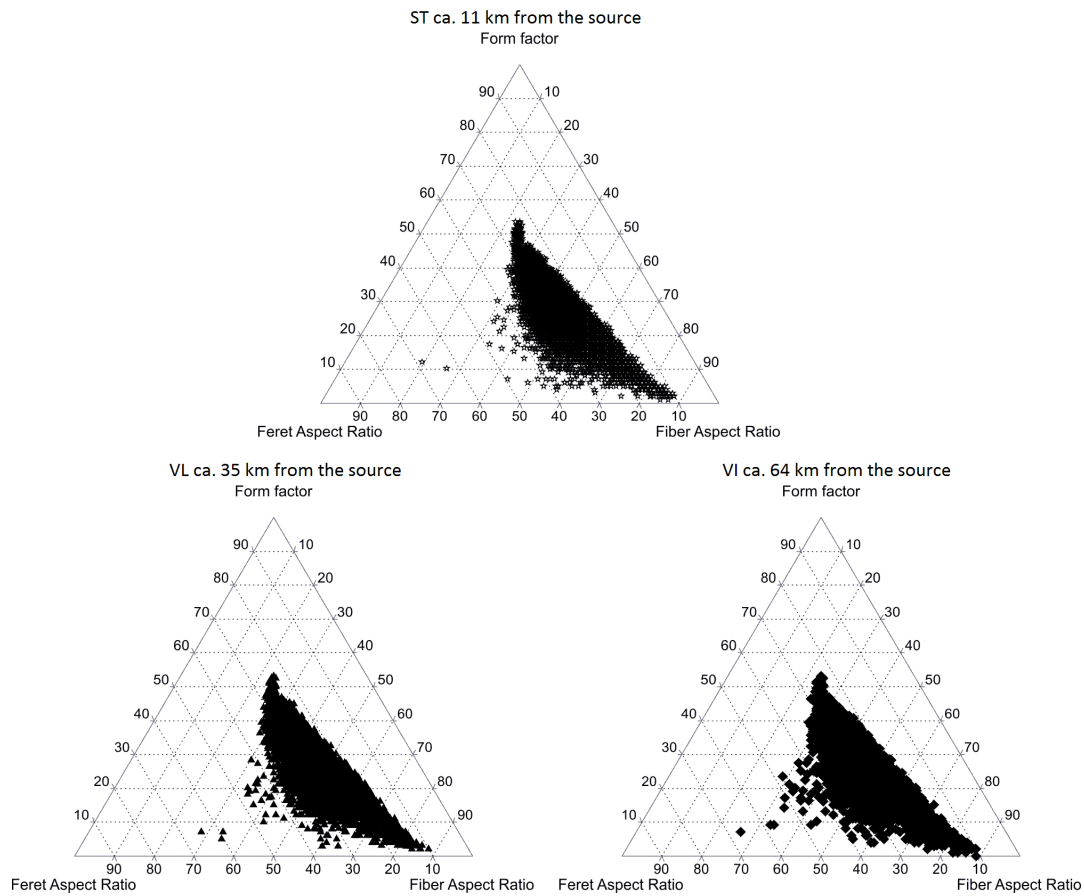


Figure 4-14: Triangular plots for 3.5 phi at various distances, the form factor scale has been scaled by 2.5 to get a better range in the data (Agnes Ösp Magnúsdóttir, 2014).

The three samples shown in Figure 4-14 don't seem to show that there is much difference in the grains shapes as the distance from the source grows. Furthermore Figure 4-14 seems to show the same trend and range in the dataset as Figure 4-13 does.

4.0 phi and below changes with distance

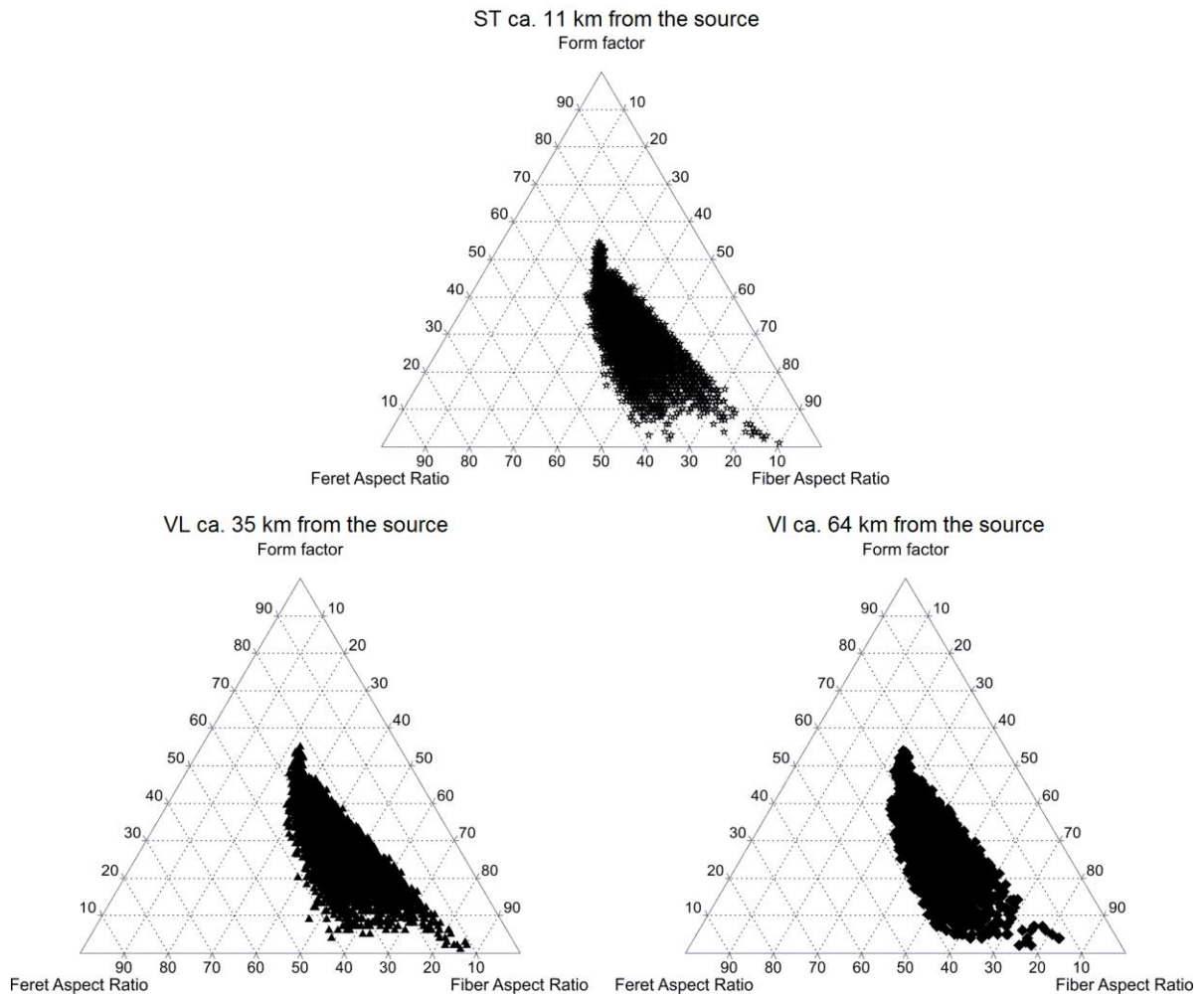


Figure 4-15: Triangular plots for 4 phi and finer at various distances, the form factor scale has been scaled by 2.5 to get a better range in the data (Agnes Ösp Magnúsdóttir, 2014).

When looking at the results from the shape analysis of the material finer than 4 phi it can be seen that the dataset has a similar trend as the datasets of the grain sizes 3.5 phi and 3.0 phi on Figure 4-13 and Figure 4-14 but the range is not exactly the same as the form factor ranges from 0% - 55%, the fiber aspect ratio from 20% - 90% and the feret aspect ratio from 10% - 45%. A slight difference can be seen between the sample places, the sample that is furthest away from the volcanic vent is more compressed than the other two. The focus rejection on the particle shape analyzer prevents very small grains to be analyzed so the smallest grains that are analyzed are about 20-30 μm .

3.0 phi changes with distance

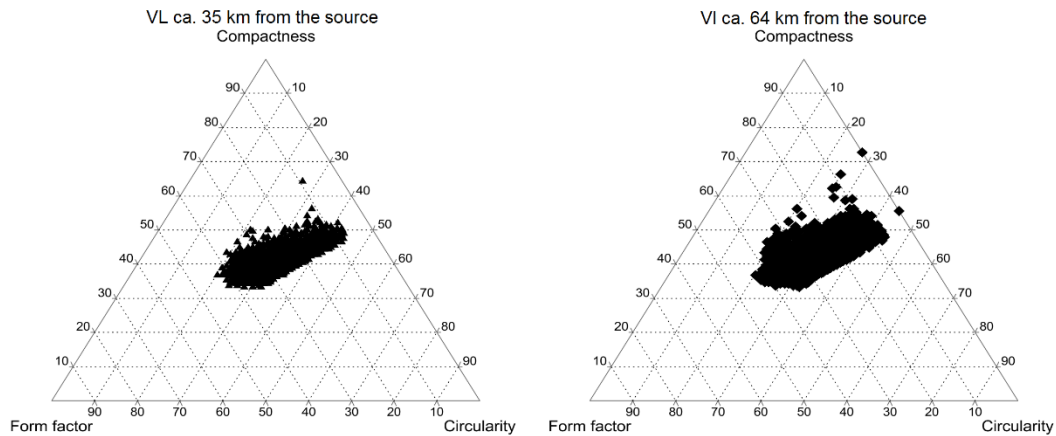


Figure 4-16: Triangular plots for 3.0 phi at various distances, having form factor, compactness and circularity in the corners (Agnes Ösp Magnúsdóttir, 2014).

Compactness, circularity and form factor are used to interpret the data from the shape analysis and they seem to show a different trend than the other type of triangles did. The data range is from 30% - ~70% in compactness, 20% - 45% in circularity and 0% - 55% in form factor. The datasets on Figure 4-16 don't seem to show difference with distance from the source.

3.5 phi changes with distance

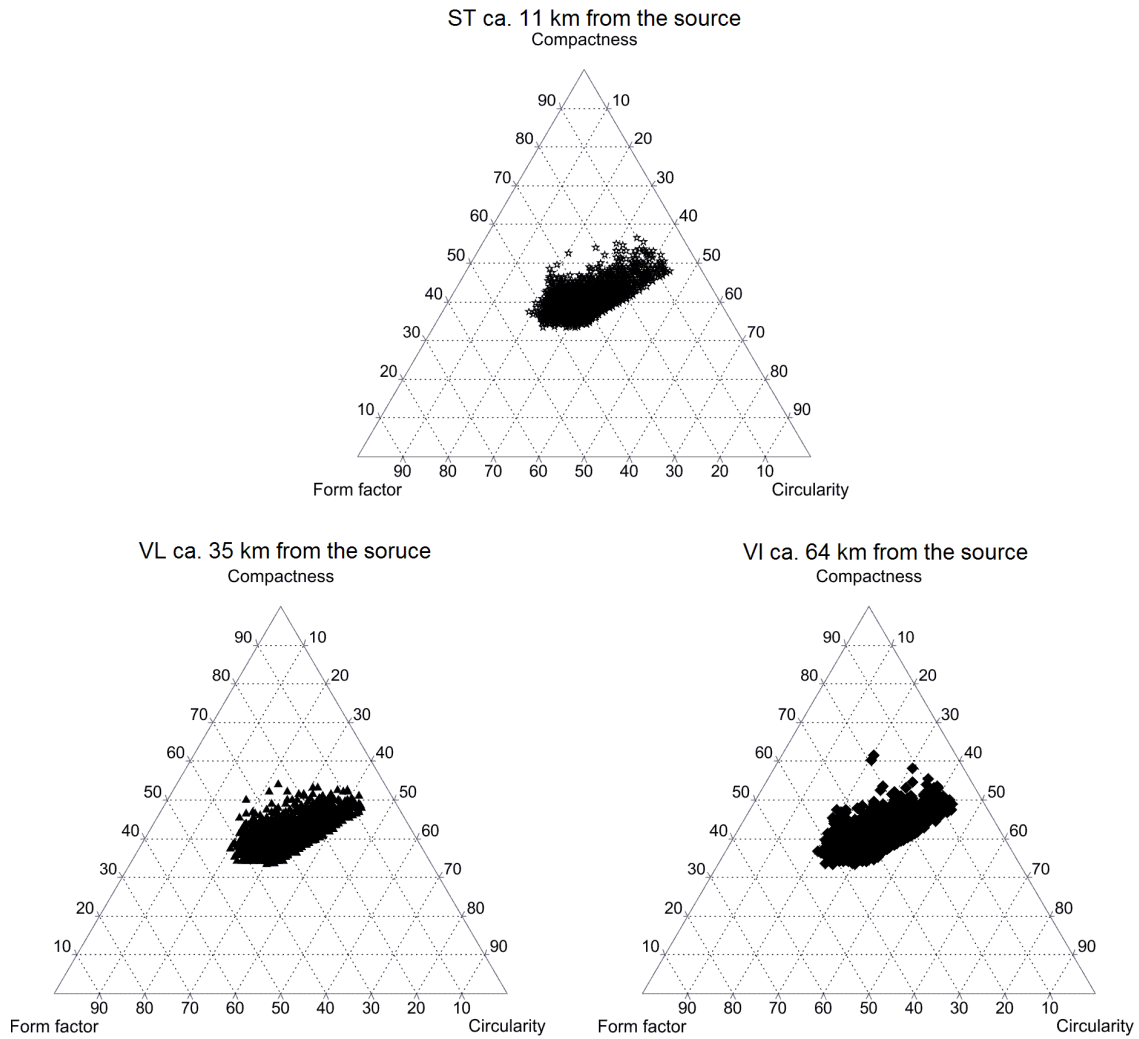


Figure 4-17: Triangular plots for 3.5 phi at various distances, having form factor, compactness and circularity in the corners (Agnes Ösp Magnúsdóttir, 2014).

3.5 phi, shown in Figure 4-17, seem to show the same trend as Figure 4-16 and the data also seem to have the same range as before. This grain size doesn't seem to show any particular changes with distance regarding the previously mentioned shape parameters.

4.0 phi and below changes with distance

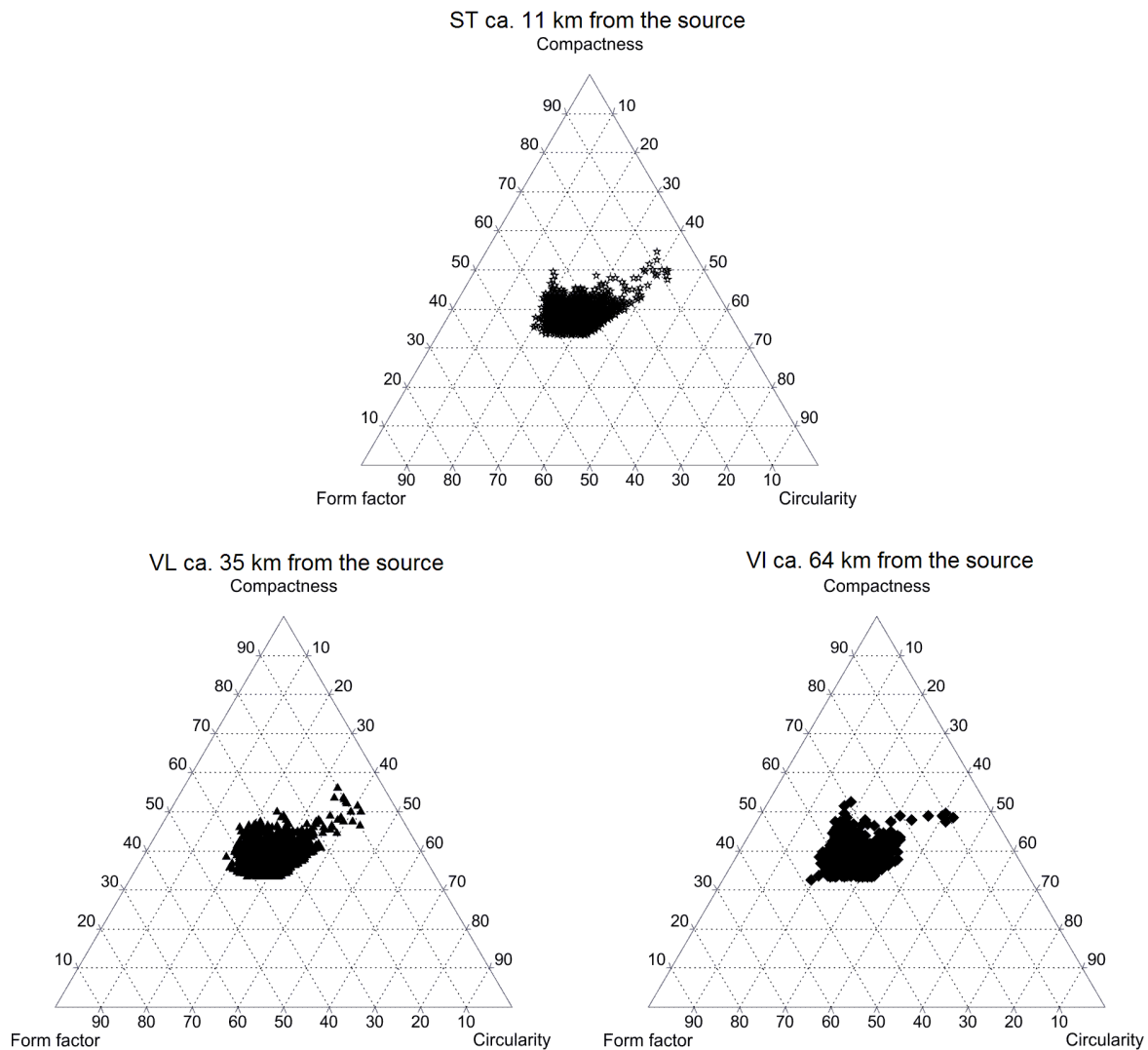


Figure 4-18: Triangular plots for 4 phi and everything below that size at various distances having form factor, compactness and circularity in the corners (Agnes Ösp Magnúsdóttir, 2014).

When looking at the shape data for the finest grain sizes shown on Figure 4-18 there seems to be the same underlying trend as before in the other triangular plots of this type but the data range doesn't seem to be the same as seen in Figure 4-16 and Figure 4-17. Here the data range is smaller since the shape forms a cluster that becomes more compact with distance from the source. The fine materials seem to show a slight difference in shape with distance from the source when looking into these three parameters.

To conform the results from the shape analysis a two tailed t-test was done to find out if there was significant difference between sample places. The t-test was done on all parameter used in the triangular plots and the frequency plots for both 3.5 phi and 4 phis and below. The results from the t-tests are shown in appendix V, the main result from the t-test is that there is, in almost all cases significant statistical difference exists between samples collected at different distances.

4.3.2 Frequency graphs

Frequency plots were made with the data using the ellipse aspect ratio and the circularity. This is done to try to see if any changes occur with distance. These frequency plots were done using circularity and ellipse aspect ratio using samples of three different distances from the source, 11 km, 35 km, and 64 km and three grain sizes 3.0 phi, 3.5 phi and 4 phis and below.

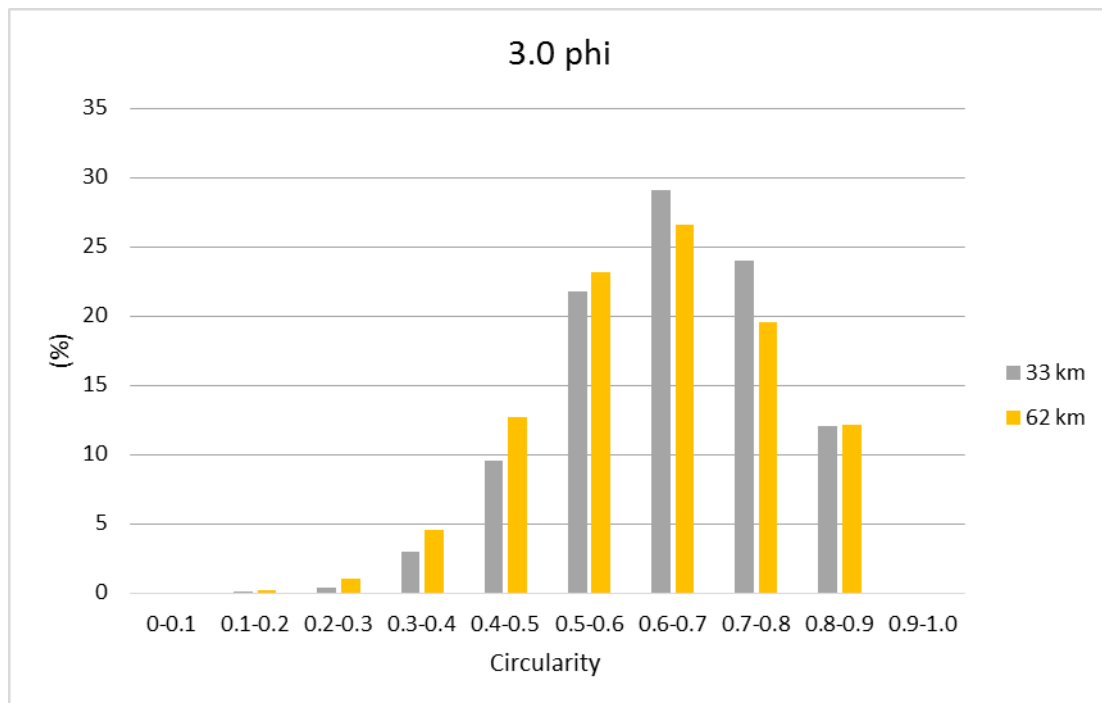


Figure 4-19: Frequency of the measured circularity at two different distances from the source (Agnes Ösp Magnúsdóttir, 2014).

Figure 4-19 shows the frequency of circularity in two samples one from 35 km and the other one from 64 km from the volcanic source. These two samples show the same trend and have a high peak at the same circularity intercept. But as shown in appendix V that although there doesn't seem to be much of a difference between these two samples the combined t-test tells that there is a statistical difference between these two samples.

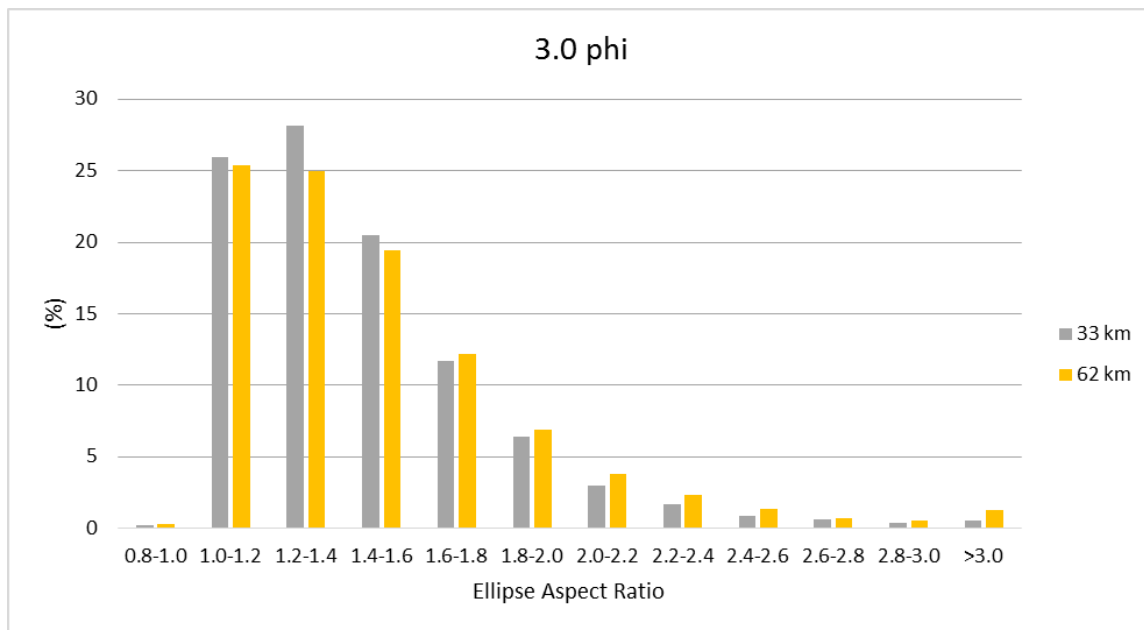


Figure 4-20: Frequency of the measured ellipse aspect ratio at two different distances from the source (Agnes Ösp Magnúsdóttir, 2014).

Figure 4-20 shows that the frequency of the samples don't behave in the same way, the high peak is not in the same place in the samples. The statistical analysis show in appendix V tell us that there is a significant difference between these two sample places when looking at the ellipse aspect ratio.

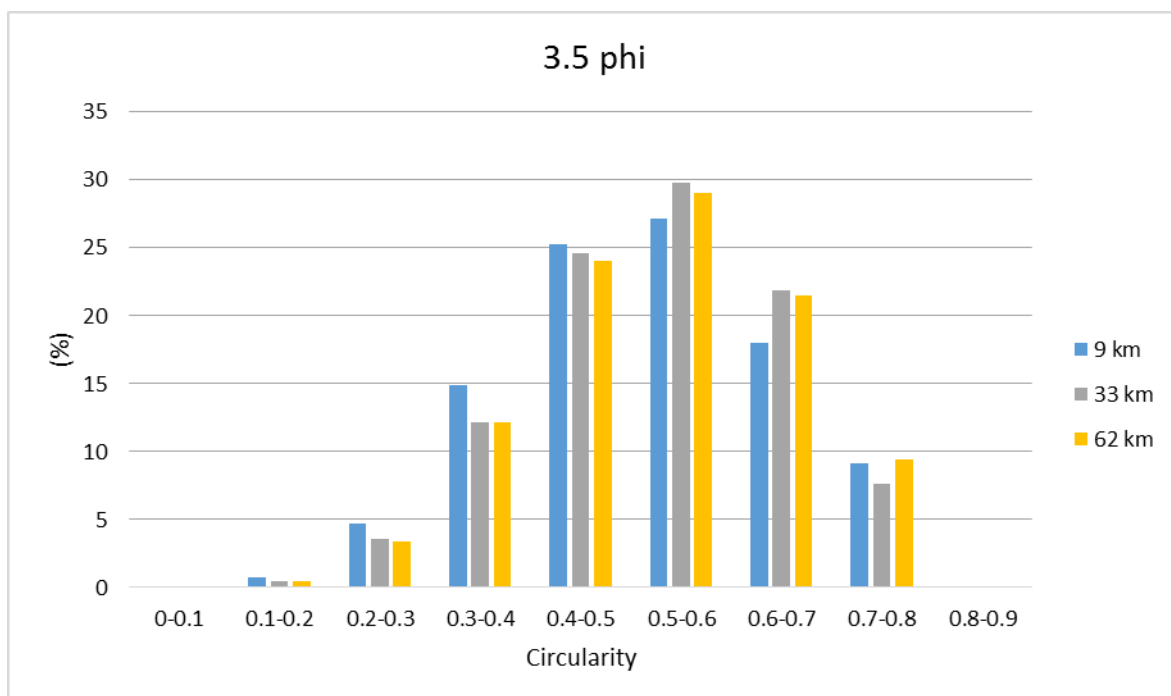


Figure 4-21: Frequency of the measured circularity at three different distances from the source (Agnes Ösp Magnúsdóttir, 2014).

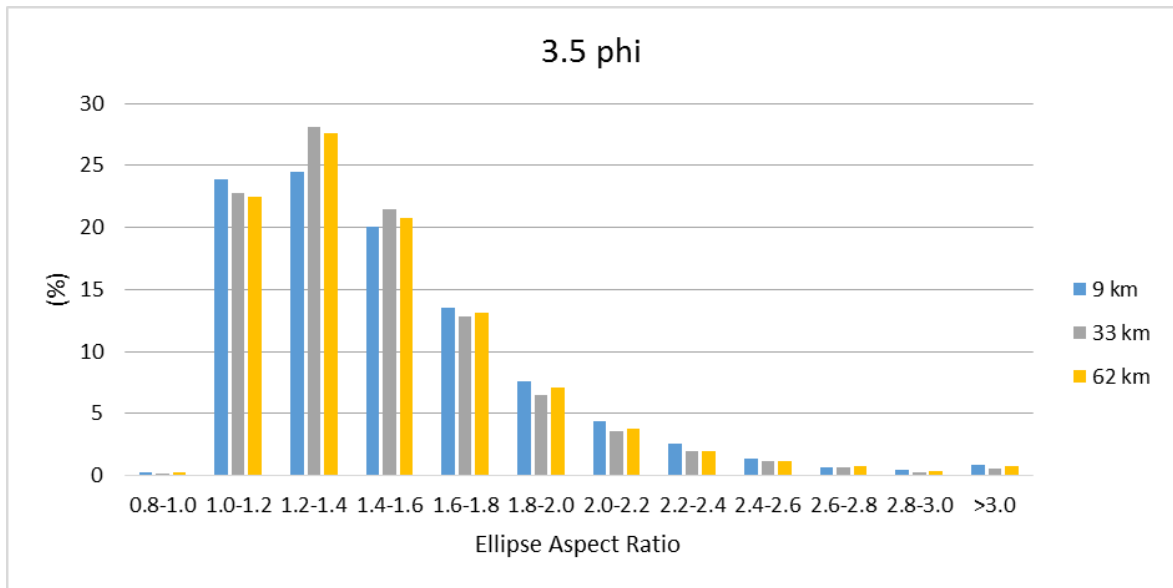


Figure 4-22: Frequency of the measured ellipse aspect ratio at three different distances from the source (Agnes Ösp Magnúsdóttir, 2014).

Both the circularity on Figure 4-21 and the ellipse aspect ratio on Figure 4-22 seem to show the same trend. The Circularity always has the same peak in frequency so it could be concluded that it doesn't change with distance from the volcanic source. The same thing applies to the ellipse aspect ratio, the peak is always in the same place and all sample points seem to have the same trend. But by looking into the statistical data in appendix V that tell us that there is a significant difference between all samples both in the circularity and the ellipse aspect ratio.

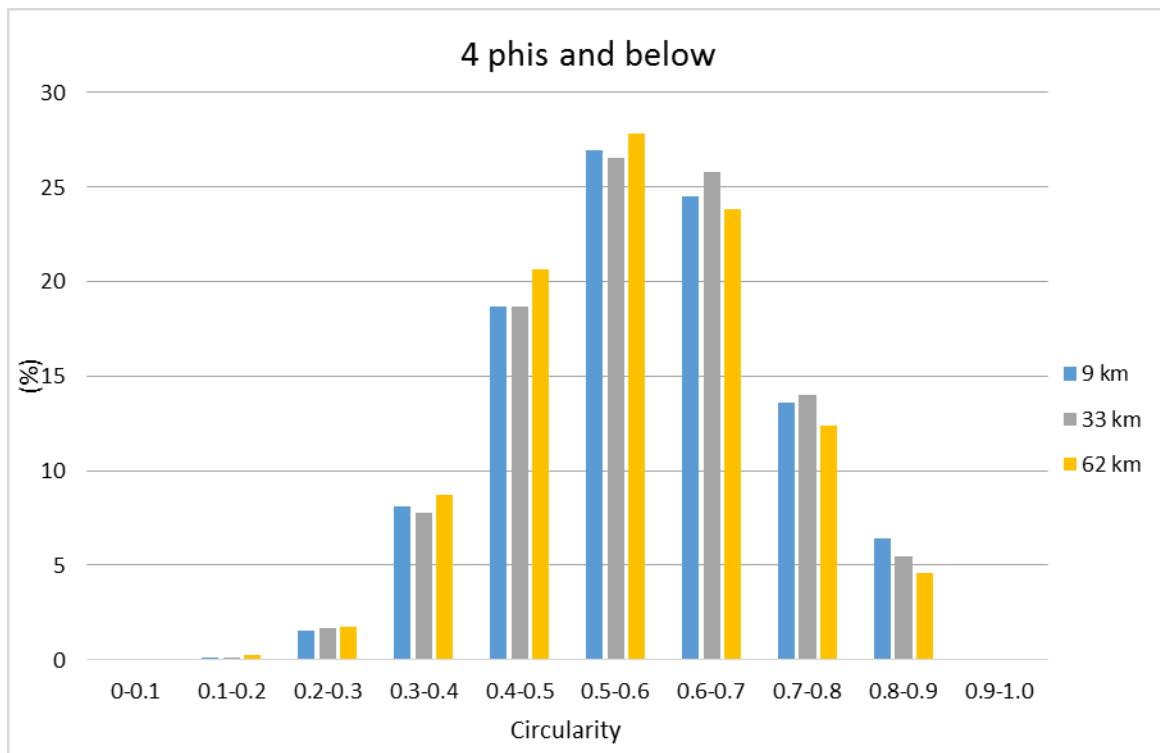


Figure 4-23: Frequency of the measured circularity at three different distances from the source (Agnes Ösp Magnúsdóttir, 2014).

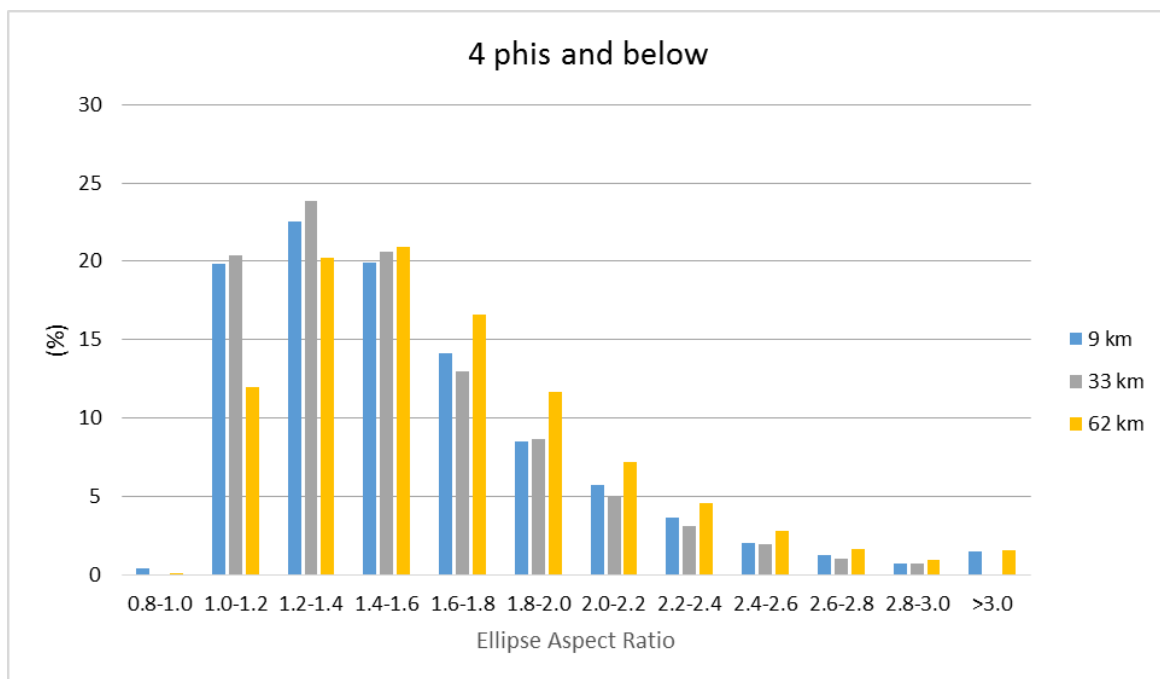


Figure 4-24: Frequency of the measured ellipse aspect ratio at three different distances from the source (Agnes Ösp Magnúsdóttir, 2014).

Figure 4-23 shows the frequency of the measured circularity at three various distances from the volcanic source. The peak is at the same circularity interval in all of the samples and the samples also have the same frequency dispersion. The statistical data in appendix V show that there is not a statistical difference between 11 km from the source and 35 km from the source in the circularity. But there is a statistical difference between 35 km. and 64 km. and also between 11 km. and 64 km. from the volcanic source.

The frequency of the measured ellipse aspect ratio in Figure 4-24 doesn't seem to have the same trend in dispersion for all the samples. The peak is at 1.2-1.4 for two of the samples, 11 km. and 35 km. from the source, but at 1.4-1.6 for the sample that was taken the farthest away from the source or at a distance of 64 km. The statistical data in appendix V show that there is a statistical difference between all sample places. Therefore it can be concluded that the ellipse aspect ratio changes with distance from the volcanic source in the grain size of 4 phi and below.

4.3.3 Shape plots

One of the way to find out if the shape changes with distance from the source is by multiplying three factors from the particle insight and plotting them against feret aspect ratio. The line shown on the graphs can tell if there is any changes between the two sample places. This line represents graphical average of the dataset. The graphical average measures how blocky a sample is, as the number of the graphical average increases the sample is more blocky as can be seen in Figure 4-25 and Figure 4-26 (Schmith, 2014).

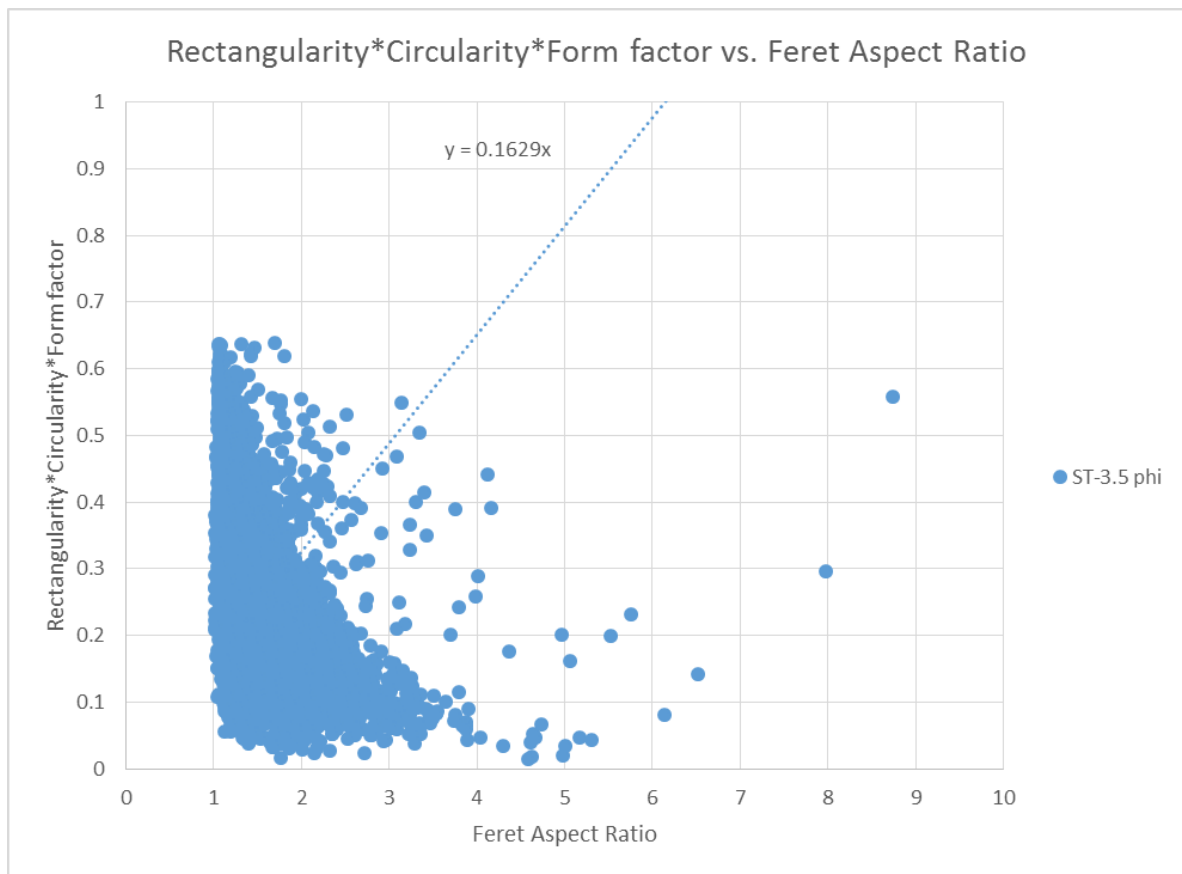


Figure 4-25: Rectangularity, circularity and form factor plotted against feret aspect ratio and has a trendline of $y=0.1629x$ (Agnes Ösp Magnúsdóttir, 2014).

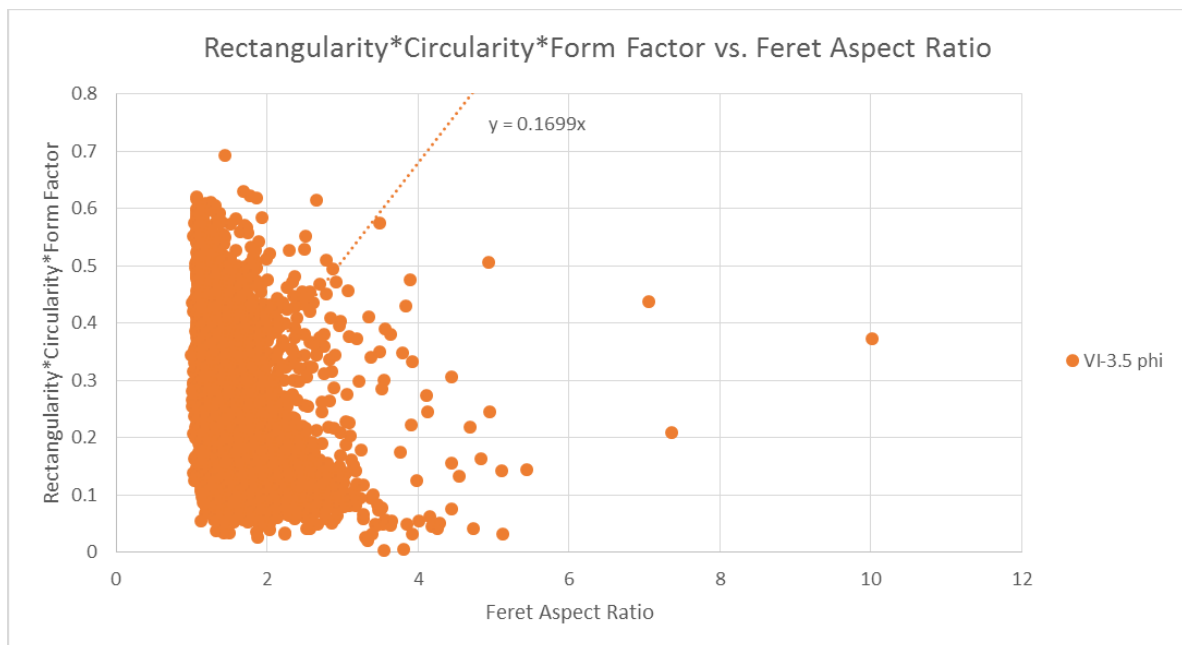


Figure 4-26: Rectangularity, circularity and form factor against feret aspect ratio, it has a trendline of $y=0.1699x$ (Agnes Ösp Magnúsdóttir, 2014).

4.4 Scanning electron microscope

The following images were taken with the SEM TM 3000 and show phreatomagmatic tephra grains from the CE 1226 eruption. The images show two selected grain sizes from various locations.

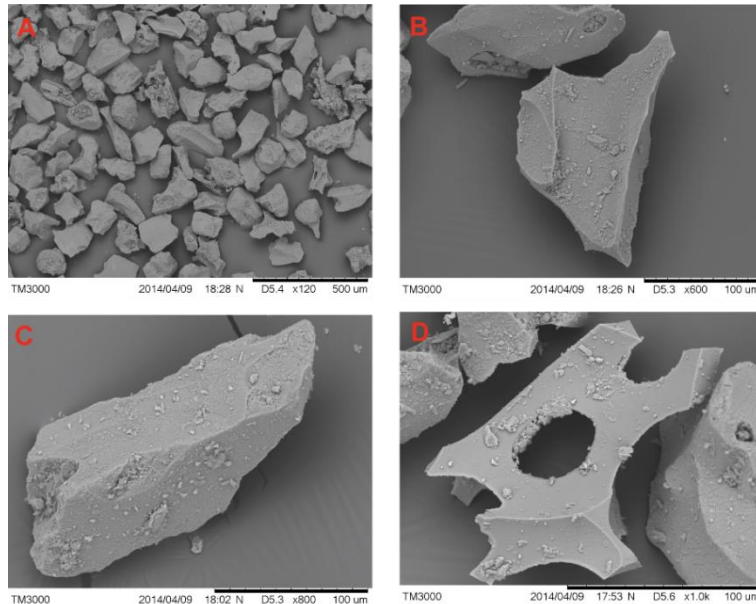


Figure 4-27: SEM images for the Medieval tephra layer. The grain size shown is 3.5 phi and the sample is taken 35 km from the source. (A) shows an overview of the tephra grains for this sample place, (B) shows a vesicle-growth tephra grain, (C) shows a typical bulky grain and (D) is another vesicle-growth grain (Agnes Ösp Magnúsdóttir, 2014).

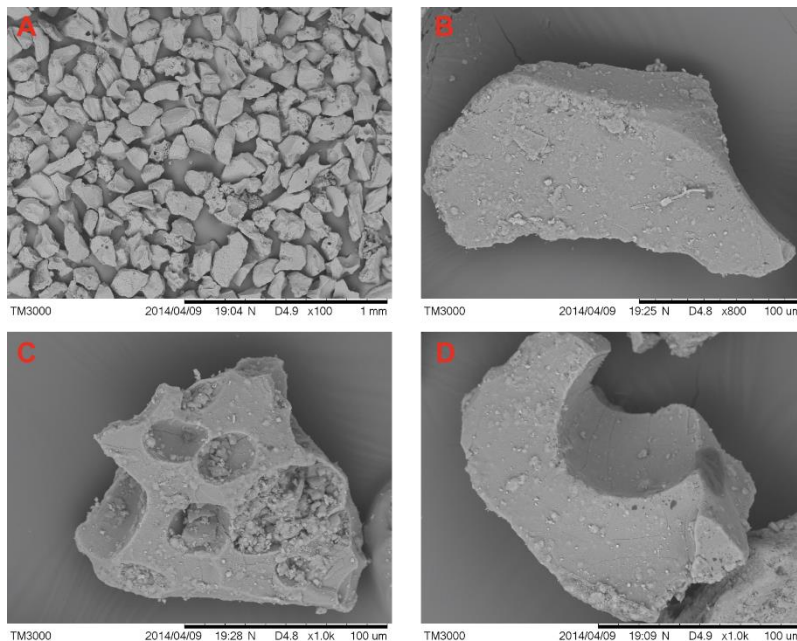


Figure 4-28: Tephra from the Medieval tephra layer. The grain size shown is 3.5 phi and the sample is taken 46 km from the source. (A) shows an overview of the tephra sample, (B) is a typical bulky grain for this kind of an eruption, (C) is a bulky grain covered with small bubbles and (D) is a grain that is rather bulky but most likely had a big bubble inside (Agnes Ösp Magnúsdóttir, 2014).

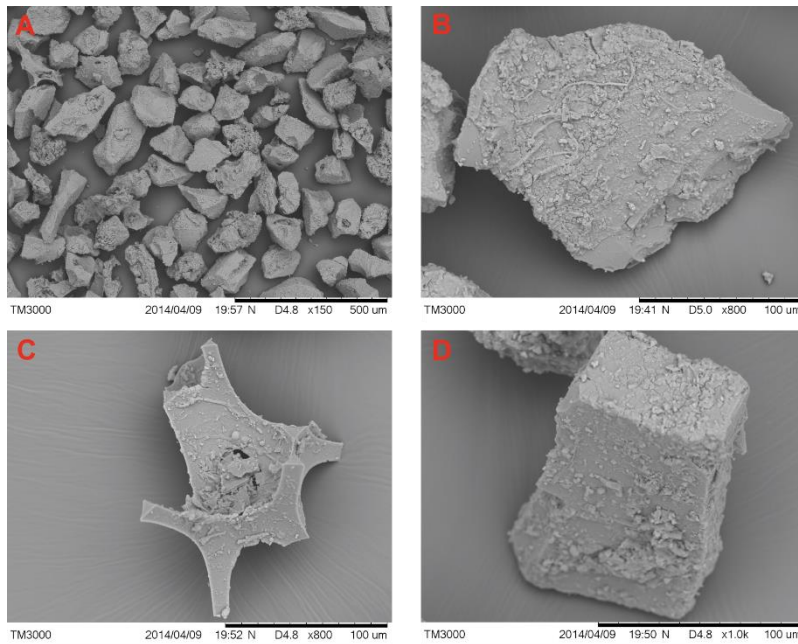


Figure 4-29: Tephra from the Medieval tephra layer. The grain size is 3.5 phi and the sample was taken 64 km from the source. (A) shows an overview of the sample, (B) is a bulky grain, (C) is a vesicle growth grain and therefore was a part of a bubble wall and (D) has a rather rhombic shape (Agnes Ösp Magnúsdóttir, 2014).

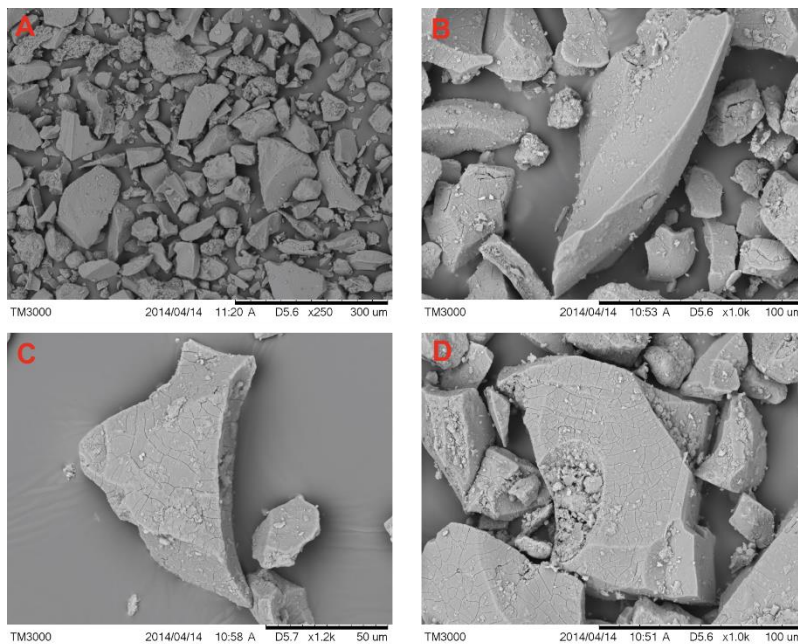


Figure 4-30: Tephra from the Medieval tephra layer. The grain size is 4 phi and everything below that and the sample is taken 35 km away from the source. (A) shows an overview of the grains in the sample, (B) is rather blocky angular grain with stepped surfaces, (C) is also rather angular and blocky with stepped surfaces and (D) is blocky angular grain that had a small bubble inside (Agnes Ösp Magnúsdóttir, 2014).

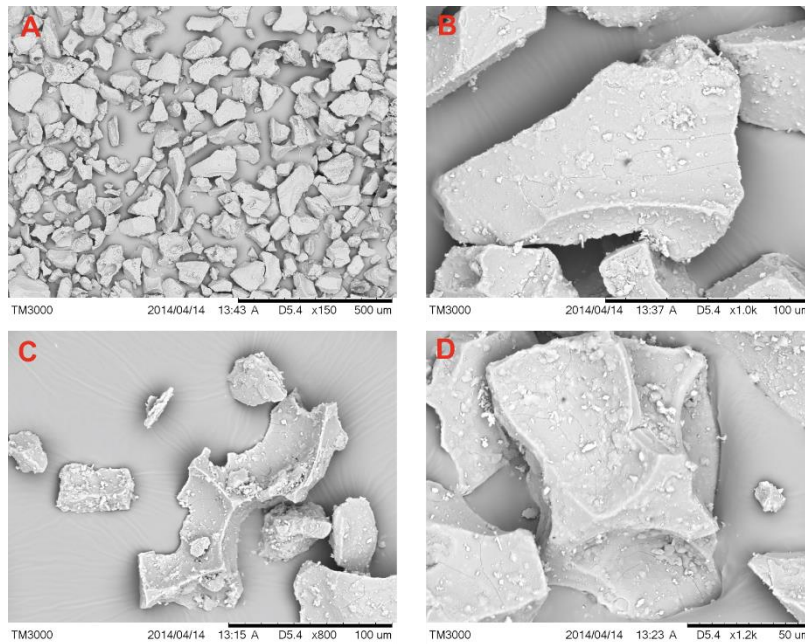


Figure 4-31: Tephra from the Medieval tephra layer the grain size is 4 phi and everything below and the sample is taken 46 km from the source. (A) shows a rather typical overview of tephra grains in this sample, (B) shows an angular and blocky tephra grain with stepped surfaces, (C) shows a vesicle growth controlled tephra grain and (D) a rather bulky grain, which has most likely been a part of bubble wall for a set of bubbles (Agnes Ösp Magnúsdóttir, 2014).

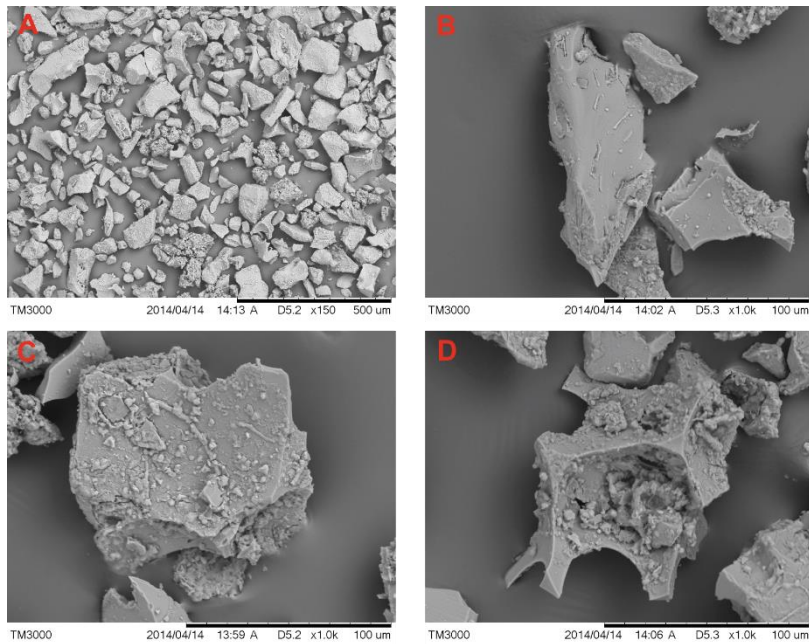


Figure 4-32: Showing tephra from the Medieval tephra layer. The grain size is 4 phi and everything below that, the sample is taken 64 km from the source. (A) shows a typical overview of tephra grains from this sample, (B) is rather angular and blocky tephra grain, (C) shows a blocky grain with stepped surfaces and (D) shows a tephra grain that is a vesicle grown tephra grain (Agnes Ösp Magnúsdóttir, 2014).

As the images in this chapter show the grains formed in this eruption fit into the category of phreatomagmatic ash. More SEM images are shown in appendix III. The tephra grains are angular and blocky shaped with stepped surfaces which is distinguishing for these kind of eruptions and a part of the grains have a vesicle controlled growth and have clearly been a part of a bubble wall. No shape analysis was done using the SEM instrument but by looking at the tephra sample it is indicated that most of the particles were blocky angular tephra grains with stepped surfaces. A part of the grains were clearly vesicular growth controlled tephra grains and had clearly been a part of a bubble wall. That may indicate that the magma had not been fully degassed at the time of the eruption.

4.5 Volume calculations

The area and thickness of the tephra layer are found from the isopach map (Figure 1-5) using ArcMap 10.2. Volume calculations were made with three different methods of power law, exponential thinning and Weibull. The volume had been previously calculated by Sigurgeirsson (1992) and it was found to be 0.1 km^3 . Information for these volume calculations were obtained using ArcMap and are shown in Table 3.

Table 3: The data for the Medieval tephra layer, t is the thickness in centimeters, A^ is the area that the layer covered in square meters and A is the area that it covered in square kilometers and then T is the thickness of the layer in kilometers.*

$t \text{ (cm)}$	$A^* \text{ (m}^2\text{)}$	$A \text{ (km}^2\text{)}$	$\text{Sqrt } A \text{ (km}^2\text{)}$	$T \text{ (km)}$
20	30715577.2	30.7	5.5	0.0002
10	125070954.7	125.1	11.2	0.0001
5	235605940.0	235.6	15.3	0.00005
2	852695337.8	852.7	29.2	0.00002
1	1616024684.9	1616.0	40.2	0.00001
0.5	3125573996.2	3125.6	55.9	0.000005

4.5.1 Exponential thinning

From Figure 4-33, which is made from Table 3, only one break in slope can be seen. The following information is read from the two slopes in Figure 4-33 and put in Table 4.

Table 4: Shows results for the exponential thinning method where T is the intercept, k is the slope of the line and BS is the break in slope.

$T1_0$	0.000448176
k_1	-0.1403
BS_1	15.349
$T2_0$	0.000111084
K_2	-0.057
BS_2	55.906

The information in Table 4 are then used to calculate the volume using equation 29. These calculation give a volume of 0.089 km^3 .

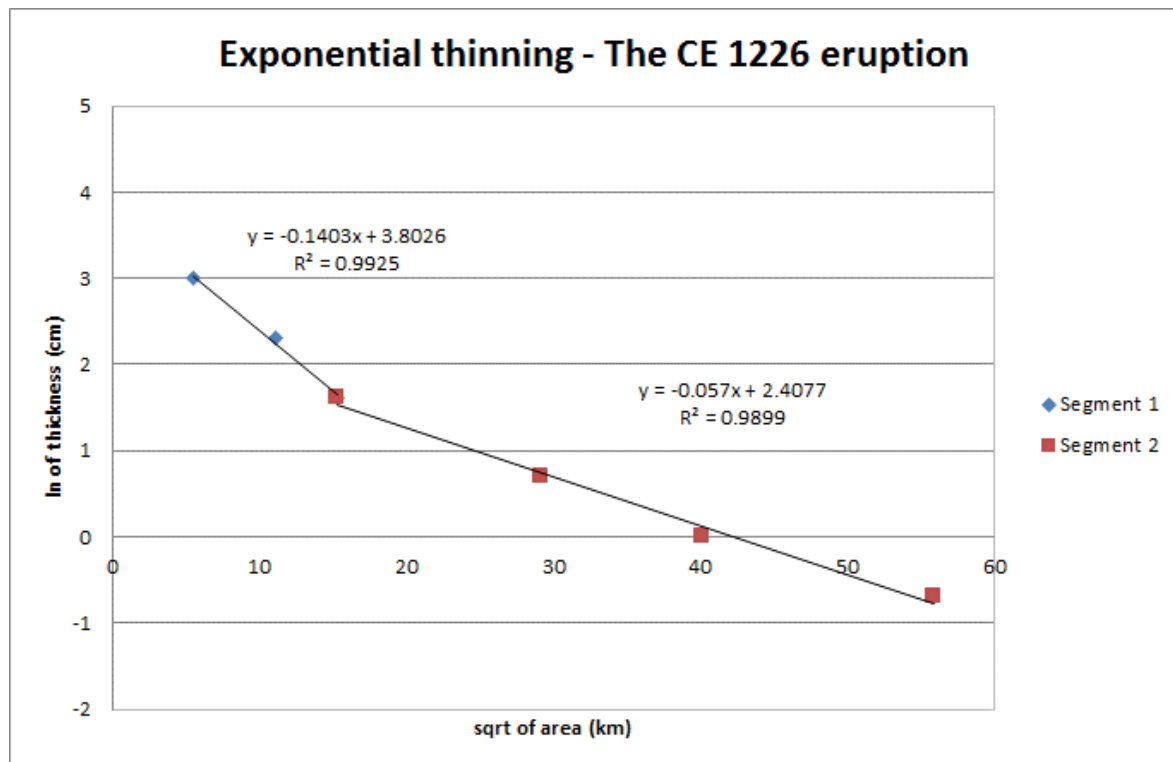


Figure 4-33: The plot for the exponential thinning method where \ln of the thickness of the layer is plotted against square root of the area. The line is split up in to two segments and each of them has its own intercept, slope and break in slope (Agnes Ösp Mangúsdóttir, 2014).

4.5.2 Power law

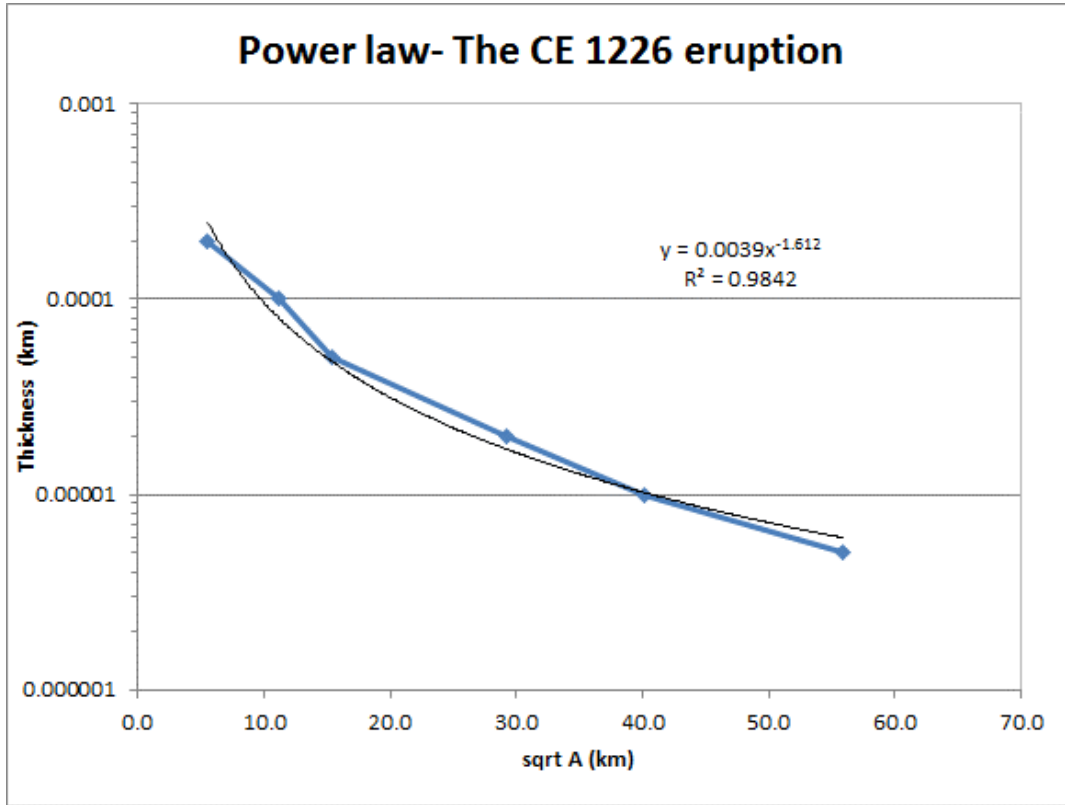


Figure 4-34: The power law fit for the CE 1226 eruption, showing the thickness in kilometers against the square root of the area that the layer covered (Agnes Ösp Magnúsdóttir, 2014).

The constant T_{pl} is 0.0039 and the power law coefficient m is 1.612 for this eruption. This information is put into equation 32 where B is defined as 5.5 and C as 55.9. These information are read from the slope of the line in Figure 4-34, C is underestimated because C is normally the downwind limit that is difficult to guess at for older layers but may work for contemporary eruptions where it may be found by using satellite images. In this case that limit is not known for the tephra dispersal and for that reason C is underestimated. If the downwind limit is increased it would result in a greater volume of the tephra layer.

This method gives a total volume of 0.49 km^3 .

4.5.3 Weibull method

The Weibull method is described in chapter 3.2.7, for making the fit n is 0.9575, θ is 3.394 cm and λ is 36.727 km. This method gives the volume to be 0.096 km^3 . The Weibull fit is shown on Figure 4-35.

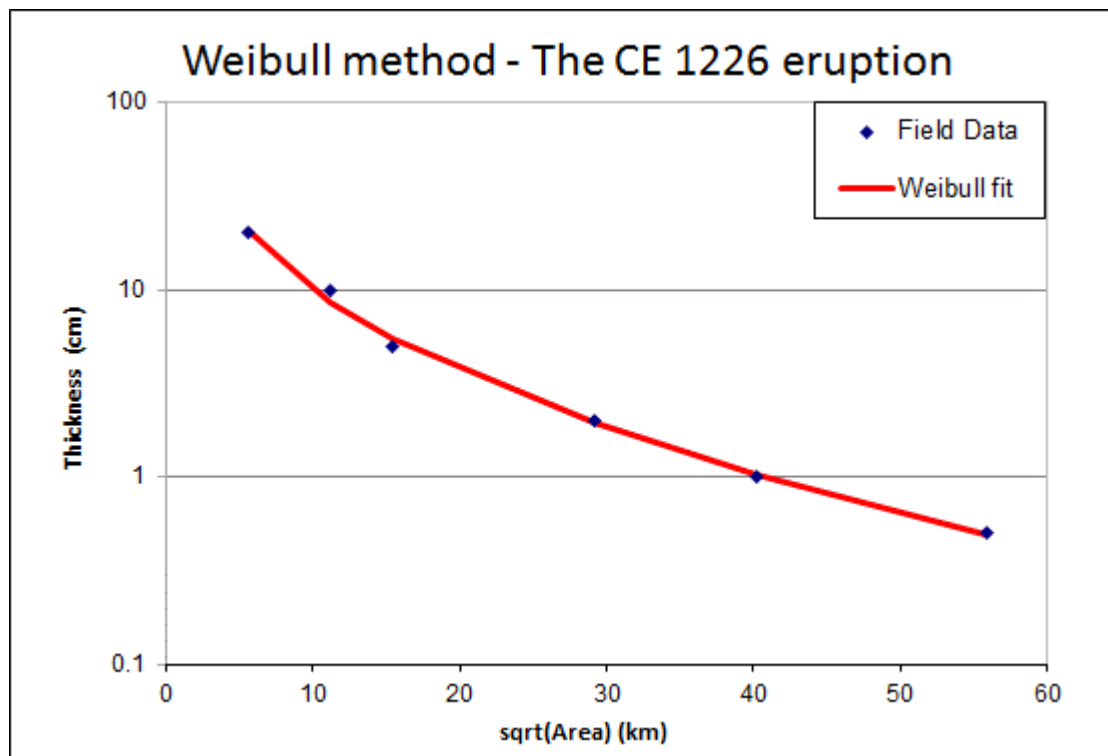


Figure 4-35: The Weibull fit for the Medieval tephra layer, the thickness in centimeters is plotted against the square root of the area (Agnes Ösp Magnúsdóttir, 2014).

5 Discussion

The source of the Medieval tephra layer cannot be exactly located and as said before that in this work it is estimated that it is 2.5 km from the coastline in southwest direction, which is the submarine continuation of the Reykjanes volcanic system. Since the sea part of the volcanic system is at less than 100 m depth as shown on Figure 1-4 it can be assumed that an eruption in that part of the volcanic system could produce an explosive volcanic eruption with tephra formation. In this chapter the main result from this work are discussed and the chapter is split up in to grain size analyzes, particle shape analyzes, volume calculations and scanning electron microscope (SEM).

5.1 Grain size analysis

The tephra from the Medieval tephra layer was analyzed down to 1 μm for twelve samples at various distances from the source see Figure 5-1. There is obviously a lack of fine materials preserved in the soil, compared to other phreatomagmatic eruptions. Changes in material finer than 63 μm are shown on Figure 5-2. It is most likely that not all the fine materials were preserved in the soil after the eruption took place and there can be several reasons for this, e.g. what time of the year the ash layer fell and that there had been a few eruptions in the years before the eruption in 1226 and therefore the fine materials did not bind with the soil since vegetation had not recovered after those eruptions. Furthermore this area is known to be rather windy so some of the material has likely simply been blown away. Figure 5-2 indicates that aggregation could be occurring since there is more of fine material near the volcanic vent but the amount of fine materials becomes less as the distance grows.

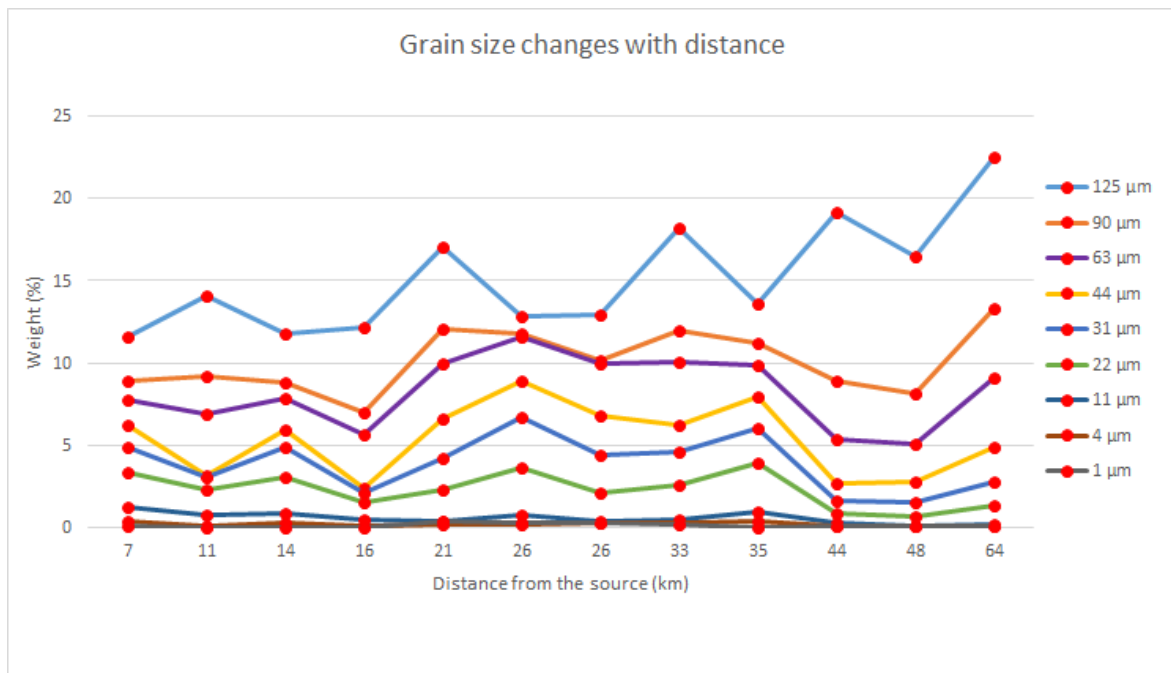


Figure 5-1: Changes in certain grain size classes with distance from the volcanic source (Agnes Ösp Magnúsdóttir, 2014)

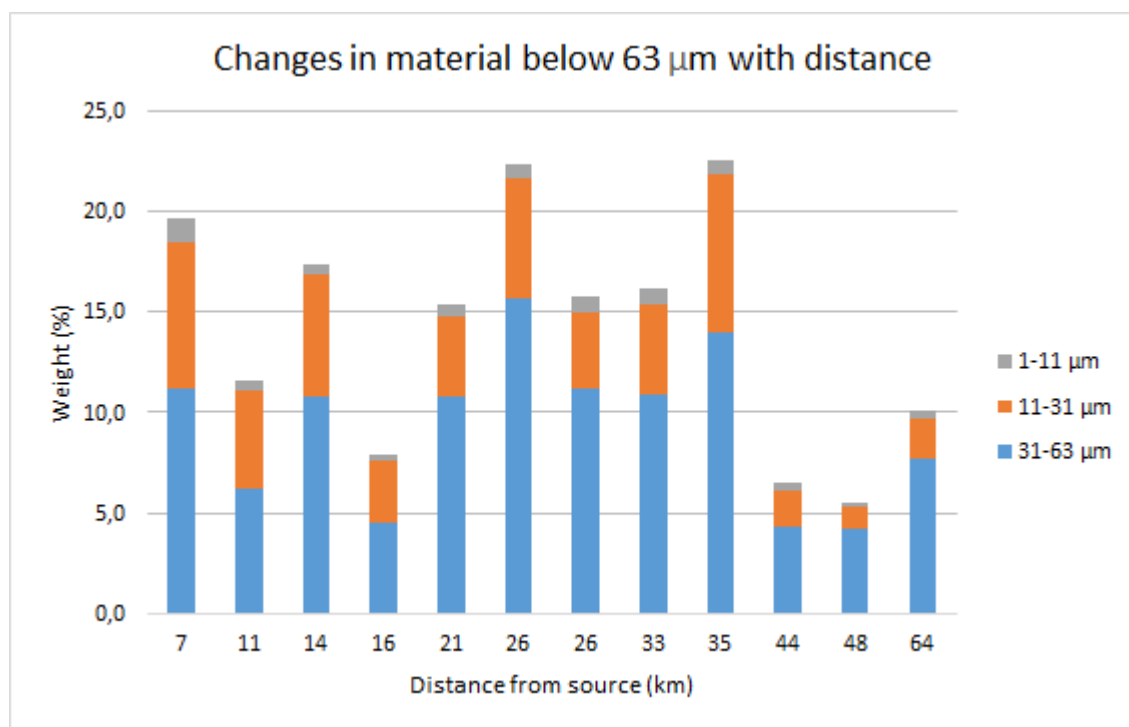


Figure 5-2: Changes in material below 63 µm with distance from the source, the material finer than 63 µm is split up in to three groups they are 31-63 µm, 11-31 µm and 1-11 µm (Agnes Ösp Magnúsdóttir, 2014).

When looking at what changes occur as the distance from the source increases, some clear trends emerge. Firstly, the mean grain size of the tephra layer decreases with distance from

the source. Secondly the sorting also changes with distance; the ash gets better sorted with distance. This is not surprising, as expected the larger grain sizes fall out near to the volcanic source.

The changes in the fine materials differ from one sample place to the next but there is not a trend in them with distance. This applies to all fine material classes studied in this way: (i) finer than 63 μ m. (ii) finer than or equal to 31 μ m and (iii) material finer than 11 μ m.

Material finer than 10 μ m is thought to be a special health hazard and can cause asthma or bronchitis. Particles of sizes 10-15 μ m can cause an irritation in the throat and nasal passages but most of the particles of these sizes will settle in the upper respiratory tract and that causes the irritation. But particles finer than 10 μ m that enter the bronchioles can cause lung irritation, inflammation, asthma or bronchitis (Horwell, 2007). As shown both on Figure 4-7 and Figure 5-2 the material finer than 11 μ m is between 1.9% and 0.14% of the whole sample. This amount of material finer than 11 μ m is small compared to what Horwell (2007) found for some volcanic eruptions e.g. the Fuego eruption in 1974 was a basaltic sup-plinian eruption and had 7.99% of material finer than 10 μ m, since there is most likely fine material missing from the CE 1226 eruption there is no way of knowing how much fine material existed at the time of the eruption.

In the Eyjafjallajökull eruption in 2010 the amount of fine materials produced by the eruption, during high magma discharge indicate that about 35-50% of the ash was finer than 63 μ m at distances of only 10-15 km from the summit. But these results don't show the presence of material under 63 μ m for the whole eruption, this eruption had many phases and they did not all produce the same amount of fine materials (Gudmundsson et al., 2012).

When looking at the largest grain sizes with distance from the source of the eruption the largest grains in each sample get smaller as the distance grows.

Total grain size calculations were done for the CE 1226 tephra layer. It gave that the mean grain size for the layer was 189 μ m. This mean grain size has considerable uncertainty. It could be made more accurate by adding more sample locations in the dispersal area. By increasing the number of sample spots each segment produced in the Voronoi method would be smaller and be more representative for the area within the segment. This should give a better estimate of segment mean grain size and therefore a more precise mean grain size of the whole tephra layer.

According to Figure 1-5 the main dispersal of the tephra layer is in a north-east direction but since this is a phreatomagmatic eruption the eruption has probably lasted for at least few days. Therefore it is very likely that the wind direction wasn't the same the whole time of the eruption and it is then likely that the dispersal of the tephra was considerably greater than that shown on the isopach map, possibly with tephra sectors extending out to sea that are not preserved on land.

5.2 Particle shape analysis

Two kinds of triangular plots were used to try to see changes in particle shape with distance from the volcanic source. Three grain sizes were used 3.0 phi, 3.5 phi and >4 phi. No changes could be detected with distance in the grain size classes of 3.0 phi and 3.5 phi in either type of the plots. But slight changes could be detected in the grain class with 4 phi and below. There was a slight change with distance as the range of the dataset became more compact. The triangular plots don't show much difference with distance from the volcanic source but that can be interpreted in the way that the all the grains are made in the same process in the eruption. The approximations made to do the triangular plots are considered to large to allow mapping it into the classification scheme Boggs (2006), who classifies the triangle into ten classes which are compact, compact platy, compact bladed, compact elongate, platy, bladed, elongate, very platy, very bladed and very elongated.

By looking at the frequency of circularity it can be seen that there is not much difference between various distances from the source in any of the grain size groups. The frequency of ellipse aspect ratio shows a slight difference between distances from the source.

The statistical analysis show that there is a difference between the samples with distance in all parameters between 11 km and 64 km. Even though the triangular plots don't show much difference the statistical analysis tells us that although all the samples seem to have the same trends the center of the grain shape values are at a different point in all parameters within each sample. Table 5 shows how the mean in each parameter is changing between 11 km and 64 km from the volcanic source.

Table 5: Showing how the mean in each parameter changes between 11 km and 64 km from the source of the eruption. Between these two places was always significant statistical difference.

	3.5ϕ	$<4\phi$
<i>Circularity</i>	Increase	Decrease
<i>Form factor</i>	Decrease	Increase
<i>Compactness</i>	Decrease	Decrease
<i>Fiber aspect ratio</i>	Increase	Decrease
<i>Feret aspect ratio</i>	Decrease	Increase
<i>Ellipse aspect ratio</i>	Decrease	Increase

Each grain size seems to behave in its own way, the parameters don't seem to behave in the same way in all grain sizes.

Eiriksson and Wigum (1989) look into 22 samples from various eruptions including the Medieval tephra layer they used a morphometry to define the shape of the ash particles. They found out that eruptions in sea, water or ice showed very little difference in measured shape parameters in each sample.

Mele et al. (2011) looked into changes in circularity with distance, they use a slightly different method than is done in this work but it is the most similar method found. They use a different formula for the circularity and larger grain sizes (0.5 mm or 1ϕ). In Mele et al. (2011) a complete circle is defined as 1 and the higher the number is above 1 the more irregular the grain is. In the present work however, a complete circle is 1 and the closer the circularity is to 0 the more irregular the grain is.

Mele et al. (2011) found that the circularity increases with distance. In the present work the grain sizes don't give the exactly same results. For the grain size of 3.5ϕ ($90\mu\text{m}$) it gives the same result as the Mele et al. (2011) obtained, but the opposite result is found for material $<4\phi$ ($<63\mu\text{m}$). The reason for that the two grain sizes don't show the same result might be that the grains smaller than 4ϕ ($<63\mu\text{m}$) are too small to effectively detect changes in the circularity with the particle shape analyser, at least for the comparatively small variations in sample distances (between 11 km and 64 km). A clearer result is anticipated in a study where the changes in distance are greater than observed here.

5.3 SEM

The SEM images show tephra grains that have typical forms for a phreatomagmatic eruption. The typical phreatomagmatic tephra grain is blocky with stepped surfaces, tephra grains that look like they have once been a part of a bubble wall are also quite common in this tephra layer, which may indicate that the magma had not fully degassed at the time of the eruption. Overall the grains that were looked at using the scanning electron microscope are typical for this kind of an eruption.

5.4 Volume calculations

The tephra volume was calculated with three different methods and two of them give similar volume but one four times higher. Exponential thinning and Weibull gave both volume about 0.1 km^3 which is the same volume as had been previously calculated. The power law gave 0.49 km^3 which is quite higher than the other ones. Bonadonna and Costa (2012) talk about that the Weibull method overestimates by only 14% when medial data is missing. Bonadonna and Houghton (2005) found that the tephra volume is underestimated about ~40%-70% of the cases that they looked into using the exponential thinning with various segments, the power law was rather stable data medial and distal data is missing but it can overestimate up to five times when proximal data is removed or missing. Figure 4-34 shows that the power law curve over estimates the volume further than 60 km from the source. The exponential and Weibull method don't overestimate that part. Therefore it

is indicated that the power law is an unreliable method if the data doesn't constrain the power law curve.

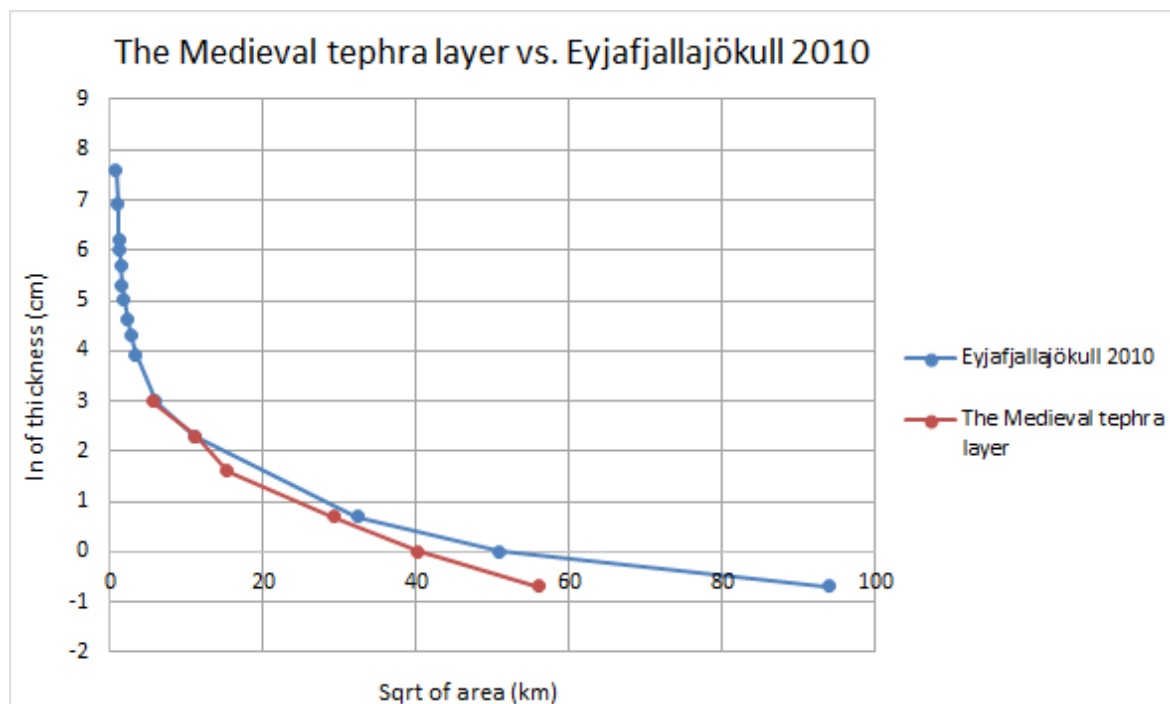


Figure 5-3: The AD 1226 eruption against the Eyjafjallajökull 2010 eruption (Gudmundsson et al., 2012) the thickness of the ash layer decreases with distance from the source. Parts of the tephra layer closest to the vent are missing in the CE 1226 eruption therefore it can be assumed that the volume calculations made by this study are underestimated (Agnes Ösp Magnúsdóttir, 2014)

The volume for this eruption is calculated by using the isopach map shown on Figure 1-5. By comparing the two eruptions shown on Figure 5-3 they have a similar trend but in the CE 1226 there is no data for the thickness near the vent and therefore it can be assumed that 0.1 km^3 is a minimum volume for the tephra layer, especially since this kind of an eruption is known to last for weeks or months, then it is safe to assume that some of the ash has blown in different directions than shown on the isopach map, possibly out to sea were the dispersal of the tephra is not known and the part near the volcanic vent is missing. So 0.1 km^3 is an absolute minimum volume for this tephra layer, the volume could easily have been two to three times larger.

6 Conclusion

- The amount of fine ash in the Medieval tephra layer is less than expected for a basaltic phreatomagmatic eruption. The fine materials missing may have washed out with time or blown away after the tephra had settled. Near the volcanic vent the distribution curves don't show a top but further away from the source the grain size distribution curves do have a clear top. The mean changes with distance as does the sorting. The total grain size was found by using the Voronio method and that gave the tephra layer a mean grain size of $189\mu\text{m}$ or 2.40 phi for the whole tephra layer as it now preserved in soils on the Reykjanes Peninsula and vicinity.
- The triangular plots don't show much difference in the shape parameters, all samples seem to show the same trend, although the grain size that shows the most difference with distance is 4 phi and below, but by using statistical analysis on all of the parameters used a statistical difference can be found between the samples as the distance from the source grows. The potential usefulness of this information in eruptions has yet to be explored in more detail.
- SEM images show that the ash from the Medieval tephra layer of CE 1226 is characterized by ash shaped as typical grains formed in a phreatomagmatic eruption. Most of the grains classify as blocky.
- The volume of the tephra layer as presently preserved were done by using three different methods. Two of them gave similar volume as had been previously calculated. The third method (power law) did not provide reliable estimates. It is assumed that the volume obtained is a minimum value because this eruption was phreatomagmatic and this type of eruption can last for some time and it is very likely that the wind direction was not the same for the whole time of the eruption.

References

- Blott, S. J., & Pye, K. (2001). GRADISTAT: a grain size distribution and statistics package for the analysis of unconsolidated sediments. *Earth surface processes and Landforms*, 26(11), 1237-1248.
- Boggs, S. (2006). *Principles of sedimentology and stratigraphy* (4 ed.). New Jersey: Person Education, Inc.
- Bonadonna, C., & Costa, A. (2012). Estimating the volume of tephra deposits: A new simple strategy. *Geology*, 40(5), 415-418. doi: 10.1130/G32769.1
- Bonadonna, C., & Houghton, B. F. (2005). Total grain-size distribution and volume of tephra-fall deposits. *Bulletin of Volcanology*, 67(5), 441-456. doi: 10.1007/s00445-004-0386-2
- Büttner, R., Dellino, P., La Volpe, L., Lorenz, V., & Zimanowski, B. (2002). Thermohydraulic explosions in phreatomagmatic eruptions as evidenced by the comparison between pyroclasts and products from Molten Fuel Coolant Interaction experiments. *Journal of Geophysical Research: Solid Earth*, 107(B11), 2277. doi: 10.1029/2001JB000511
- Büttner, R., & Zimanowski, B. (1998). Physics of thermohydraulic explosions. *Physical Review E*, 57(5), 5726-5729.
- Clifton, A. E., & Kattenhorn, S. A. (2006). Structural architecture of a highly oblique divergent plate boundary segment. *Tectonophysics*, 419(1-4), 27-40. doi: <http://dx.doi.org/10.1016/j.tecto.2006.03.016>
- Einarsson, P. (2008). Plate boundaries, rifts and transforms in Iceland. *Jökull*, 58, 35-58.
- Eiríksson, J., & Wigum, B. J. (1989). Morphometry of Selected Tephra Samples from Icelandic Volcanoes. *Jökull*, 39, 57-73.
- Fierstein, J., & Nathenson, M. (1992). Another look at the calculation of fallout tephra volumes. *Bulletin of Volcanology*, 54(2), 156-167. doi: 10.1007/BF00278005
- Francis, P., & Oppenheimer, C. (2004). *Volcanoes* (2 ed.). New York: Oxford University Press.

- Guðmundsson, M. T., Thordarson, T., Höskuldsson, Á., Larsen, G., Björnsson, H., Prata, F. J., Oddsson, B., Magnússon, E., Högnadóttir, T., Petersen, G. N., Hayward, C. L., Stevenson, J. A., & Jónsdóttir, I. (2012). Ash generation and distribution from the April-May 2010 eruption of Eyjafjallajökull, Iceland. *Sci. Rep.*, 2.
- Guðmundsson, A. (1986). Mechanical aspects of postglacial volcanism and tectonics of the Reykjanes Peninsula, southwest Iceland. *Journal of Geophysical Research*, 91(B12), 12711-12721. doi: 10.1029/JB091iB12p12711
- Haflidason, H., Eiriksson, J., & Kreveld, S. V. (2000). The tephrochronology of Iceland and the North Atlantic region during the Middle and Late Quaternary: a review. *Journal of Quaternary Science*, 15(1), 3-22.
- Hagstofa Íslands (2014). Mannfjöldi eftir kyni, aldri og sveitarfélögum 1998-2014 - Sveitarfélagaskipan hvers árs. Retrieved 18.06.2014 from <http://hagstofa.is/?PageID=2593&src=https://rannsokn.hagstofa.is/pxis/Dialog/varval.asp?ma=MAN10001%26ti=Mannfj%F6ldi+eftir+sveitarf%E9l%F6gum%2C+kyni%2C+r%EDkisfangi+og+%E1rsfj%F3r%F0ungum+2010%2D2014%26path=../Database/mannfjoldi/Arsfjordungstolur/%26lang=3%26units=Fj%F6ldi>
- Harðarsson, B., Fitton, G. J., & Hjartarson, Á. (2008). Tertiary volcanism in Iceland. *Jökull*, 58, 161-178.
- HITACHI TM3000 Tabletop Scanning Electron Microscope. (2014). Retrieved 20.10, 2014 from <http://www.microscopy.ou.edu/hitachi-3000.shtml>
- Horwell, C. J. (2007). Grain-size analysis of volcanic ash for the rapid assessment of respiratory health hazard. *Journal of Environmental Monitoring*, 9(10), 1107-1115.
- Houghton, B. F., Wilson, C. J. N., & Pyle, D. M. (2000). Pyroclastic fall deposits. In H. Sigurðsson, B. F. Houghton, S. R. McNutt, H. Rymer & J. Stix (Eds.), *Encyclopedia of Volcanoes* (pp. 555-570). San Diego: Academic press.
- Houghton, B. F., Wilson, C. J. N., Smith, R. T., & Gilbert, J. S. (2000). Phreatoplinian eruptions. In H. Sigurðsson, B. F. Houghton, S. R. McNutt & J. Stix (Eds.), *Encyclopedia of volcanos* (pp. 513-527). San Diego: Academic press.
- Hreinsdóttir, S., Einarsson, P., & Sigmundsson, F. (2001). Crustal deformation at the oblique spreading Reykjanes Peninsula, SW Iceland: GPS measurements from 1993 to 1998. *Journal of Geophysical Research: Solid Earth (1978–2012)*, 106(B7), 13803-13816.
- Höskuldsson, Á., Hey, R., Kjartansson, E., & Guðmundsson, G. B. (2007). The Reykjanes Ridge between 63°10'N and Iceland. *Journal of Geodynamics*, 43(1), 73-86. doi: <http://dx.doi.org/10.1016/j.jog.2006.09.003>

- Jakobsson, S. P., Jónsson, J., & Shido, F. (1978). Petrology of the Western Reykjanes Peninsula, Iceland. *Journal of Petrology*, 19(4), 669-705. doi: 10.1093/petrology/19.4.669
- Levene, H. (1960). Robust tests for equality of variances1. *Contributions to probability and statistics: Essays in honor of Harold Hotelling*, 2, 278-292.
- Marti, J., Soriano, C., & Dingwell, D. B. (1999). Tube pumices as strain markers of the ductile-brittle transition during magma fragmentation. *Nature*, 402(6762), 650-653. doi: 10.1038/45219
- Mason, C. (2011). NMBAQC's Best Practice Guidance - Particle Size Analysis (PSA) for Supporting Biological Analysis.
- Mele, D., Dellino, P., Sulpizio, R., & Braia, G. (2011). A systematic investigation on the aerodynamics of ash particles. *Journal of Volcanology and Geothermal Research*, 203(1–2), 1-11. doi: <http://dx.doi.org/10.1016/j.jvolgeores.2011.04.004>
- Micromeritics. (1996-2014). Sedigraph III Plus. Retrieved 19.09.2014 from <http://www.micromeritics.com/Product-Showcase/SediGraph-III-Plus.aspx>
- Micromeritics. (2010). *SediGraph III 5120 Operator's Manual (V1.04)*. Norcross, GA.
- Morrissey, M., Zimanowski, B., Wohletz, K. H., & Büttner, R. (2000). Phreatomagmatic fragmentation. In H. Sigurðsson, B. F. Houghton, S. R. McNutt, H. Rymer & J. Stix (Eds.), *Encyclopedia of volcanoes* (pp. 431-445). San Diego: Academic press.
- Ólafsson, G. (1983). Greinargerð um Miðaldarlagið (pp. 25 pages.). Verkfræði og náttúruvísindadeild: Háskóli Íslands.
- Particle Insight. User manual. Micromeritics.
- Proussevitch, A. A., & Sahagian, D. L. (1998). Dynamics and energetics of bubble growth in magmas: Analytical formulation and numerical modeling. *Journal of Geophysical Research: Solid Earth*, 103(B8), 18223-18251. doi: 10.1029/98JB00906
- Pyle, D. M. (1989). The thickness, volume and grainsize of tephra fall deposits. *Bulletin of Volcanology*, 51(1), 1-15. doi: 10.1007/BF01086757
- Pyle, D. M. (1990). New estimates for the volume of the Minoan eruption. . In H. DA (Ed.), *Thera and the Aegean World, III*. (pp. 113-121). London: Thera Foundation.
- Sahagian, D. (1999). Volcanology: Magma fragmentation in eruptions. *Nature*, 402(6762), 589-591. doi: 10.1038/45099
- Sahagian, D. L., & Proussevitch, A. A. (1996). Thermal effects of magma degassing. *Journal of Volcanology and Geothermal Research*, 74(1–2), 19-38. doi: [http://dx.doi.org/10.1016/S0377-0273\(96\)00047-9](http://dx.doi.org/10.1016/S0377-0273(96)00047-9)

- Sartorius. (1999). Manual of Weighing Applications, Part 1, Density (pp. 16-17): Sartoris.
- Schmith, J. (2014). (Personal communication from september 2013 to august 2014)
- Self, S., & Sparks, R. S. J. (1978). Characteristics of widespread pyroclastic deposits formed by the interaction of silicic magma and water. *Bulletin Volcanology*, 41(3), 196-212. doi: 10.1007/BF02597223
- Sigurgeirsson, M. Á. (1992). *Gjóskumyndanir á Reykjanesi*. Reykjavík.
- Sigurgeirsson, M. Á. (1995a). Miðaldarlagið. In B. Hróarsson, D. Jónsson & S. S. Jónsson (Eds.), *Eyjar í eldhafi*. Reykjavík: Gott mál.
- Sigurgeirsson, M. Á. (1995b). Yngra-Stampagosið á Reykjanesi. *Náttúrufræðingurinn*, 64(3), 211-230.
- Sæmundsson, K. (1986). Subaerial volcanism in the western North Atlantic. *The Geology of North America, 1000*, 69-86.
- Sæmundsson, K., & Sigurgeirsson, M. Á. (2013). Reykjanesskagi. In J. Sólnes, F. Sigmundsson & B. Bessason (Eds.), *Náttúruvá á Íslandi eldgos og jarðskjálftar* (pp. 379-401).
- Thorarinsson, S. (1944). Tefrokronologiska studier på Island. *Geografiska Annaler*, 26, 1-217.
- Thorarinsson, S., Einarsson, T., Sigvaldason, G., & Elisson, G. (1964). The submarine eruption off the Vestmann islands 1963–64. *Bulletin Volcanologique*, 27(1), 435-445. doi: 10.1007/BF02597544
- Thordarson, T., & Höskuldsson, Á. (2008). Postglacial volcanism in Iceland. *Jökull*, 58, 197-228.
- Toramaru, A. (1995). Numerical study of nucleation and growth of bubbles in viscous magmas. *Journal of Geophysical Research: Solid Earth*, 100(B2), 1913-1931. doi: 10.1029/94JB02775
- Vespermann, D., & Schmincke, H.-U. (2000). Scoria cones and tuff rings. In H. Sigurdsson, B. F. Houghton, S. R. McNutt & J. Stix (Eds.), *Encyclopedia of Volcanoes* (pp. 683-694). San Diego: Academic press.
- Walker, G. L. (1973). Explosive volcanic eruptions — a new classification scheme. *Geologische Rundschau*, 62(2), 431-446. doi: 10.1007/BF01840108
- Walker, G. P. L. (1980). The Taupo pumice: Product of the most powerful known (ultraplinian) eruption? *Journal of Volcanology and Geothermal Research*, 8(1), 69-94. doi: [http://dx.doi.org/10.1016/0377-0273\(80\)90008-6](http://dx.doi.org/10.1016/0377-0273(80)90008-6)

- Walker, G. P. L., & Croasdale, R. (1971). Characteristics of some basaltic pyroclastics. *Bulletin Volcanologique*, 35(2), 303-317. doi: 10.1007/BF02596957
- Walpole, R. E., Myers, R. H., Myers, S. L., & Ye, K. (2012). *Probability & Statistics for Engineers & Scientists* (9 ed.): Pearson.
- Wilson, C. J. N., & Houghton, B. F. (2000). Pyroclast transport and deposition. In H. Sigurðsson, B. F. Houghton, S. R. McNutt, H. Rymer & J. Stix (Eds.), *Encyclopedia of Volcanoes* (pp. 545-554). San Diego: Academic press.
- Wohletz, K., McQueen, R., & Morrissey, M. (1995). Experimental study of hydrovolcanism by fuel-coolant interaction analogs. *this volume*.
- Wohletz, K. H. (1983). Mechanisms of hydrovolcanic pyroclast formation: Grain-size, scanning electron microscopy, and experimental studies. *Journal of Volcanology and Geothermal Research*, 17(1-4), 31-63. doi: [http://dx.doi.org/10.1016/0377-0273\(83\)90061-6](http://dx.doi.org/10.1016/0377-0273(83)90061-6)
- Wohletz, K. H. (1986). Explosive magma-water interactions: Thermodynamics, explosion mechanisms, and field studies. *Bulletin of Volcanology*, 48(5), 245-264.
- Zhang, Y. (1999). A criterion for the fragmentation of bubbly magma based on brittle failure theory. *Nature*, 402(6762), 648-650. doi: 10.1038/45210
- Zimanowski, B., Büttner, R., Lorenz, V., & Häfele, H.-G. (1997). Fragmentation of basaltic melt in the course of explosive volcanism. *Journal of Geophysical Research: Solid Earth*, 102(B1), 803-814. doi: 10.1029/96JB02935
- Zimanowski, B., & Wohletz, K. (2000). *Physics of Phreatomagmatism-I*. Paper presented at the International Maar Conference, Daun, Germany.
- Þórarinnsson, S. (1965). Neðansjávargos við Ísland. *Náttúrufræðingurinn*, 35, 49-74.
- Þórðarsson, Þ. (1990). *Skaftáreldar 1783-1785*. Reykjavík: University of Iceland.

Appendix I

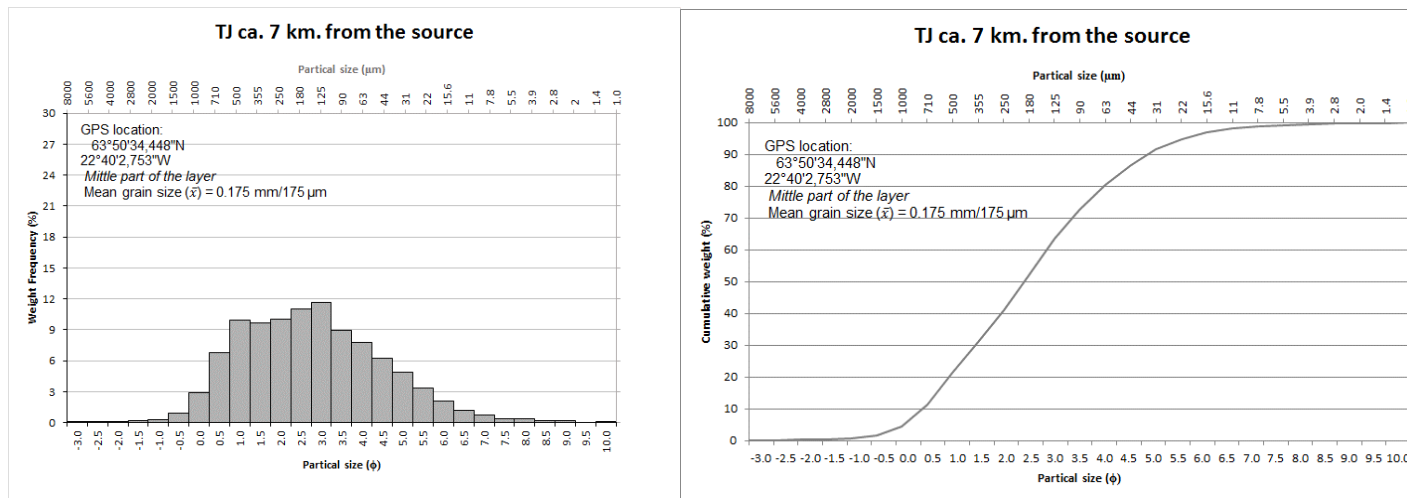
Sample information

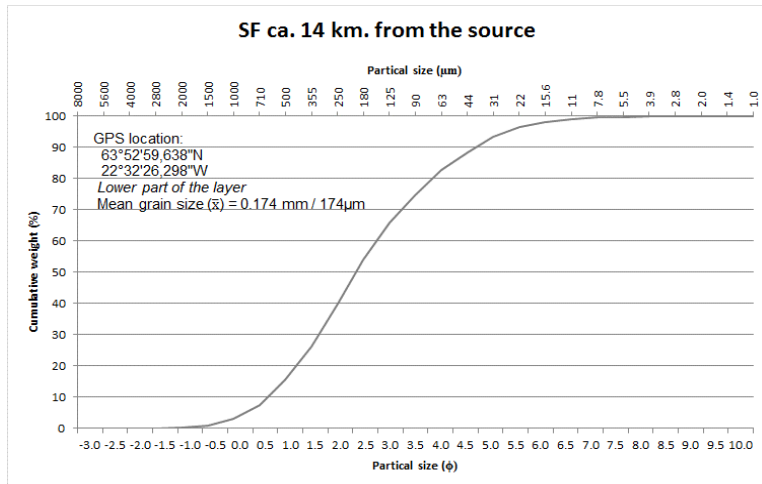
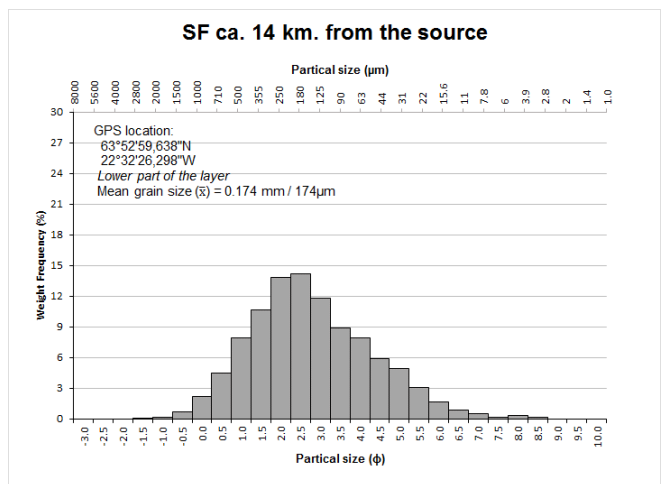
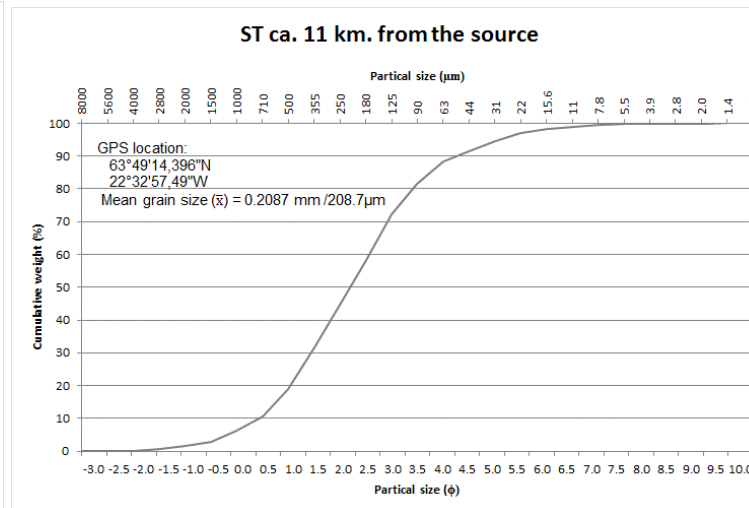
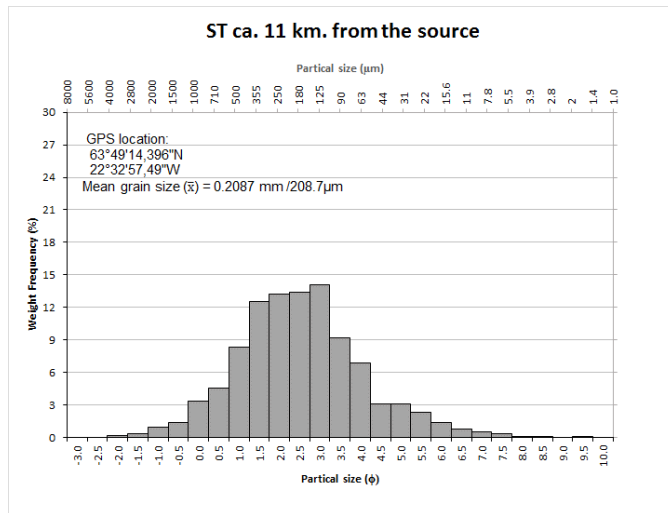
Sample name	Distance from source	GPS-location (Degrees, minutes, seconds)	Sample place	Which part of the layer	Condition of the layer
TJ	6.5 km	63°50'34,448"N 22°40'2,753"W	Tjaldastaðargjá	Upper part of the layer	Good
ST	10.6 km	63°49'14,396"N 22°32'57,49"W	Staðarmalir north of Grindavík	Bulk sample	Good
SF	14.1 km	63°52'59,638"N 22°32'26,298"W	Swamp north of Lágafells top crater	Lower part of the layer	Good
LF	16.1 km	63°51'32,69"N 22°27'34,661"W	Lágafell, north of Grindavík	Bulk sample	Good
FF	20.9 km	63°51'30,137"N 22°21'16,526"W	Abut 1km. north of Festarfjall	Bulk sample	Good
SK	25.6 km	63°51'26,714"N 22°15'24,523"W	Soil section east of Skálamælifell	Bulk sample	Little bit soil mixed
MH	25.5 km	64°1'16,045"N 22°37'8,027"W	Miðnesheiði, off the road to Sandgerði	Bulk sample	Quite reworked
EB	33.2 km	63°51'52,388"N 22°6'2,648"W	Soil section in SW mountain side of Einbúa, west of Krýsuvík	Bulk sample	Little bit soil mixed
VL	34.5 km	64°1'18,216"N 22°16'3,965"W	Westpart of Keilisnes on Vatnsleysuströnd	Bulk sample	Good
VS	44.2 km	63°57'39,598"N 21°56'18,354"W	Breiðdalur east of Vatnsskarð	Bulk sample	Good
BL	47.6 km	63°59'28,525"N 21°53'33,304"W	Bláfjallavegur, off the road to Bláfjöll	Bulk sample	Good
VI	64.0 km	64°2'22,076"N 21°34'24,817"W	Vífilsfell, near Vífilsfell	Bulk sample	Good

The the volcanic source is estimated at 0.5 km of the shore. GPS location: 63°48'0,199"N; 22°45'28,672"W

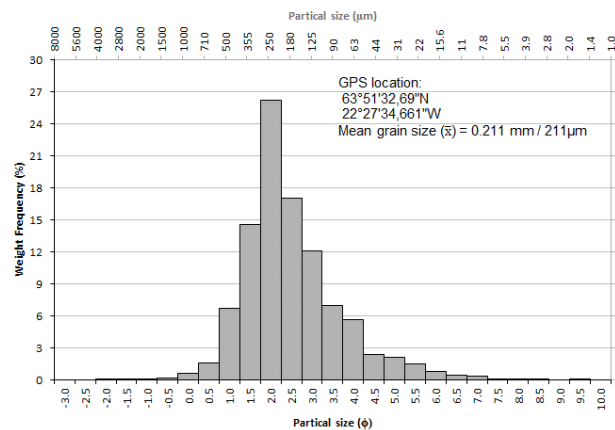
Appendix II

Histograms, cumulative curves and grain size data

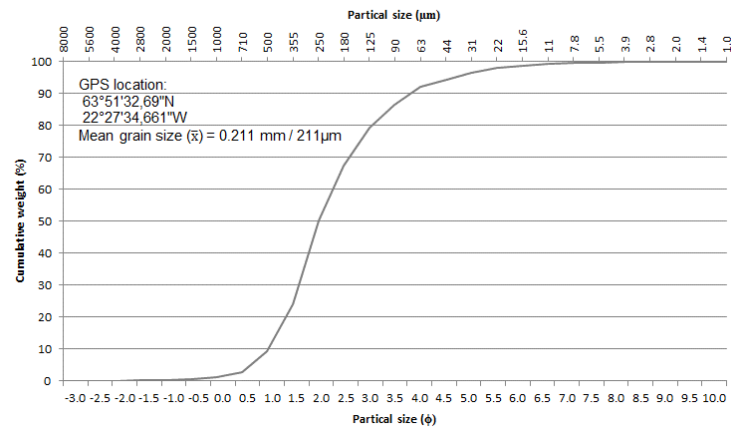




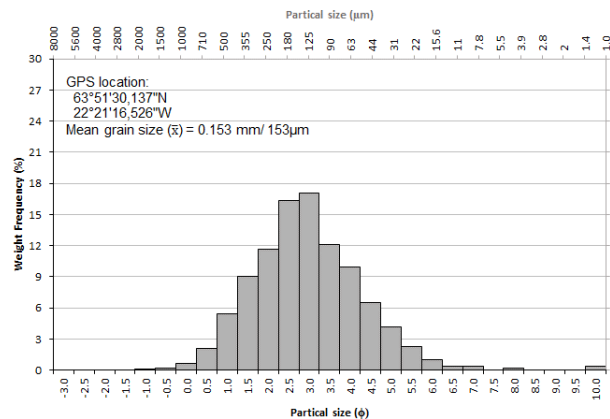
LF ca. 16 km. from the source



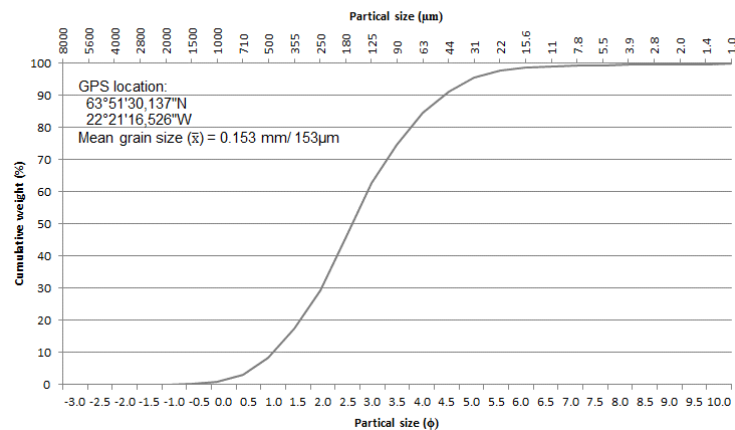
LF ca. 16 km. from the source



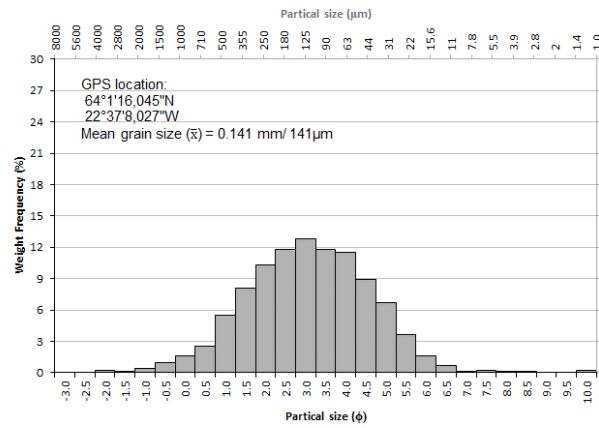
FF ca. 21 km. from the source



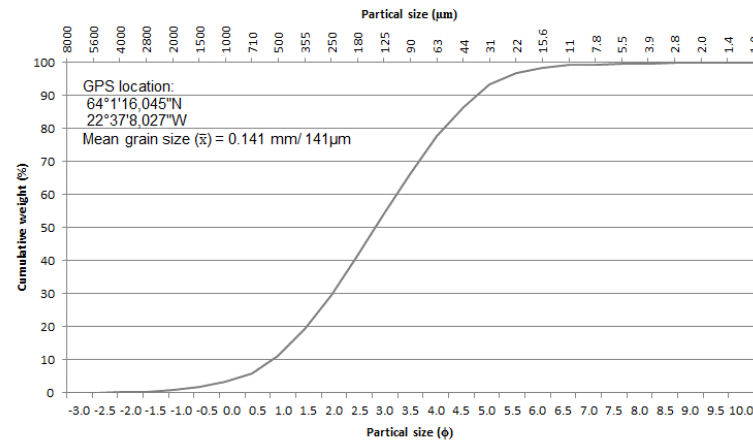
FF ca. 21 km. from the source



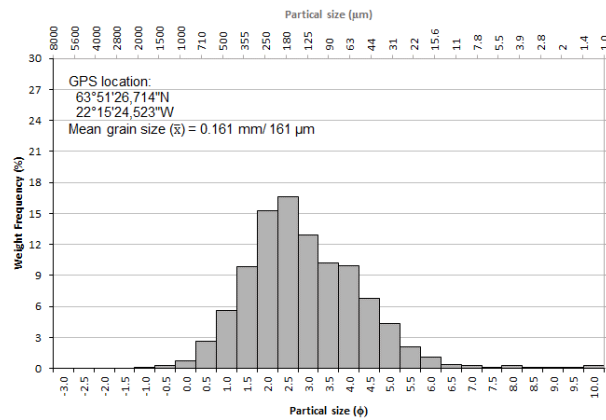
MH ca. 26 km. from the source



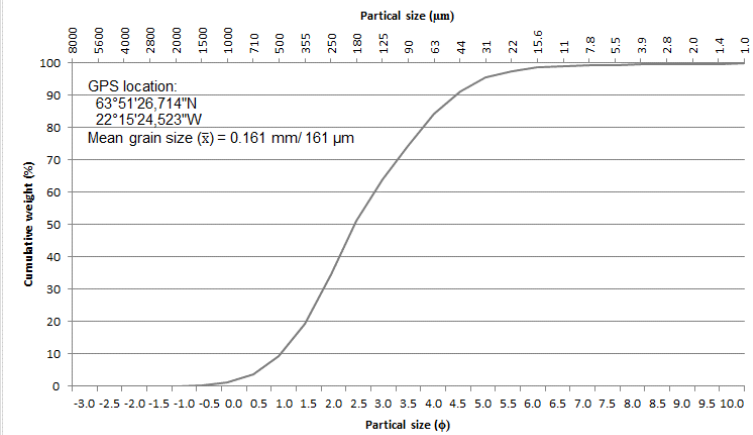
MH ca. 26 km. from the source



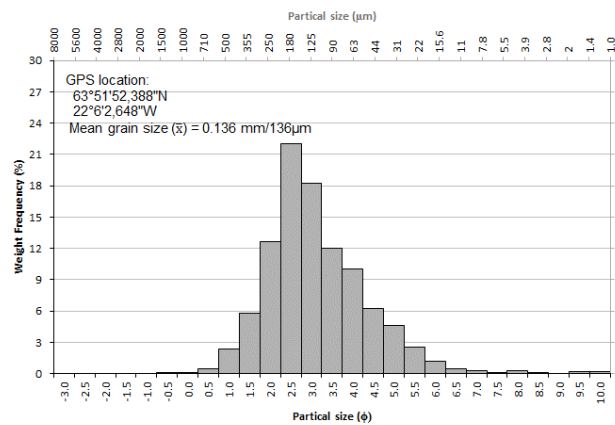
SK ca. 26 km. from the source



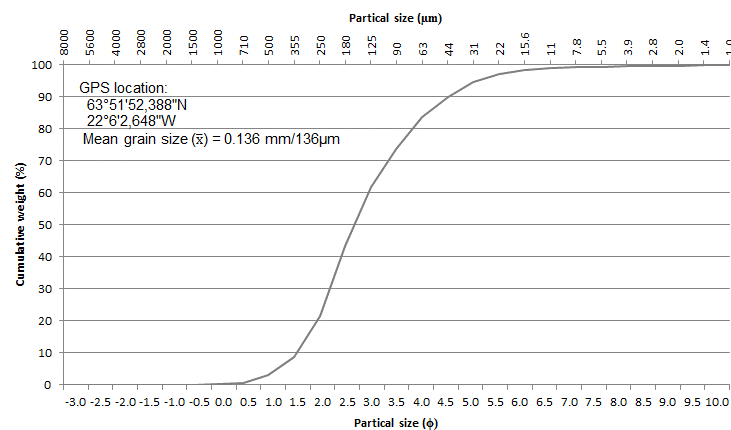
SK ca. 26 km. from the source



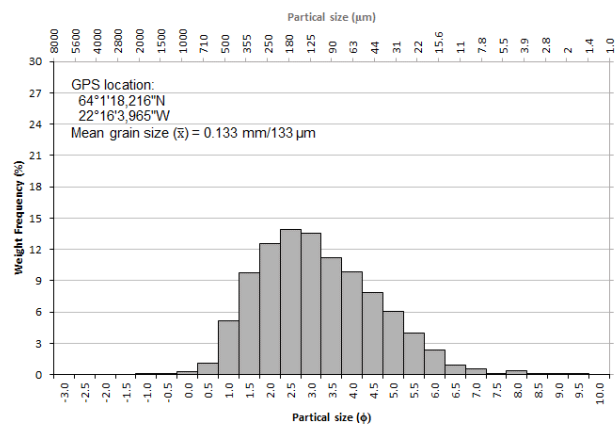
EB ca. 33 km. from the source



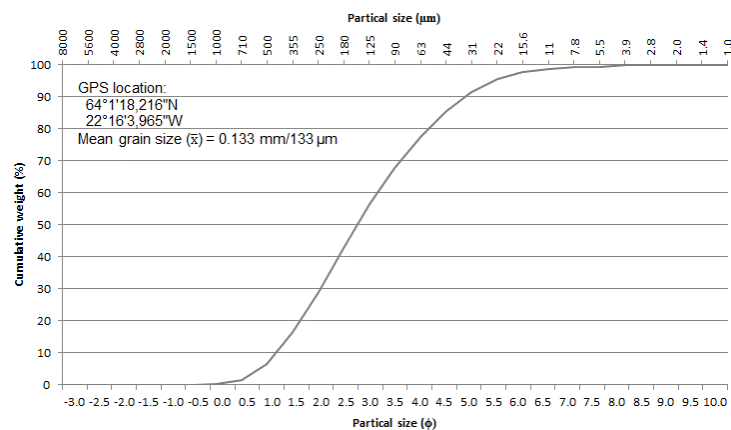
EB ca. 33 km. from the source



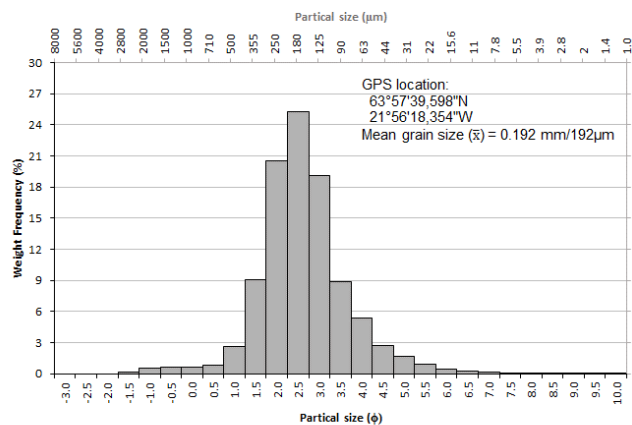
VL ca. 35 km. from the source



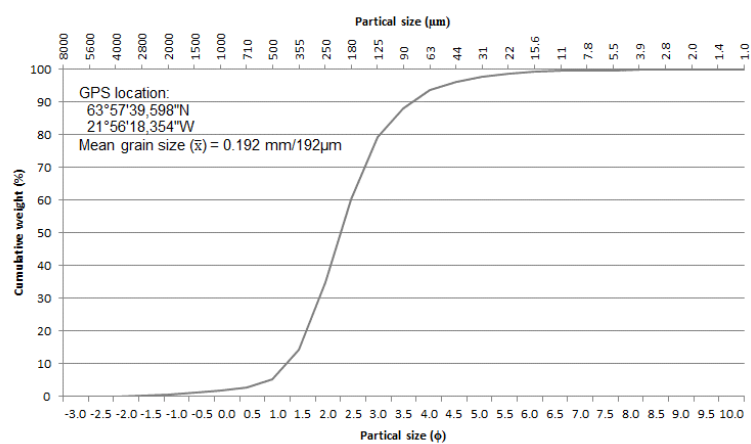
VL ca. 35 km. from the source



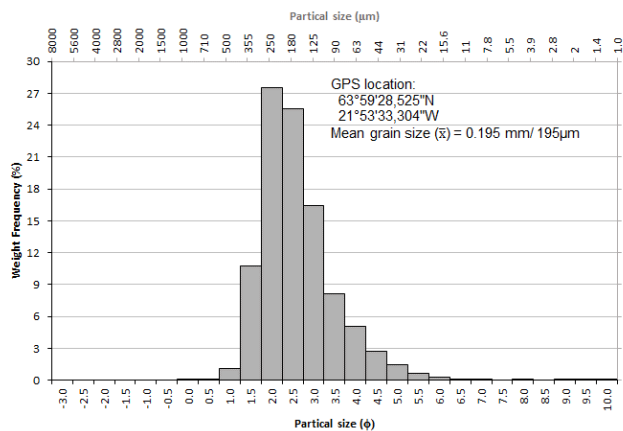
VS ca. 44 km. from the source



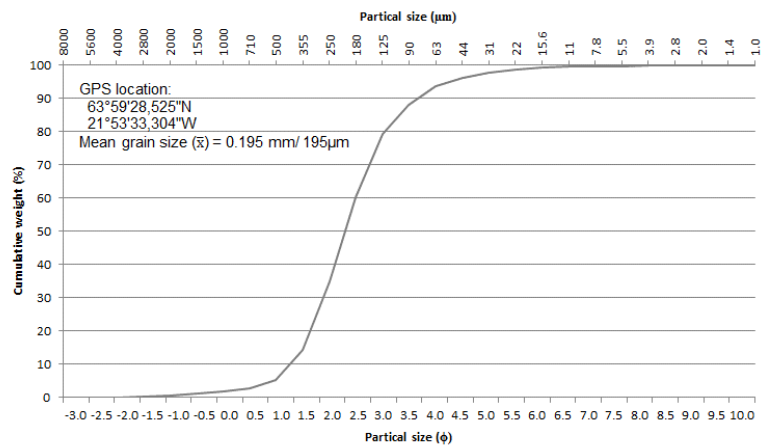
VS ca. 44 km. from the source

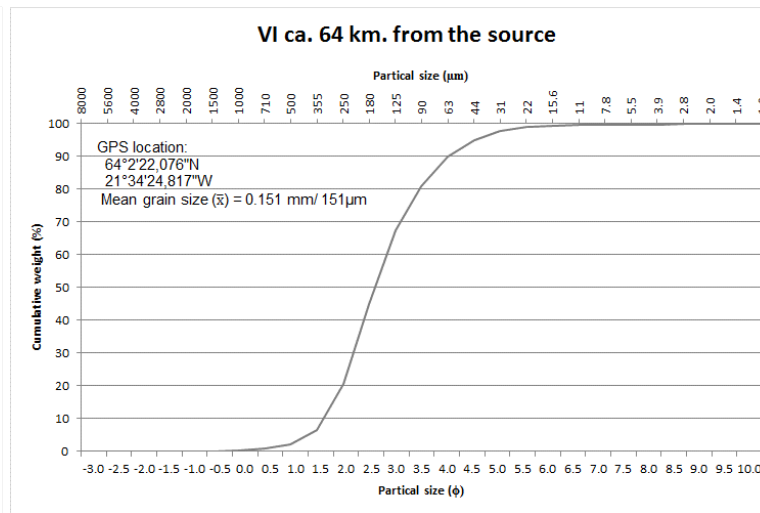
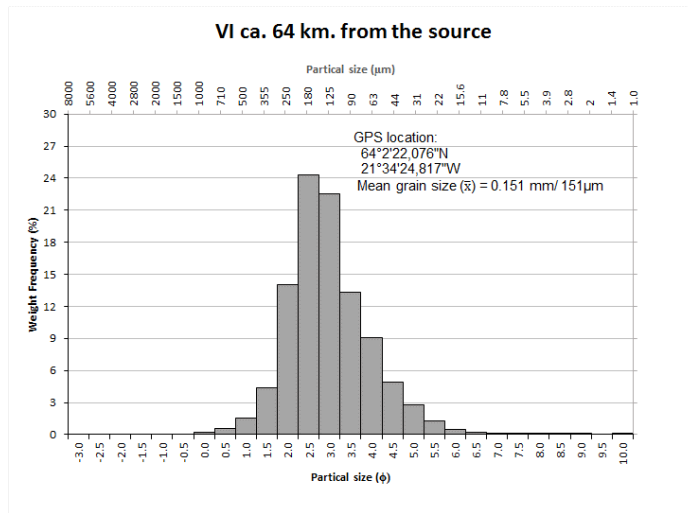


BL ca. 48 km. from the source



BL ca. 48 km. from the source





TJ-6.5 km from the source

GPS: 63°50'34.448"N
22°40'2.753"W

Size (mm)	Size (phi)	Weight (g)	Weight (%)	Cumulative (%)
16	-4.0	0.0	0.00	0.00
11.2	-3.5	0.0	0.00	0.00
8	-3.0	0.07	0.04	0.04
5.6	-2.5	0.21	0.12	0.16
4	-2.0	0.21	0.12	0.28
2.8	-1.5	0.3	0.17	0.45
2	-1.0	0.57	0.32	0.77
1.5	-0.5	1.64	0.93	1.69
1	0.0	5.12	2.89	4.58
0.710	0.5	11.97	6.75	11.33
0.500	1.0	17.66	9.96	21.30
0.355	1.5	17.08	9.64	30.93
0.250	2.0	17.84	10.06	41.00
0.180	2.5	19.53	11.02	52.01
0.125	3.0	20.61	11.63	63.64
0.090	3.5	15.8	8.91	72.55
0.063	4.0	13.81	7.79	80.35
0.044	4.5	11.1	6.25	86.60
0.031	5.0	8.7	4.91	91.51
0.022	5.5	5.9	3.32	94.84
0.0156	6.0	3.7	2.07	96.90
0.0110	6.5	2.1	1.20	98.10
0.0078	7.0	1.3	0.73	98.83
0.0055	7.5	0.7	0.42	99.25
0.0039	8.0	0.6	0.34	99.58
0.0028	8.5	0.3	0.17	99.75
0.0020	9.0	0.3	0.17	99.92
0.0014	9.5	0.0	0.00	99.92
0.0010	10.0	0.1	0.08	100.00

ST-10.6 km from the source

GPS: 63°49'14,396"N
22°32'57,49"W

Size (mm)	Size (phi)	Weight (g)	Weight (%)	Cumulative (%)
16	-4.0	0.0	0.00	0.00
11.2	-3.5	0.0	0.00	0.00
8	-3.0	0.0	0.00	0.00
5.6	-2.5	0.0	0.00	0.00
4	-2.0	0.23	0.17	0.17
2.8	-1.5	0.47	0.35	0.52
2	-1.0	1.29	0.96	1.48
1.5	-0.5	1.84	1.37	2.84
1	0.0	4.50	3.34	6.18
0.710	0.5	6.08	4.51	10.69
0.500	1.0	11.21	8.32	19.01
0.355	1.5	16.85	12.50	31.52
0.250	2.0	17.85	13.25	44.76
0.180	2.5	18.06	13.40	58.16
0.125	3.0	19.03	14.12	72.28
0.090	3.5	12.41	9.21	81.49
0.063	4.0	9.30	6.90	88.39
0.044	4.5	4.21	3.12	91.52
0.031	5.0	4.16	3.09	94.61
0.022	5.5	3.13	2.32	96.93
0.0156	6.0	1.79	1.33	98.26
0.0110	6.5	0.97	0.72	98.98
0.0078	7.0	0.65	0.48	99.46
0.0055	7.5	0.45	0.34	99.79
0.0039	8.0	0.11	0.08	99.87
0.0028	8.5	0.02	0.02	99.89
0.0020	9.0	0.00	0.00	99.89
0.0014	9.5	0.15	0.11	100.00
0.0010	10.0	0.00	0.00	100.00

SF-14.1 km. from the source

GPS: 63°52'59,638"N
22°32'26,298"W

Size (mm)	Size(phi)	Weight (g)	Weight (%)	Cumulative (%)
16	-4.0	0.0	0.00	0.00
11.2	-3.5	0.0	0.00	0.00
8	-3.0	0.0	0.00	0.00
5.6	-2.5	0.0	0.00	0.00
4	-2.0	0	0.00	0.00
2.8	-1.5	0.1	0.09	0.09
2	-1.0	0.14	0.12	0.21
1.5	-0.5	0.8	0.71	0.92
1	0.0	2.45	2.17	3.09
0.710	0.5	5.06	4.47	7.56
0.500	1.0	8.91	7.88	15.44
0.355	1.5	12.06	10.66	26.10
0.250	2.0	15.59	13.78	39.88
0.180	2.5	16.07	14.21	54.09
0.125	3.0	13.36	11.81	65.90
0.090	3.5	10	8.84	74.74
0.063	4.0	8.9	7.87	82.61
0.044	4.5	6.66	5.89	88.50
0.031	5.0	5.52	4.88	93.38
0.022	5.5	3.46	3.06	96.44
0.0156	6.0	1.86	1.64	98.08
0.0110	6.5	0.98	0.87	98.95
0.0078	7.0	0.57	0.50	99.45
0.0055	7.5	0.18	0.16	99.61
0.0039	8.0	0.31	0.27	99.89
0.0028	8.5	0.13	0.11	100.00
0.0020	9.0	0.00	0.00	100.00
0.0014	9.5	0.00	0.00	100.00
0.0010	10.0	0.00	0.00	100.00

LF-16.1 from the source

GPS: 63°51'32,69"N
22°27'34,661"W

Size (mm)	Size (phi)	Weight (g)	Weight (%)	Cumulative (%)
16	-4.0	0.0	0.00	0.00
11.2	-3.5	0.0	0.00	0.00
8	-3.0	0.0	0.00	0.00
5.6	-2.5	0.0	0.00	0.00
4	-2.0	0.11	0.06	0.06
2.8	-1.5	0.15	0.08	0.13
2	-1.0	0.14	0.07	0.21
1.5	-0.5	0.45	0.23	0.44
1	0.0	1.21	0.62	1.06
0.710	0.5	3.12	1.60	2.66
0.500	1.0	13.11	6.74	9.40
0.355	1.5	28.38	14.59	23.99
0.250	2.0	51.10	26.27	50.26
0.180	2.5	33.13	17.03	67.29
0.125	3.0	23.63	12.15	79.44
0.090	3.5	13.57	6.98	86.41
0.063	4.0	10.96	5.63	92.05
0.044	4.5	4.59	2.36	94.41
0.031	5.0	4.13	2.12	96.53
0.022	5.5	2.87	1.48	98.01
0.0156	6.0	1.50	0.77	98.78
0.0110	6.5	0.96	0.49	99.27
0.0078	7.0	0.66	0.34	99.61
0.0055	7.5	0.29	0.15	99.76
0.0039	8.0	0.07	0.04	99.80
0.0028	8.5	0.17	0.09	99.89
0.0020	9.0	0.00	0.00	99.89
0.0014	9.5	0.22	0.11	100.00
0.0010	10.0	0.00	0.00	100.00

FF-20.9 from the source

GPS: 63°51'30,137"N
22°21'16,526"W

Size (mm)	Size (phi)	Weight (g)	Weight (%)	Cumulative (%)
16	-4.0	0.0	0.00	0.00
11.2	-3.5	0.0	0.00	0.00
8	-3.0	0.0	0.00	0.00
5.6	-2.5	0.0	0.00	0.00
4	-2.0	0.0	0.00	0.00
2.8	-1.5	0	0.00	0.00
2	-1.0	0.1	0.09	0.09
1.5	-0.5	0.23	0.20	0.29
1	0.0	0.72	0.64	0.93
0.710	0.5	2.31	2.05	2.99
0.500	1.0	6.15	5.47	8.45
0.355	1.5	10.21	9.08	17.53
0.250	2.0	13.08	11.63	29.16
0.180	2.5	18.39	16.35	45.51
0.125	3.0	19.22	17.09	62.60
0.090	3.5	13.6	12.09	74.69
0.063	4.0	11.21	9.97	84.66
0.044	4.5	7.37	6.56	91.21
0.031	5.0	4.73	4.20	95.42
0.022	5.5	2.51	2.23	97.65
0.0156	6.0	1.18	1.05	98.69
0.0110	6.5	0.43	0.38	99.07
0.0078	7.0	0.40	0.36	99.43
0.0055	7.5	0.00	0.00	99.43
0.0039	8.0	0.24	0.21	99.64
0.0028	8.5	0.00	0.00	99.64
0.0020	9.0	0.00	0.00	99.64
0.0014	9.5	0.00	0.00	99.64
0.0010	10.0	0.40	0.36	100.00

SK-25.6. from the source

GPS: 63°51'26,714"N
22°15'24,523"

Size (mm)	Size (phi)	Weight (g)	Weight (%)	Cumulative (%)
16	-4.0	0.0	0.00	0.00
11.2	-3.5	0.0	0.00	0.00
8	-3.0	0.0	0.00	0.00
5.6	-2.5	0.0	0.00	0.00
4	-2.0	0.0	0.00	0.00
2.8	-1.5	0	0.00	0.00
2	-1.0	0.04	0.10	0.10
1.5	-0.5	0.12	0.29	0.39
1	0.0	0.31	0.76	1.15
0.710	0.5	1.09	2.67	3.81
0.500	1.0	2.29	5.60	9.41
0.355	1.5	4.03	9.85	19.27
0.250	2.0	6.26	15.31	34.57
0.180	2.5	6.79	16.60	51.17
0.125	3.0	5.28	12.91	64.08
0.090	3.5	4.17	10.20	74.28
0.063	4.0	4.07	9.95	84.23
0.044	4.5	2.8	6.81	91.04
0.031	5.0	1.8	4.38	95.43
0.022	5.5	0.8	2.07	97.50
0.0156	6.0	0.4	1.08	98.59
0.0110	6.5	0.2	0.38	98.96
0.0078	7.0	0.1	0.28	99.25
0.0055	7.5	0.0	0.02	99.27
0.0039	8.0	0.1	0.28	99.55
0.0028	8.5	0.0	0.05	99.60
0.0020	9.0	0.0	0.09	99.69
0.0014	9.5	0.0	0.05	99.74
0.0010	10.0	0.1	0.26	100.00

MH-25.5 km from the source

GPS: 64°1'16,045"N
22°37'8,027"W

Size (mm)	Size (phi)	Weight (g)	Weight (%)	Cumulative (%)
16	-4.0	0.0	0.00	0.00
11.2	-3.5	0.0	0.00	0.00
8	-3.0	0.0	0.00	0.00
5.6	-2.5	0.0	0.00	0.00
4	-2.0	0.13	0.21	0.21
2.8	-1.5	0.08	0.13	0.34
2	-1.0	0.25	0.40	0.74
1.5	-0.5	0.59	0.95	1.69
1	0.0	1.01	1.62	3.31
0.710	0.5	1.59	2.55	5.86
0.500	1.0	3.4	5.46	11.32
0.355	1.5	5.04	8.10	19.42
0.250	2.0	6.42	10.31	29.73
0.180	2.5	7.34	11.79	41.52
0.125	3.0	8	12.85	54.37
0.090	3.5	7.32	11.76	66.13
0.063	4.0	7.19	11.55	77.67
0.044	4.5	5.56	8.92	86.60
0.031	5.0	4.17	6.70	93.30
0.022	5.5	2.25	3.62	96.91
0.0156	6.0	0.99	1.59	98.51
0.0110	6.5	0.43	0.70	99.20
0.0078	7.0	0.10	0.17	99.37
0.0055	7.5	0.12	0.20	99.57
0.0039	8.0	0.10	0.17	99.73
0.0028	8.5	0.02	0.03	99.77
0.0020	9.0	0.00	0.00	99.77
0.0014	9.5	0.00	0.00	99.77
0.0010	10.0	0.14	0.23	100.00

EB-33.2 km. from the source

GPS: 63°51'52,388"N
22°6'2,648"W

Size (mm)	Size (phi)	Weight (g)	Weight (%)	Cumulative (%)
16	-4.0	0.0	0.00	0.00
11.2	-3.5	0.0	0.00	0.00
8	-3.0	0.0	0.00	0.00
5.6	-2.5	0.0	0.00	0.00
4	-2.0	0.0	0.00	0.00
2.8	-1.5	0.0	0.00	0.00
2	-1.0	0.0	0.00	0.00
1.5	-0.5	0.01	0.03	0.03
1	0.0	0.05	0.14	0.17
0.710	0.5	0.17	0.48	0.65
0.500	1.0	0.83	2.34	2.98
0.355	1.5	2.06	5.80	8.78
0.250	2.0	4.5	12.67	21.45
0.180	2.5	7.83	22.04	43.48
0.125	3.0	6.47	18.21	61.69
0.090	3.5	4.27	12.02	73.71
0.063	4.0	3.58	10.08	83.79
0.044	4.5	2.22	6.25	90.04
0.031	5.0	1.63	4.59	94.63
0.022	5.5	0.92	2.58	97.22
0.0156	6.0	0.43	1.21	98.43
0.0110	6.5	0.17	0.49	98.92
0.0078	7.0	0.09	0.27	99.18
0.0055	7.5	0.05	0.13	99.32
0.0039	8.0	0.10	0.29	99.60
0.0028	8.5	0.02	0.07	99.67
0.0020	9.0	0.00	0.00	99.67
0.0014	9.5	0.06	0.18	99.85
0.0010	10.0	0.05	0.15	100.00

VL-34.5 km. from the source

GPS: 64°1'18,216"N
22°16'3,965"W

Size (mm)	Size (phi)	Weight (g)	Weight (%)	Cumulative (%)
16	-4.0	0.0	0.00	0.00
11.2	-3.5	0.0	0.00	0.00
8	-3.0	0.0	0.00	0.00
5.6	-2.5	0.0	0.00	0.00
4	-2.0	0.0	0.00	0.00
2.8	-1.5	0	0.00	0.00
2	-1.0	0.01	0.02	0.02
1.5	-0.5	0.04	0.08	0.10
1	0.0	0.13	0.26	0.36
0.710	0.5	0.56	1.11	1.47
0.500	1.0	2.59	5.14	6.60
0.355	1.5	4.94	9.80	16.40
0.250	2.0	6.31	12.51	28.92
0.180	2.5	7.02	13.92	42.84
0.125	3.0	6.85	13.59	56.43
0.090	3.5	5.66	11.23	67.65
0.063	4.0	4.96	9.84	77.49
0.044	4.5	3.99	7.91	85.40
0.031	5.0	3.05	6.06	91.45
0.022	5.5	1.99	3.95	95.41
0.0156	6.0	1.21	2.39	97.80
0.0110	6.5	0.48	0.96	98.76
0.0078	7.0	0.29	0.57	99.33
0.0055	7.5	0.05	0.10	99.43
0.0039	8.0	0.19	0.38	99.81
0.0028	8.5	0.02	0.03	99.84
0.0020	9.0	0.06	0.13	99.97
0.0014	9.5	0.02	0.03	100.00
0.0010	10.0	0.00	0.00	100.00

VS-44.2 km. from the source

GPS: 63°57'39,598"N
21°56'18,354"W

Size (mm)	Size (phi)	Weight (g)	Weight (%)	Cumulative (%)
16	-4.0	0.0	0.00	0.00
11.2	-3.5	0.0	0.00	0.00
8	-3.0	0.0	0.00	0.00
5.6	-2.5	0.0	0.00	0.00
4	-2.0	0.0	0.00	0.00
2.8	-1.5	0.26	0.19	0.19
2	-1.0	0.66	0.48	0.67
1.5	-0.5	0.81	0.59	1.26
1	0.0	0.79	0.58	1.84
0.710	0.5	1.12	0.82	2.65
0.500	1.0	3.57	2.60	5.26
0.355	1.5	12.39	9.03	14.29
0.250	2.0	28.18	20.54	34.83
0.180	2.5	34.72	25.31	60.14
0.125	3.0	26.25	19.14	79.28
0.090	3.5	12.21	8.90	88.18
0.063	4.0	7.33	5.34	93.52
0.044	4.5	3.72	2.71	96.23
0.031	5.0	2.26	1.65	97.88
0.022	5.5	1.19	0.87	98.75
0.0156	6.0	0.64	0.47	99.22
0.0110	6.5	0.36	0.26	99.48
0.0078	7.0	0.22	0.16	99.64
0.0055	7.5	0.11	0.08	99.72
0.0039	8.0	0.13	0.09	99.82
0.0028	8.5	0.03	0.02	99.84
0.0020	9.0	0.07	0.05	99.89
0.0014	9.5	0.10	0.07	99.96
0.0010	10.0	0.06	0.04	100.00

BL-47.6 km. from the source

GPS: 63°59'28,525"N
21°53'33,304"W

Size (mm)	Size (phi)	Weight (g)	Weight (%)	Cumulative (%)
16	-4.0	0.0	0.00	0.00
11.2	-3.5	0.0	0.00	0.00
8	-3.0	0.0	0.00	0.00
5.6	-2.5	0.0	0.00	0.00
4	-2.0	0.0	0.00	0.00
2.8	-1.5	0.0	0.00	0.00
2	-1.0	0.0	0.00	0.00
1.5	-0.5	0.0	0.00	0.00
1	0.0	0.01	0.01	0.01
0.710	0.5	0.04	0.03	0.04
0.500	1.0	1.42	1.08	1.12
0.355	1.5	14.08	10.75	11.87
0.250	2.0	36.01	27.50	39.37
0.180	2.5	33.44	25.54	64.91
0.125	3.0	21.55	16.46	81.37
0.090	3.5	10.63	8.12	89.48
0.063	4.0	6.61	5.05	94.53
0.044	4.5	3.59	2.74	97.27
0.031	5.0	1.93	1.47	98.74
0.022	5.5	0.83	0.64	99.38
0.0156	6.0	0.35	0.26	99.65
0.0110	6.5	0.14	0.11	99.75
0.0078	7.0	0.08	0.06	99.82
0.0055	7.5	0.00	0.00	99.82
0.0039	8.0	0.11	0.08	99.90
0.0028	8.5	0.00	0.00	99.90
0.0020	9.0	0.04	0.03	99.93
0.0014	9.5	0.02	0.02	99.95
0.0010	10.0	0.07	0.05	100.00

VI-64.0 km. from the source

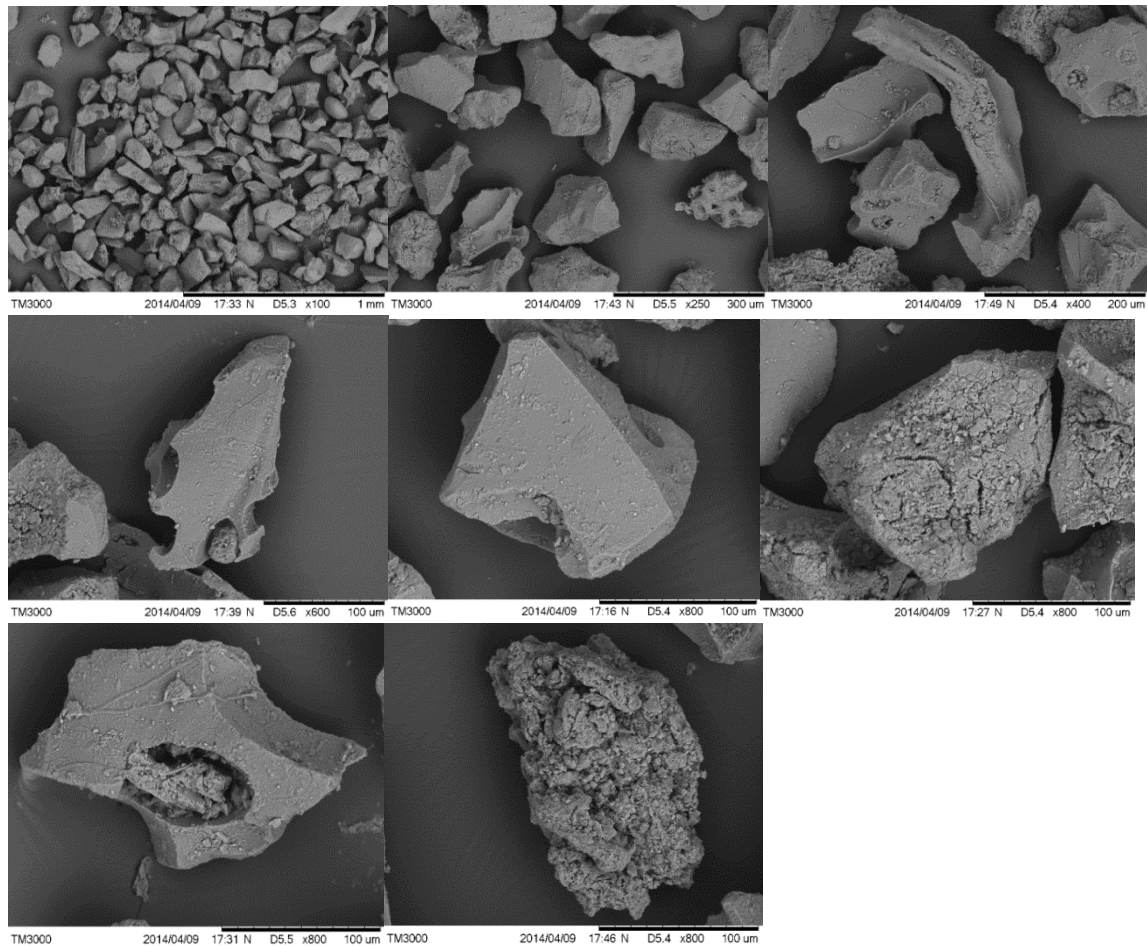
GPS: 64°2'22,076"N
21°34'24,817"W

Size (mm)	Size (phi)	Weight (g)	Weight (%)	Cumulative (%)
16	-4.0	0.0	0.00	0.00
11.2	-3.5	0.0	0.00	0.00
8	-3.0	0.0	0.00	0.00
5.6	-2.5	0.0	0.00	0.00
4	-2.0	0.0	0.00	0.00
2.8	-1.5	0.0	0.00	0.00
2	-1.0	0.0	0.00	0.00
1.5	-0.5	0.0	0.00	0.00
1	0.0	0.04	0.17	0.17
0.710	0.5	0.14	0.60	0.77
0.500	1.0	0.35	1.50	2.28
0.355	1.5	1.02	4.38	6.66
0.250	2.0	3.27	14.05	20.70
0.180	2.5	5.65	24.27	44.97
0.125	3.0	5.25	22.55	67.53
0.090	3.5	3.1	13.32	80.84
0.063	4.0	2.11	9.06	89.91
0.044	4.5	1.14	4.91	94.82
0.031	5.0	0.64	2.77	97.59
0.022	5.5	0.30	1.30	98.89
0.0156	6.0	0.11	0.46	99.34
0.0110	6.5	0.05	0.20	99.54
0.0078	7.0	0.01	0.05	99.59
0.0055	7.5	0.01	0.03	99.63
0.0039	8.0	0.03	0.12	99.75
0.0028	8.5	0.02	0.08	99.83
0.0020	9.0	0.02	0.08	99.92
0.0014	9.5	0.00	0.00	99.92
0.0010	10.0	0.02	0.08	100.00

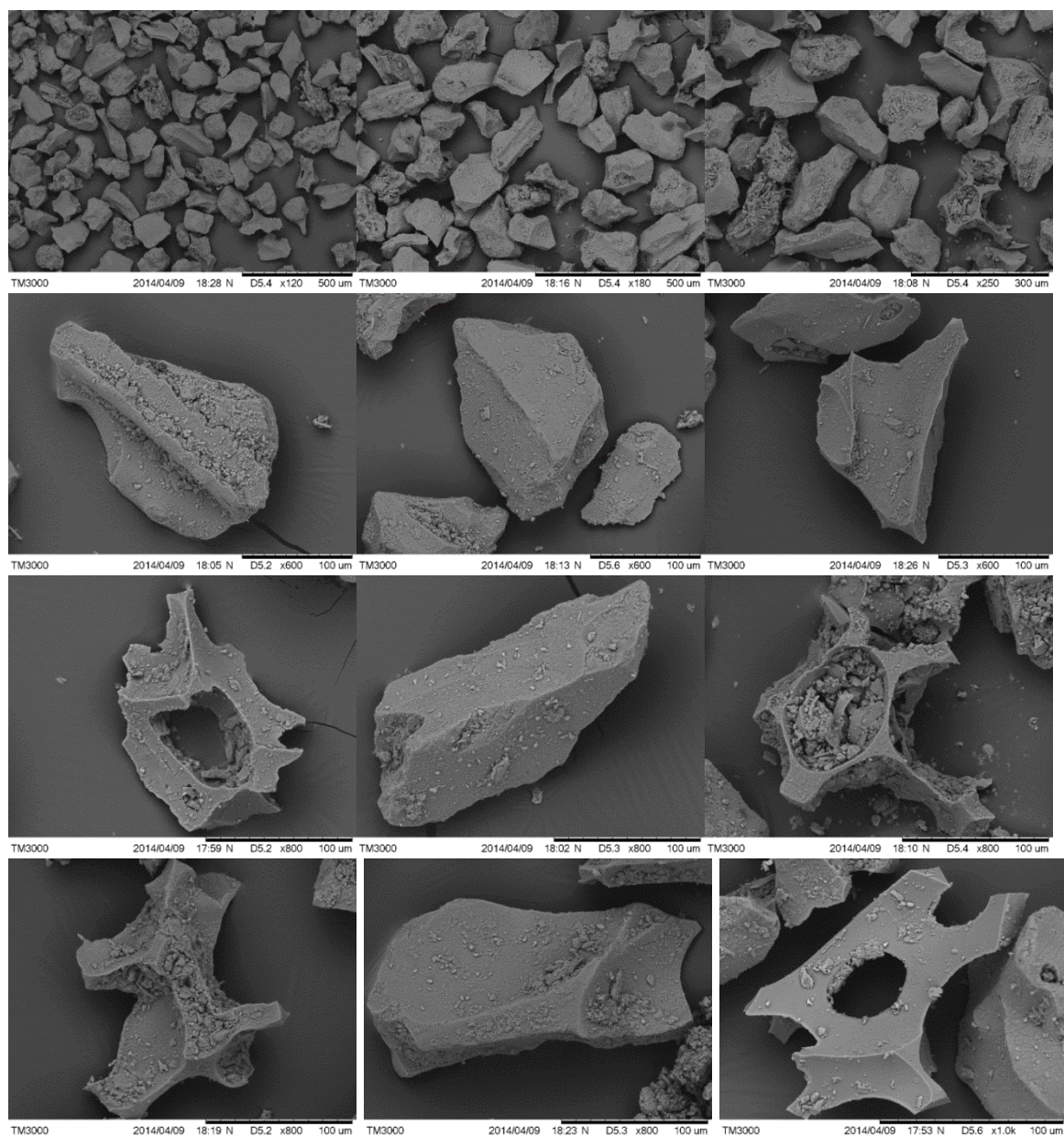
Appendix III

SEM-Images

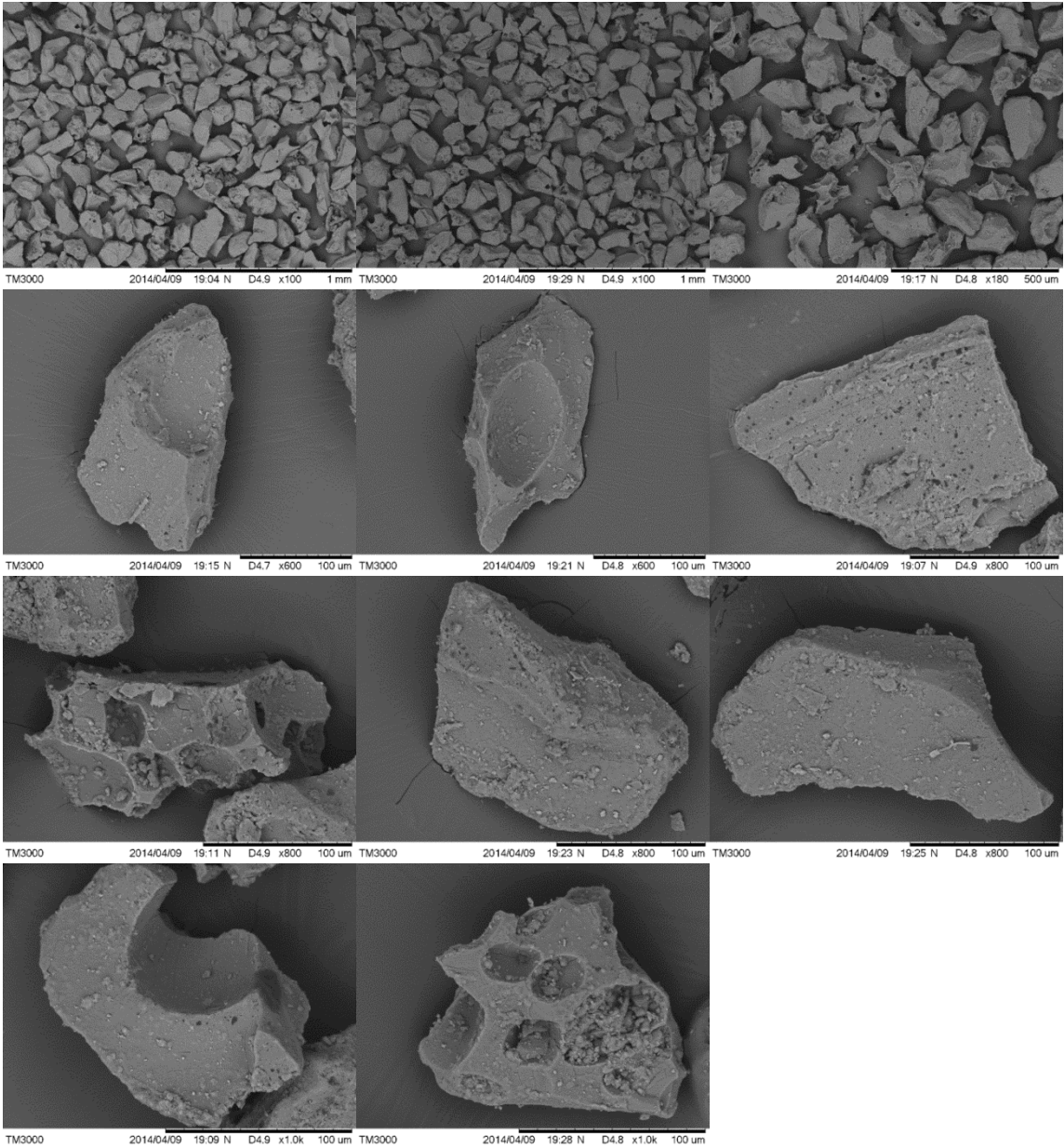
ST- ca. 11 km from source, 3.5 phi



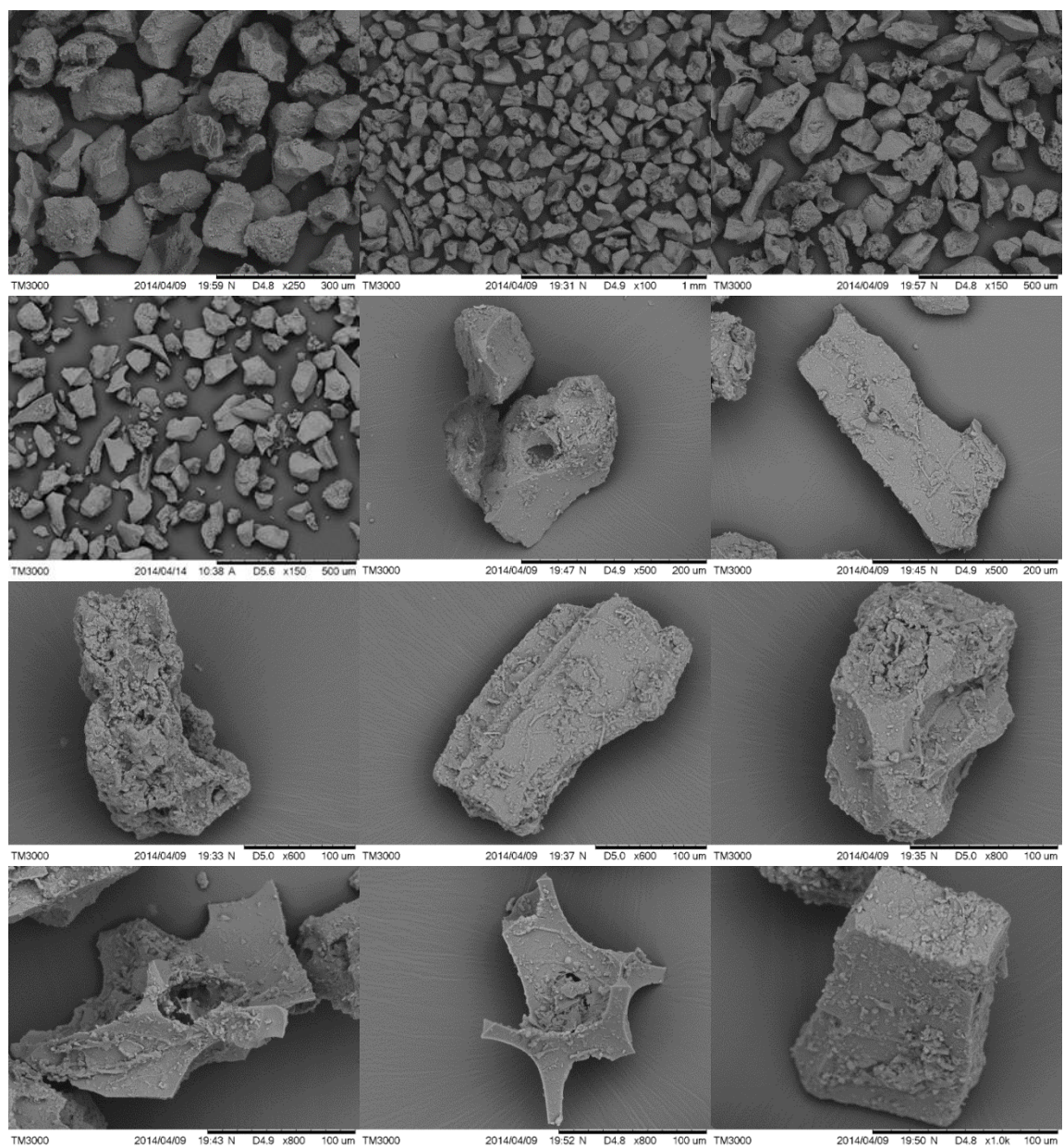
VL- ca. 35 km from source, 3.5 phi



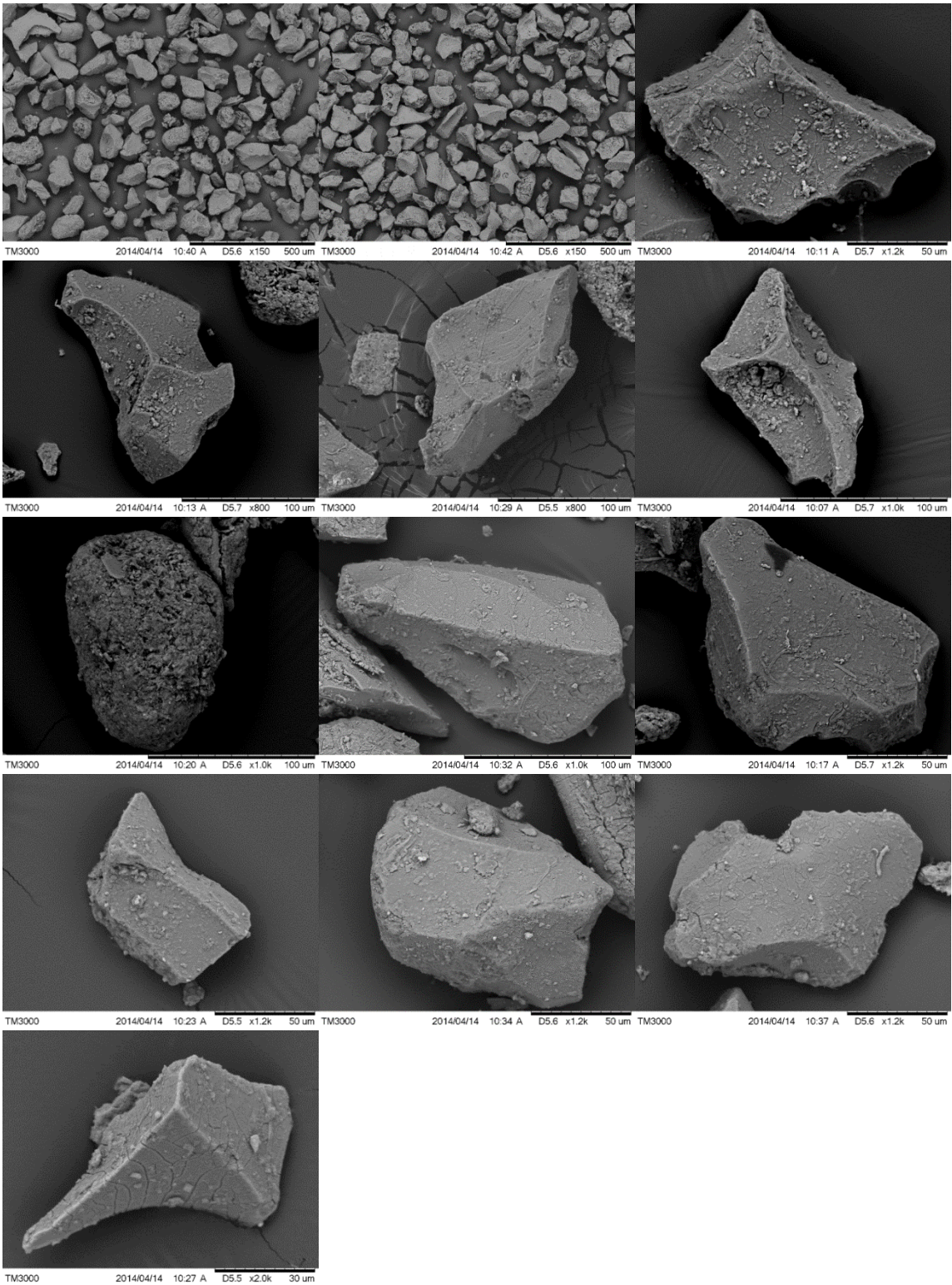
BL- ca. 48 km from the source, 3.5 phi



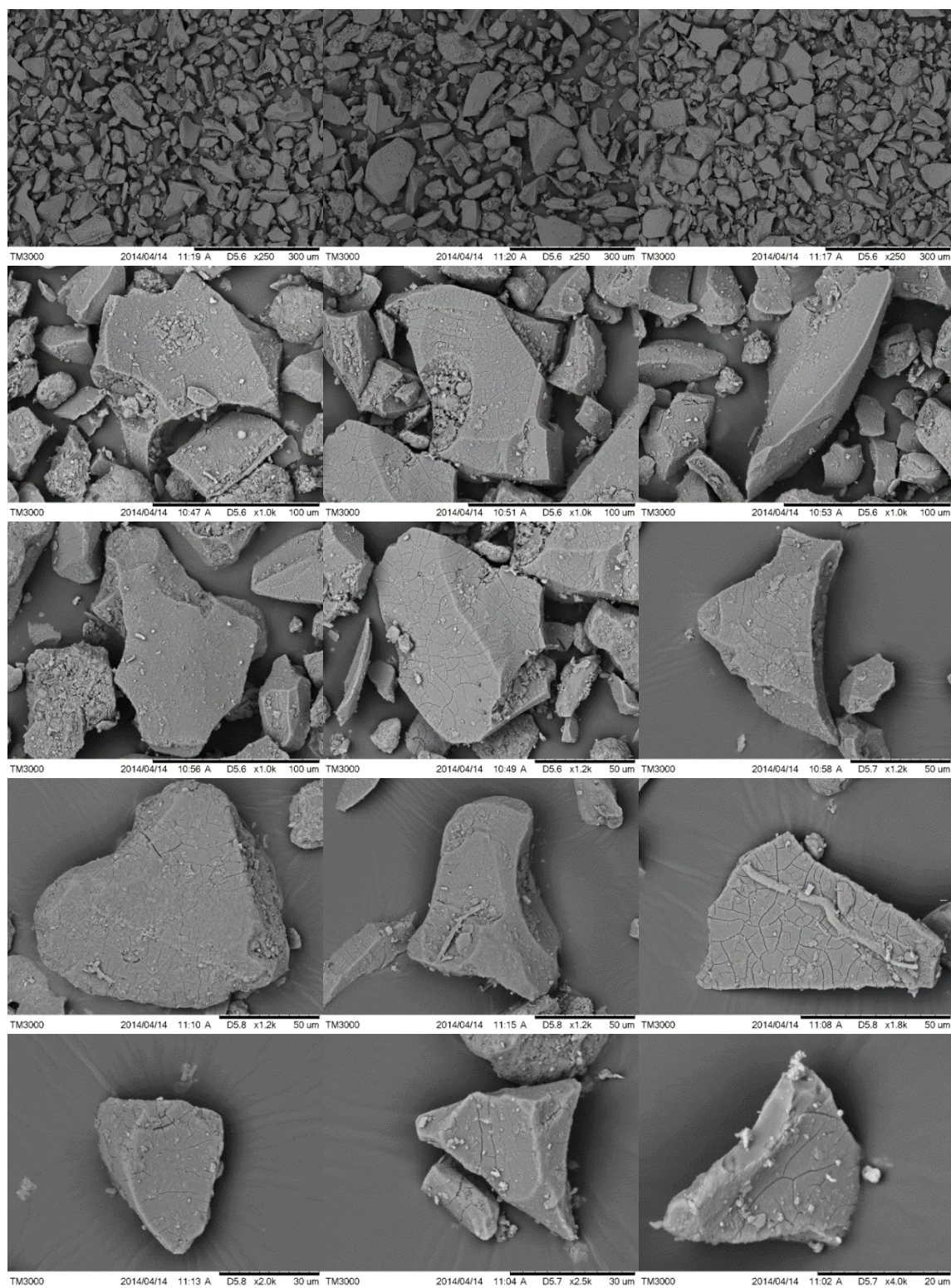
VI- ca. 64 km from source, 3.5 phi



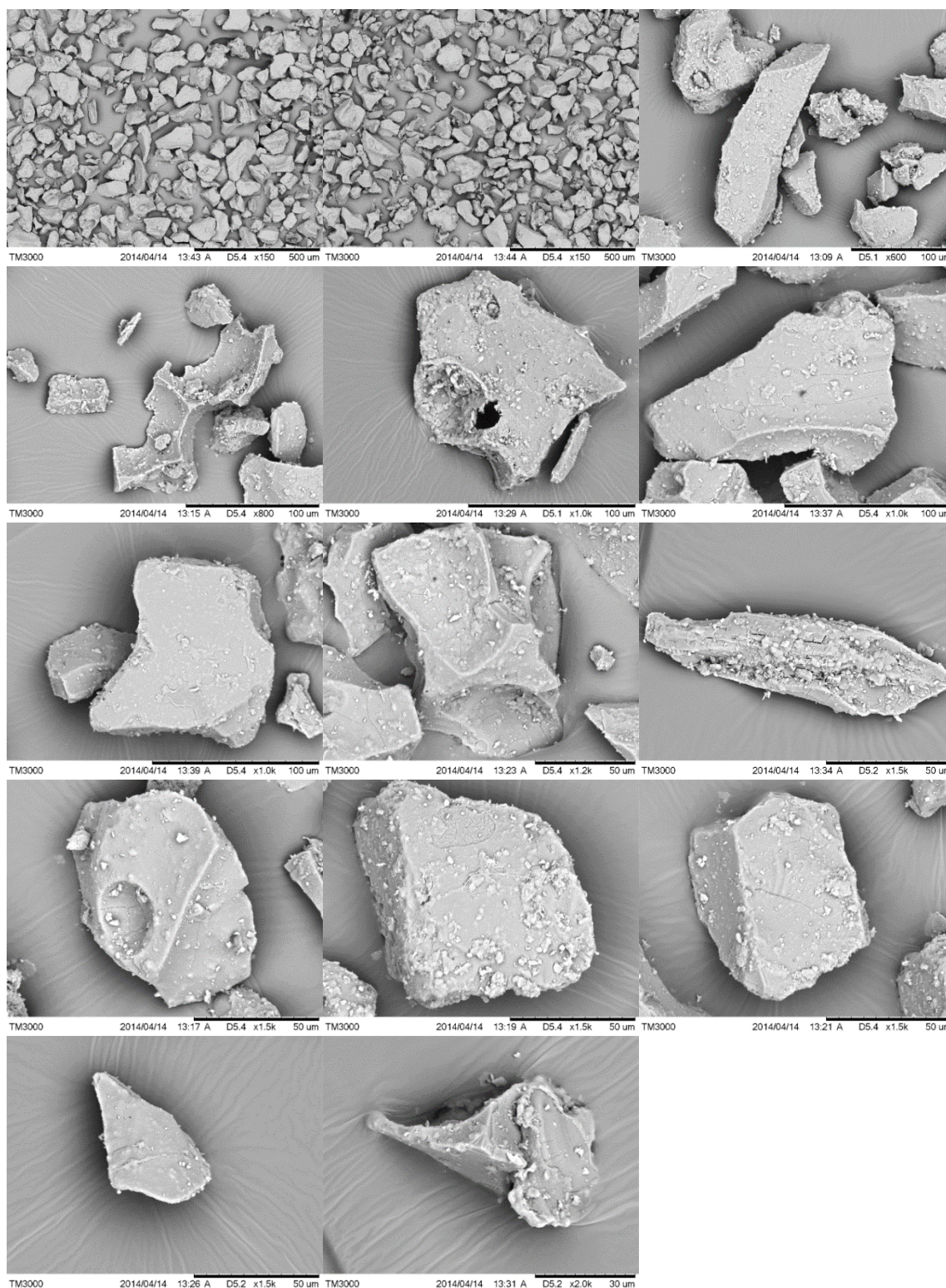
ST- ca. 11 km from source, 4 phis and below



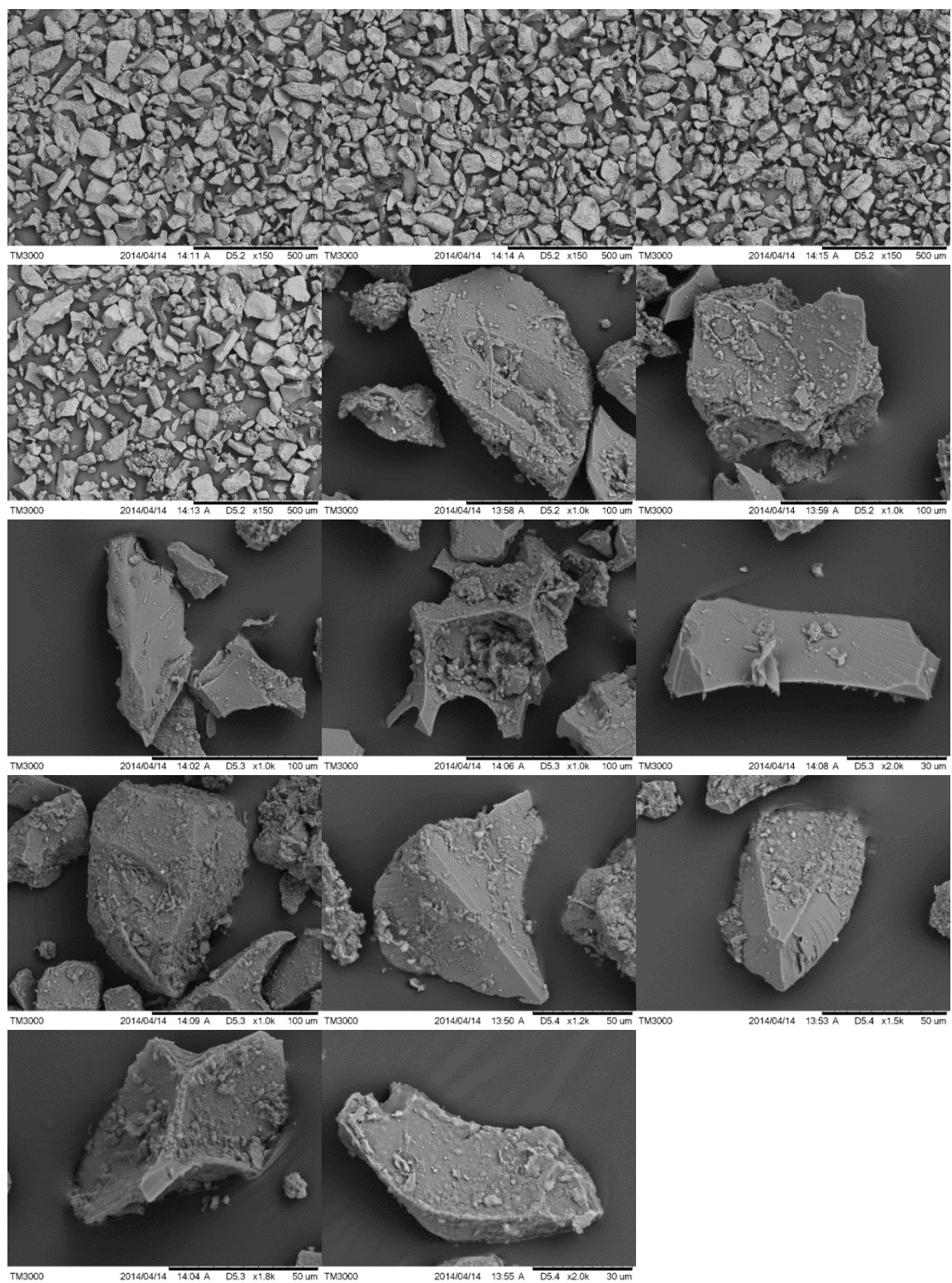
VL-ca. 34 km from source, 4 phis and below



BL- ca. 48 km from source, 4 phis and below



VI- ca. 64 km from source, 4 phis and below



Appendix IV

Density measurements

		Experiment 1	Experiment 2	Experiment 3
Weight of water in pyknometer	m_{1fl}	99.6909 g	99.7016 g	99.617 g
Weight of sample in pyknometer	m_s	0.7042 g	0.8597 g	0.9533 g
Weight of sample and water in pyknometer	m_{fl+s}	100.1305 g	100.2464 g	100.2209 g
Weigth of water in pyknometer	m_{2fl}	99.4263 g	99.3867 g	99.2676 g
Volume of pyknomter	V_{ges}	99.9137 ml	99.9244 ml	99.8396 ml
Volume of water	V_{fl}	99.6485 ml	99.6088 ml	99.4895 ml
Volume of sample	V_s	0.2652 ml	0.3156 ml	0.3502 ml
Density of sample	ρ_s	2.6554 g/ml	2.7240 g/ml	2.7223 g/ml
Mean, density of sample	ρ_s	2.7006 g/ml		

Appendix V

Statistical analysis

* represents that equal variances are assumed

<i>3.0 phi</i>	<i>VL-35 km.</i>		<i>VI-64 km.</i>	
	Mean	St.dv.	Mean	St.dv
<i>Circularity</i>	0.6461	0.1237	0.6279	0.1397
<i>Form factor</i>	0.6363	0.1279	0.6049	0.1354
<i>Compactness</i>	0.7999	0.0791	0.7871	0.0914
<i>Fiber aspect ratio</i>	2.7867	1.2653	3.0891	1.5460
<i>Feret aspect ratio</i>	1.4889	0.3666	1.5400	0.4559
<i>Ellipse aspect ratio</i>	1.4480	0.3631	1.4996	0.4509

<i>3.0 phi</i>	<i>VL-35 km. vs. VI-64 km.</i>		
	t	p-value	Std. error
<i>Circularity</i>	10.674	0.000	0.00170
<i>Form factor</i>	18.473	0.000	0.00170
<i>Compactness</i>	11.570	0.000	0.00110
<i>Fiber aspect ratio</i>	-16.581	0.000	0.1824
<i>Feret aspect ratio</i>	-9.563	0.000	0.00534
<i>Ellipse aspect ratio</i>	-9.760	0.000	0.00529

<i>3.5 phi</i>	<i>ST-11 km</i>		<i>VL-35 km.</i>		<i>VI-64 km.</i>	
	Mean	St.dv	Mean	St.dv.	Mean	St.dv
<i>Circularity</i>	0.6157	0.1345	0.6263	0.1240	0.6306	0.1274
<i>Form factor</i>	0.6454	0.1263	0.6459	0.1211	0.6351	0.1218
<i>Compactness</i>	0.7989	0.0843	0.7873	0.0803	0.7898	0.0861
<i>Fiber aspect ratio</i>	2.7672	1.2762	2.7153	1.2013	2.8029	1.2573
<i>Feret aspect ratio</i>	1.5431	0.4107	1.5198	0.3853	1.5280	0.3938
<i>Ellipse aspect ratio</i>	1.5059	0.4143	1.4796	0.3805	1.4899	0.3911

<i>3.5 phi</i>	ST-11 km. vs. VL-35km			ST-11 km. vs. VI-64 km.			VL-35 km. vs. VI-64 km.		
	t	p-value	Std. error	t	p-value	Std. error	t	p-value	Std. error
<i>Circularity</i>	-6.391	0.000	0.00167	-8.822	0.000	0.00169	-2.617	0.009	0.00162
<i>Form factor</i>	-0.314	0.753	0.00160	6.438	0.000	0.00160	6.898*	0.000	0.01081
<i>Compactness</i>	10.897	0.492	0.00107	8.456	0.000	0.00108	-2.372	0.018	0.00105
<i>Fiber aspect ratio</i>	3.244	0.001	0.01600	-2.184	0.029	0.01635	-5.520*	0.000	0.01587
<i>Feret aspect ratio</i>	4.528	0.000	0.00514	2.900	0.004	0.00519	-1.632	0.103	0.00503
<i>Ellipse aspect ratio</i>	5.130	0.000	0.02634	3.077	0.002	0.01600	0.006	0.038	0.00498

<i>4 phi and below</i>	ST-11 km		VL-35 km.		VI-64 km.	
	Mean	St.dv	Mean	St.dv.	Mean	St.dv
<i>Circularity</i>	0.5819	0.1383	0.5819	0.1348	0.5685	0.1331
<i>Form factor</i>	0.7244	0.1090	0.7124	0.1163	0.7623	0.1028
<i>Compactness</i>	0.7572	0.0972	0.7574	0.0908	0.7485	0.0906
<i>Fiber aspect ratio</i>	2.2655	0.9530	2.3494	1.0424	2.1309	0.9074
<i>Feret aspect ratio</i>	1.6081	0.4381	1.5864	0.4197	1.7039	0.4566
<i>Ellipse aspect ratio</i>	1.5753	0.4596	1.5529	0.4428	1.6653	0.4635

<i>4 phi and below</i>	ST-11 km. vs. VL-35km			ST-11 km. vs. VI-64 km.			VL-35 km. vs. VI-64 km.		
	t	p-value	Std. error	t	p-value	Std. error	t	p-value	Std. error
<i>Circularity</i>	0.009	0.993	0.00176	7.686	0.000	0.00175	7.776	0.000	0.00173
<i>Form factor</i>	-8.243	0.000	0.00145	-27.675	0.000	0.00137	-35.183	0.000	0.00142
<i>Compactness</i>	-0.189	0.850	0.00118	7.335	0.000	0.00118	7.605	0.000	0.00117
<i>Fiber aspect ratio</i>	-6.503	0.000	0.01289	11.207	0.000	0.01201	17.316	0.000	0.01262
<i>Feret aspect ratio</i>	3.919	0.000	0.00554	-16.597	0.000	0.00578	-20.768	0.000	0.00566
<i>Ellipse aspect ratio</i>	3.836	0.000	0.00583	-15.115	0.000	0.00596	-19.211	0.000	0.00585

